FAR INFRARED REFLECTION SPECTROSCOPY OF SOLIDS

by

Keith Alan Maslin

A Thesis submitted for the internal Degree of
Doctor of Philosophy in the Faculty
of Science, Royal Holloway
and Bedford New College
University of London

March 1986

ABSTRACT

The optical properties of a selection of crystalline solids have been studied in the far infrared by dispersive Fourier transform spectroscopy. This technique allows both the amplitude and phase to be determined without any approximation.

The measurements were performed on a modified Michelson interferometer, in which one of the mirrors is replaced with the sample to obtain the dispersive interferogram. The instrument was improved by replacing the stepper motor drive with a hydraulic piston and a high precision linear bearing. Sampling control was obtained by monitoring the cosine fringes from a secondary laser beam passed down the optic axis.

The far infrared amplitude and phase reflection spectra of eight zincblende structure binary semiconductors and two alkaline earth flourides have been measured, in most cases for the first time. Then, by using the equations of Maxwell and Fresnel, the refractive index, absorption index, and the real and imaginary parts of the dielectric response were obtained. From these functions the frequency dependence of the anharmonic self-energy function of the transverse optic mode at the centre of the Brillouin zone was calculated. Features observed in the self-energy functions of the zincblende crystals are attributed to phonon combination bands due to the decay of the lattice resonant mode. These are assigned by critical point analysis with the aid of lattice dynamical models to provide an experimental test of the phonon frequencies.

Finally, the amplitude and phase reflectivity of a GaAs-AlGaAs multiple quantum well structure and a GaAs-AlAs superlattice are presented for the first time. In the case of the multiple quantum well structure the results are shown to be in good agreement with calculations based on macroscopic dielectric theory.

ACKNOWLEDGEMENTS

I would like to express my sincerest thanks to Dr T.J Parker, who has helped in all aspects and without whom this work could not have been performed. Cheers Terry.

I would also like to thank my fellow co-workers in the Solid State laboratory, namely Dr G.A Gledhill, John Collins and Wan Abdullah.

I am very grateful for the technical help I have received during my time at Westfield and Royal Holloway colleges, especially Mr M.E. Thyer for the vacuum system, Mr E. Herrmann and Mr B. Porter for the construction of components of the interferometer, Mr T. Brooks for help with the electronics and Mr C. Winterton for help with the technical drawings and lunchtime consultations.

I would also like to thank Dr E.A.M Baker for the time spent at NPL, as well as some useful discussions.

Thanks must be given to Dr P.J Dobson at Philips Research laboratories, Redhill, for the loan of the superlattice crystals.

I would also like to thank Mr B Hawker for the time spent on my C.A.S.E award at Specac Ltd.

I would like to acknowledge the financial support of the Science and Engineering Research Council.

Finally, I would like to thank my parents for the support they have given. Thank you.

March 1986 K.A.Maslin

CONTENTS

LIST OF FIGURES

Page

CHAPTER 6

CHAPTER 1

Introduction

It is well known that information about lattice vibrations of crystalline solids can be obtained by studying the interaction of electromagnetic radiation with suitable samples. The variation of the wavevector K of lattice waves (phonons) with energy is represented in the dispersion curves, which comprise two distinct branches. One is termed the acoustic branch because in the limit of the wavevector $K \rightarrow 0$, the slope of the dispersion curve approaches the speed of sound in the material, while the other is termed the optic branch because it is responsible for infrared absorption, as described below. Both these branches can have transverse and longitudinal modes. Semiconductors with zinc blende lattice structures have two interpenetrating sub-lattices, one for the positive ions and the other for the negative ions. In the limit that the wavevector $K \rightarrow 0$, the transverse optic (TO) branch occurs when the two differently charged sub-lattices vibrate in opposite phase, inducing an electric dipole moment. This dipole moment can interact with the electric vector of electromagnetic radiation. The effect of this coupling, known as a polariton, is to generate a spectral region of high reflectivity known as the Reststrahlen region.

By using Maxwell's equations for the propagation of light in a medium and a suitable lattice model, either the

optical constants (n,k), or the dielectric functions (ϵ',ϵ'') can be related to the lattice properties. These functions completely describe the frequency dependent optical properties of the material. Apart from the main resonance peak, smaller features are present which are due to phonon decay modes. To study these small features in greater detail, the idea of an anharmonic self energy function Γ (Cowley 1963) is used. By knowing the values for the static (ϵ_0) and high frequency (ϵ_∞) real part of the dielectric response, as well as the frequency of the TO mode, the harmonic resonance can be eliminated from the dielectric functions. This then gives only the anharmonic components of the response function. Features arising in the function Γ are attributed to two and three phonon combination processes, such as overtones, summations and differences. Knowing the lattice structure, i.e zincblende, group theory can determine the selection rules, and which modes are infrared active. By the use of inelastic neutron scattering experiments and lattice dynamical models such as the Rigid Ion Model (RIM), values are obtained for phonon frequencies at the critical points. These can then be used to calculate the frequencies of phonon combination bands, which are compared to the experimental values for the peaks in Γ.

Early work on the optical properties of materials in the infrared was carried out using either grating or prism instruments, with the main limiting factor being the detector used. As these techniques were extended to the far infrared, problems were encounted due to the very low

intensities of the radiation. Two factors in Fourier transform spectroscopy which can improve the response are the Fellgett or multiplex advantage and the Jacquinot or throughput advantage, which are discussed in Appendix A.

With the advent of microcomputers to perform cost effective Fourier transformations, the technique of Fourier transform spectroscopy (FTS) has superceded conventional spectroscopy. To obtain the optical constants, both the amplitude and the phase response are required. In FTS, the phase is not determined directly because the sample is placed in the output optics of the instrument, so both partial beams undergo the same phase change. The phase can be calculated from this data by the use of Kramers-Kronig analysis. However, this has the disadvantage that the phase uncertainty is dependent on the spectral limits of the power spectrum, which in practice is a severe limitation. By placing the sample in one arm of the interferometer, the phase response is determined implicitly. This is the technique of dispersive Fourier transform spectroscopy (DFTS) as explained by Birch and Parker (1979). In the work described in this thesis, the sample is highly polished and is mounted in place of one of the mirrors in the fixed arm, producing reflection DFTS results.

The theoretical basis for all the instrumentation is contained in the two Fourier integrals given in chapter 2. When the instrument is used in the dispersive mode, the concept of the complex insertion loss developed by Chamberlain (1972) can be used to relate the complex Fourier transforms to the amplitude and phase. Then by the

use of Fresnel's equations for reflection at normal incidence, the refractive index n and the absorption index k, as well as the dielectric functions ϵ' and ϵ'' can be determined.

The instrument used for this work, as described in chapter 3, was based on the cube interferometer by Grubb Parsons Ltd, which divides the radiation into two partial arms at 90° to each other. The moving mirror was originally driven by a stepper motor, which could move in steps of 2.5μm. The infrared beam was phase modulated to obtain a satisfactory signal to noise ratio, and the interferogram was recorded via a Phase Sensitive Detector. This system had a number of serious limitations due to the slow scan speeds, inaccurate stepping and phase modulation.

The major improvement carried out on the instrument was replacing the stepper assembly by a high precision linear bearing, driven by a hydraulic piston and controlled by laser fringe counting. This improved the sampling accuracy by a factor of over 50, as well as removing the need to externally modulate the infrared beam. Because of the accuracy of the laser sampling technique, automation of the data collection is possible, allowing co-averaging of separate scans.

Chapter 4 describes the interaction of radiation with zinc blende structure crystals, and the effect this has on the reflectivity in the region around the transverse optic (TO) energy. By using a simple rigid ion model, the interaction can be described by a resonance model centered on the TO frequency. This model can be elaborated by

replacing the frequency independent damping function by a frequency dependent function Γ as shown by Cowley (1963). This function calculates the degree of anharmonicity as the TO mode decays into various phonon combinations. Also given is the plasma response due to free carriers which appears in some of the materials studied.

The amplitude r and phase ϕ of the reflection spectra of 8 zincblende semiconductors and 2 alkaline Earth flourides have been measured using the improved interferometer, and are shown in chapter 5. From this data have been calculated, using equations in chapter 2, the refractive index n and absorption index k, as well as the dielectric functions ϵ' and ϵ''. Also from the dielectric functions, the values for ω(TO) and ω(LO) at the zone centre have been experimentally determined. Using these results with the equation for Γ given in chapter 4, along with values for ϵ_0, ϵ_∞ and ω(TO), the anharmonic self energy function has been determined. Features observed in Γ were compared with the frequencies of phonon combination bands from neutron scattering, Raman scattering and previous infrared work, as well as results from an 11 parameter RIM by Patel (1982). These are the first reported measurements by DFTS for most of these materials, and in many cases these are also the first determinations of the optical and dielectric parameters in the region of the lattice resonance. In each case new structure associated with lattice combination bands has been revealed in the Reststrahl region, and the agreement with expected features is generally good.

Recently, multiple layered semiconductor crystals grown by molecular beam epitaxy (MBE) have been obtained. Both superlattice (SL) and multiple quantum well (MQW) structures grown from layers of GaAs and $Al_{1-x}Ga_xAs$ have been studied by reflection DFTS for the first time, with some of the results shown in chapter 6. These results are compared to model calculations performed by Raj and Tilley (1985), and are in good agreement.

1.1 References

Birch J.R and Parker T.J; Infrared and Millimetre waves, Vol. 2, 137, Edited by K.J Button, Academic Press

Chamberlain J.E; Infrared phys. 11, 145-164 (1972)

Cowley R.A; Adv Phys, 12, 421 (1963)

Patel C; Ph.D Thesis of (1982), University of London

Raj N and Tilley D.R; Sol.State.Comm, 55, 373 (1985)

CHAPTER 2

The general theory of Fourier transform spectroscopy

2.1 Fourier Transform Spectrocopy

One of the main differences between Fourier Transform Spectroscopy (FTS) and grating or prism spectrocopy is that the data obtained after scanning is not the spectrum, but a Fourier transform of all the spectral components known as the interferogram. Generally the shape of the interferogram conveys very little as to the true spectral output because of the number of individual components. To sort them out requires the Fourier integral pair as shown below

$$A(x) = \int_{-\infty}^{+\infty} B(\nu)\, e^{i2\pi\nu x}\, d\nu \qquad (2.1)$$

$$B(\nu) = \int_{-\infty}^{+\infty} A(x)\, e^{-i2\pi\nu x}\, dx \qquad (2.2)$$

This relates the two functions A(x) and B(ν) so that if one is known, the other can be determined. In the case of Fourier transform infrared spectroscopy the function A(x) is the interferogram, with the variable x as the optical path difference in centimetres. The function B(ν) is the spectrum, with the variable ν given in wavenumbers (cm^{-1}). One major difference between the properties of the above

equations and the behaviour of a real instrument is that equation (2.2) integrates from $-\infty$ to $+\infty$, and infinite limits of optical path difference cannot be achieved experimentally. Because the actual scan is limited, this introduces an experimental line width, and so limits the resolution. Other effects like sidelobes are associated with a limited scan length, but these can be reduced by apodizing. Another difference is that because the interferogram is an experimentally sampled function, the integrals should be replaced with a discrete summation over the total scan. One effect of the sampling is aliasing, which limits the spectral range for a given step interval. These and other factors can be found in books by Chantry (1971) and Bell (1972).

The experimental configurations for Fourier transform spectroscopy are shown schematically in figure (2.1). This shows both reflection and transmission modes for a standard Michelson interferometer. These show that the sample is placed in the output beam, after the two beams from the arms have recombined. From these arrangements either the power reflectivity or power transmissivity can be obtained. To obtain the complex functions like the amplitude and phase, Kramers-Kronig analysis of the power throughput can be used. The main disadvantage in using this is that to obtain the true complex terms, an integration over infinite limits of frequency is required. However, it is experimentally difficult to find the power throughput from radio waves to X-rays, and so the determination of the phase contains approximations. To obtain the complex

functions directly, Dispersive Fourier Transform Spectroscopy (DFTS) is used, and is described in the next section.

2.2 DFTS and the complex insertion loss

The difference between DFTS and conventional FTS is that in DFTS the sample is placed in one of the arms of the instrument. The experimental arrangements for performing DFTS measurements are shown in figure (2.2). This shows schematically both single and double pass transmission as well as reflection. Because the sample is placed in one of the arms, the phase response will be present in the interferogram. To derive an expression relating the interferograms to the optical constants, it is useful to define the complex insertion loss as given by Chamberlain (1972), as

$$\tilde{L}(\nu) = L(\nu)\, e^{i\phi_L(\nu)} \qquad (2.1)$$

This is a complex factor by which the amplitude and phase is changed when a reference material such as a vacuum or perfect mirror is replaced by the specimen.

It can be shown that the electric field vector of a wave propagating in the fixed arm of the interferometer in free space can be written as a Fourier integral

$$\underline{\tilde{E}}_1 = \int_{-\infty}^{+\infty} \underline{\tilde{E}}_0(\nu)\, e^{i2\pi\nu(z-ct)}\, d\nu \qquad (2.2)$$

where $\underline{\tilde{E}}_0(\nu)$ is the amplitude, z is the coordinate in the

direction of propagation and t is time. There will also be an equation for the electric field propagating in the moving mirror arm, given by

$$\underline{\tilde{E}}_2 = \int_{-\infty}^{+\infty} \underline{\tilde{E}}_0(\nu)\, e^{i2\pi\nu(z+x-ct)}\, d\nu \qquad (2.3)$$

where $x/2$ is the displacement of the moving mirror from the position of zero path difference.

If we now consider placing a specimen in the fixed mirror arm, then the modified output beam will be given by

$$\underline{\tilde{E}}_1 = \int_{-\infty}^{+\infty} \underline{\tilde{E}}_0(\nu)\, L(\nu)\, e^{i[2\pi\nu(z-ct)+\phi_L(\nu)+\phi_0(\nu)]}\, d\nu \qquad (2.4)$$

where $\phi_0(\nu)$ is a small residual phase difference caused by a lack of perfect symmetry due to imperfect alignment, or some other asymmetry between the optical paths.

The electric field amplitude in the recombined beam propagating towards the output port is

$$\underline{\tilde{E}}_r = \underline{\tilde{E}}_1 + \underline{\tilde{E}}_2 = \int_{-\infty}^{+\infty} \underline{\tilde{g}}(\nu,x)\, e^{i2\pi\nu(z-ct)}\, d\nu \qquad (2.5)$$

$$\text{where} \quad \underline{\tilde{g}}(\nu,x) = \underline{\tilde{E}}_0(\nu) \left[\underline{L}(\nu)\, e^{i\phi(\nu)} + e^{i2\pi\nu x} \right] \qquad (2.6)$$

$$\text{and} \quad \phi(\nu) = \phi_L(\nu) + \phi_0(\nu) \qquad (2.7)$$

The output intensity, $\underline{\tilde{E}}_r\underline{\tilde{E}}_r^* = I_s(x)$ is proportional to $\underline{\tilde{g}}(\nu,x)\underline{\tilde{g}}^*(\nu,x)$, where * indicates the complex conjugate. Therefore, by using equations (2.2), (2.3) and (2.5), the output intensity $I_s(x)$ can be expressed as

$$I_s(x) = \int_{-\infty}^{+\infty} \underline{\tilde{g}}(\nu,x)\ \underline{\tilde{g}}^{*}(\nu,x)\ d\nu \tag{2.8}$$

$$\left.\begin{aligned} &= \int_{-\infty}^{+\infty} \underline{\tilde{E}}_0(\nu)\ \underline{\tilde{E}}_0^{*}(\nu)\ \left[\ 1 + L^2(\nu)\ \right]\ d\nu \\ &+ 2\int_{-\infty}^{+\infty} \underline{\tilde{E}}_0(\nu)\ \underline{\tilde{E}}_0^{*}(\nu)\ L(\nu)\cos\left[\ \phi(\nu) - 2\pi\nu x\ \right]\ d\nu \end{aligned}\right\} \tag{2.9}$$

The first term in equation (2.9) is independent of x and so plays no part in the interferogram. The second term is the interference function, i.e. the interferogram, which can be rewritten as a sum of even and odd components

$$\left.\begin{aligned} I_s(x) &= \int_{-\infty}^{+\infty} \rho(\nu)\ \cos\phi(\nu)\ \cos(2\pi\nu x)\ d\nu \\ &+ \int_{-\infty}^{+\infty} \rho(\nu)\ \sin\phi(\nu)\ \sin(2\pi\nu x)\ d\nu \end{aligned}\right\} \tag{2.10}$$

where $\rho(\nu) = 2\ \underline{\tilde{E}}_0(\nu)\ \underline{\tilde{E}}_0^{*}(\nu)\ L(\nu)$ (2.11)

The quantity $\rho(\nu)$ is the power spectrum, while $\phi(\nu)$ is the phase difference between the two partial waves. By taking the cosine and sine transforms of equation (2.10), the resulting functions are

$$p(\nu) = \int_{-\infty}^{+\infty} I_s(x)\ \cos(2\pi\nu x)\ dx = \rho(\nu)\ \cos\phi(\nu) \tag{2.12}$$

$$q(\nu) = \int_{-\infty}^{+\infty} I_s(x)\ \sin(2\pi\nu x)\ dx = \rho(\nu)\ \sin\phi(\nu) \tag{2.13}$$

The computed spectrum will be given by

$$\tilde{s}(\nu) = p(\nu) + iq(\nu) = \rho(\nu)\, e^{i\phi(\nu)} \qquad (2.14)$$

with a modulus of

$$\rho(\nu) = \left[p^2(\nu) + q^2(\nu) \right]^{\frac{1}{2}} \qquad (2.15)$$

and a phase

$$\phi(\nu) = \tan^{-1} \left[\frac{q(\nu)}{p(\nu)} \right] \qquad (2.16)$$

By comparing equations (2.1), (2.7) and (2.10 - 13) it follows that the complex insertion loss is related to the complex Fourier transform of the interferogram by

$$2\, \underline{\tilde{E}}_0(\nu)\, \underline{\tilde{E}}_0^*(\nu)\, L(\nu)\, e^{i\phi_0(\nu)} = \int_{-\infty}^{+\infty} I_S(x)\, e^{2\pi i \nu x}\, d\nu \qquad (2.17)$$

The specimen, which was in one of the arms, is now removed so as to return the interferometer to the symmetric mode. Now the background interferogram, $I_0(x)$, is recorded, and it can be shown that

$$I_0(x) = \int_{-\infty}^{+\infty} \rho_0(\nu) \cos\left[\phi_0(\nu) - 2\pi\nu x \right] d\nu \qquad (2.18)$$

which is similiar to the interference part of equation (2.9), with

$$\rho_0(\nu) = 2\, \underline{\tilde{E}}_0(\nu)\, \underline{\tilde{E}}_0^*(\nu) \qquad (2.19)$$

The cosine and sine transforms of equation (2.18) can be computed, to give

$$p_0(\nu) = \int_{-\infty}^{+\infty} I_0(x) \cos 2\pi\nu x \, dx = \rho_0(\nu) \cos\phi_0(\nu) \quad (2.20)$$

and

$$q_0(\nu) = \int_{-\infty}^{+\infty} I_0(x) \sin 2\pi\nu x \, dx = \rho_0(\nu) \sin\phi_0(\nu) \quad (2.21)$$

This gives a computed background spectrum of the interferometer of

$$s_0(\nu) = p_0(\nu) + iq_0(\nu) = \rho_0(\nu) \, e^{i\phi_0(\nu)} \quad (2.22)$$

This is a complex quantity, having a modulus of

$$\rho_0(\nu) = \left[p_0^2(\nu) + q_0^2(\nu) \right]^{\frac{1}{2}} \quad (2.23)$$

and a phase of

$$\phi_0(\nu) = \tan^{-1}\left[\frac{q_0(\nu)}{p_0(\nu)} \right] \quad (2.24)$$

Hence from equations (2.19 - 22) it follows that

$$2 \, \tilde{E}_0(\nu) \, \tilde{E}_0^*(\nu) \, e^{i\phi_0(\nu)} = \int_{-\infty}^{+\infty} I_0(x) \, e^{2\pi i\nu x} \, dx \quad (2.25)$$

so that the complex insertion loss can be obtained from equation (2.17) and (2.25), as the ratio of the two complex Fourier transforms as shown below

$$\tilde{L}(\nu) = \frac{\int_{-\infty}^{+\infty} I_S(x) \, e^{i2\pi\nu x} \, dx}{\int_{-\infty}^{+\infty} I_0(x) \, e^{i2\pi\nu x} \, dx} = \frac{FT\left[I_S(x) \right]}{FT\left[I_0(x) \right]} \quad (2.26)$$

where the function FT in the equation represents the

Fourier transform, as a mathematical operation performed in the computer. By using the above equation, the complex insertion loss can be calculated directly if complex numbers are used. Since the Fourier transform programs are written in Pascal, and standard Pascal does not support complex notation, the functions $L(\nu)$ and $\phi_L(\nu)$ are calculated using the cosine and sine Fourier transforms of $I_S(x)$ and $I_0(x)$ given by equations (2.12 - 13) and (2.20 - 21). This gives

$$L(\nu) = \frac{\left[p^2(\nu) + q^2(\nu) \right]^{\frac{1}{2}}}{\left[p_0^2(\nu) + q_0^2(\nu) \right]^{\frac{1}{2}}} \qquad (2.27)$$

and

$$\phi_L(\nu) = \tan^{-1}\left[\frac{q(\nu)}{p(\nu)} \right] - \tan^{-1}\left[\frac{q_0(\nu)}{p_0(\nu)} \right] \qquad (2.28)$$

2.3 Amplitude reflectivity for opaque solids

The method described below applies to all the data obtained in this thesis since it is the high reflectivity regions of the materials which are of interest. To obtain the complex insertion loss, firstly the background interferogram $I_0(x)$ is recorded, then the fixed mirror is replaced with the sample and accurately aligned with the use of the laser. Because this is also used to obtain the laser fringes while scanning, this gives a very precise alignment method as the size of the fringes is directly related to the degree of alignment. The sample interferogram $I_S(x)$ is then recorded. Since the materials

are highly absorbing, there are no higher terms due to transmission and subsequent reflections. This gives an amplitude reflectivity of the reference mirror of

$$\tilde{r}_0(\nu) = r_0(\nu)\, e^{i\phi_0(\nu)} \tag{2.30}$$

and for the sample

$$\tilde{r}_S(\nu) = r_S(\nu)\, e^{i\phi_S(\nu)} \tag{2.31}$$

This will give a complex insertion loss by using equation (2.26) of

$$\tilde{L}(\nu) = \frac{\tilde{r}_S(\nu)}{\tilde{r}_0(\nu)} = \frac{r_S(\nu)\, e^{i\phi_S(\nu)}}{r_0(\nu)\, e^{i\phi_0(\nu)}} \tag{2.32}$$

Since for a perfect mirror the amplitude would be 1.0 and the phase equal to π, this leads to

$$\tilde{L}(\nu) = r_S(\nu)\, e^{i(\phi_S(\nu) - \pi)} = \frac{FT\left\{ I_S(x) \right\}}{FT\left\{ I_0(x) \right\}} \tag{2.33}$$

So, from equations (2.27) and (2.28) the complex insertion loss can be calculated, and then by using equation (2.33), the amplitude $r_S(\nu)$ and the phase $\phi_S(\nu)$ can be found.

2.4 The response functions

Using the Fresnel equations at normal incidence, as given by Birch and Parker (1979), the amplitude reflectivity of the surface of a medium 1 immersed in a medium 2 is given as

$$\tilde{r}(\nu) = \frac{\tilde{N}_1(\nu) - \tilde{N}_2(\nu)}{\tilde{N}_1(\nu) + \tilde{N}_2(\nu)} \tag{2.34}$$

where $\tilde{N}_1(\nu)$ is the complex refractive index of medium 1 and $\tilde{N}_2(\nu)$ is the complex reflective index of medium 2.

The instrument is evacuated while scanning so that medium 1 is a vacuum, with a refractive index $\tilde{N}_1(\nu) = 1$, so the equation reduces to

$$\tilde{r}(\nu) = \frac{1 - \tilde{N}_2(\nu)}{1 + \tilde{N}_2(\nu)} \qquad (2.35)$$

This can be rearranged to give the complex refractive index of $\tilde{N}_2(\nu)$ as

$$\tilde{N}_2(\nu) = \frac{1 - \tilde{r}(\nu)}{1 + \tilde{r}(\nu)} \qquad (2.36)$$

From Maxwell's equations (Chantry 1984 or any other standard text on Electromagnetism) it can be shown that the complex refractive index is given by

$$\tilde{N}(\nu) = n(\nu) + ik(\nu) \qquad (2.37)$$

where Real $\tilde{N}(\nu) = n(\nu)$ Refractive index

Imag $\tilde{N}(\nu) = k(\nu)$ Absorption index

From equation (2.36) the refractive and absorption indices can now be calculated. Also the complex refractive index is related to the complex dielectric permittivity by

$$\tilde{\epsilon}(\nu) = \tilde{N}^2(\nu) = \left[n(\nu) + ik(\nu)\right]^2 \qquad (2.38)$$

and

$$\tilde{\epsilon}(\nu) = \epsilon'(\nu) + i\epsilon''(\nu) \qquad (2.39)$$

The real and imaginary components of the dielectric permittivity can be expressed in terms of the refractive and absorption indexes, as given below

$$\epsilon'(\nu) = n^2(\nu) - k^2(\nu) \tag{2.40}$$

$$\epsilon''(\nu) = 2\, n(\nu)\, k(\nu) \tag{2.41}$$

Also from these equations the electric susceptibility χ can be determined, which will be of use later on to determine the optical characteristics of solids.

$$\tilde{\epsilon}(\nu) = 1 + \tilde{\chi}(\nu) \tag{2.42}$$

$$\tilde{\chi}(\nu) = \chi'(\nu) + i\chi''(\nu) \tag{2.43}$$

From the above equations, the real and imaginary parts of the dielectric permittivity are given by

$$\text{Real}\quad \epsilon'(\nu) = 1 + \chi'(\nu) \tag{2.44}$$

$$\text{Imag}\quad \epsilon''(\nu) = \chi''(\nu) \tag{2.45}$$

Thus, by using the complex insertion loss, it can be seen that all of the response functions can be obtained from the Fourier transform pair.

2.5 References

Bell R.J; "Introductory Fourier transform spectroscopy" Academic Press, New York (1972).

Birch J.R and Parker T.J; Infrared and Millimetre waves, 2, 137, Edited by K.J.Button, Academic Press, New York (1979).

Chamberlain J.E; Infrared phys. 11, 145-164 (1972).

Chantry G.W; "Submillimetre spectroscopy" Academic Press, New York (1971).

Chantry G.W; "Long wave optics", Academic Press, New York (1984).

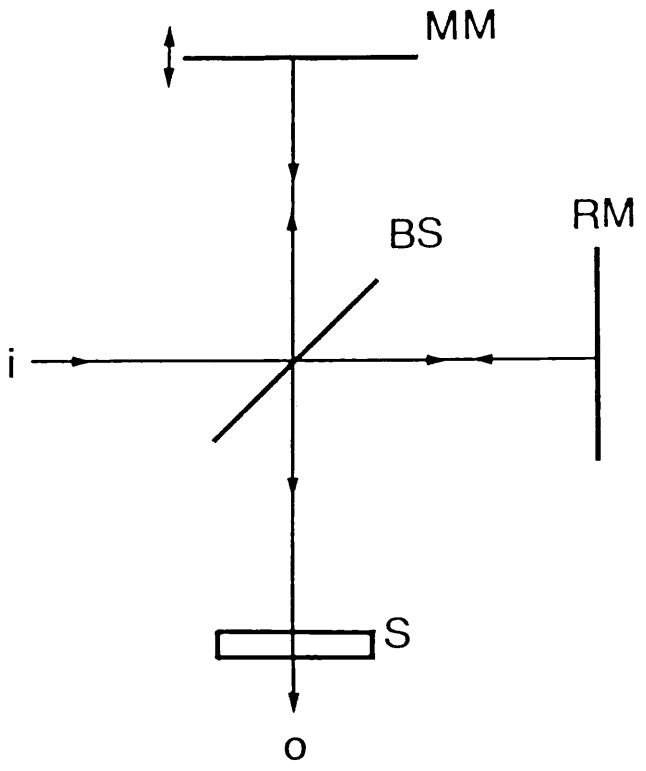

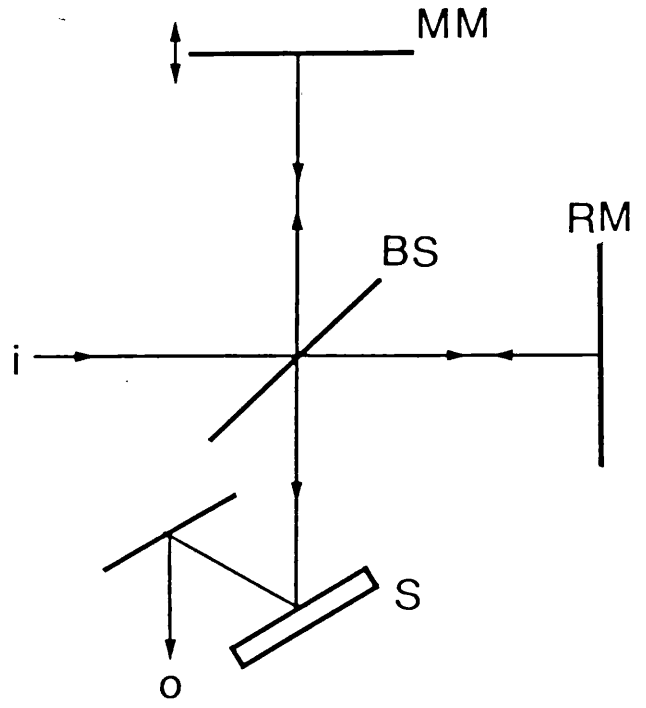

Figure 2.1 Schematic diagram of a Power Fourier transform spectrometer (a) Transmission (b) Reflection

Key : i input beam, O output beam, MM moving mirror RM reference mirror, BS beam splitter, S sample.

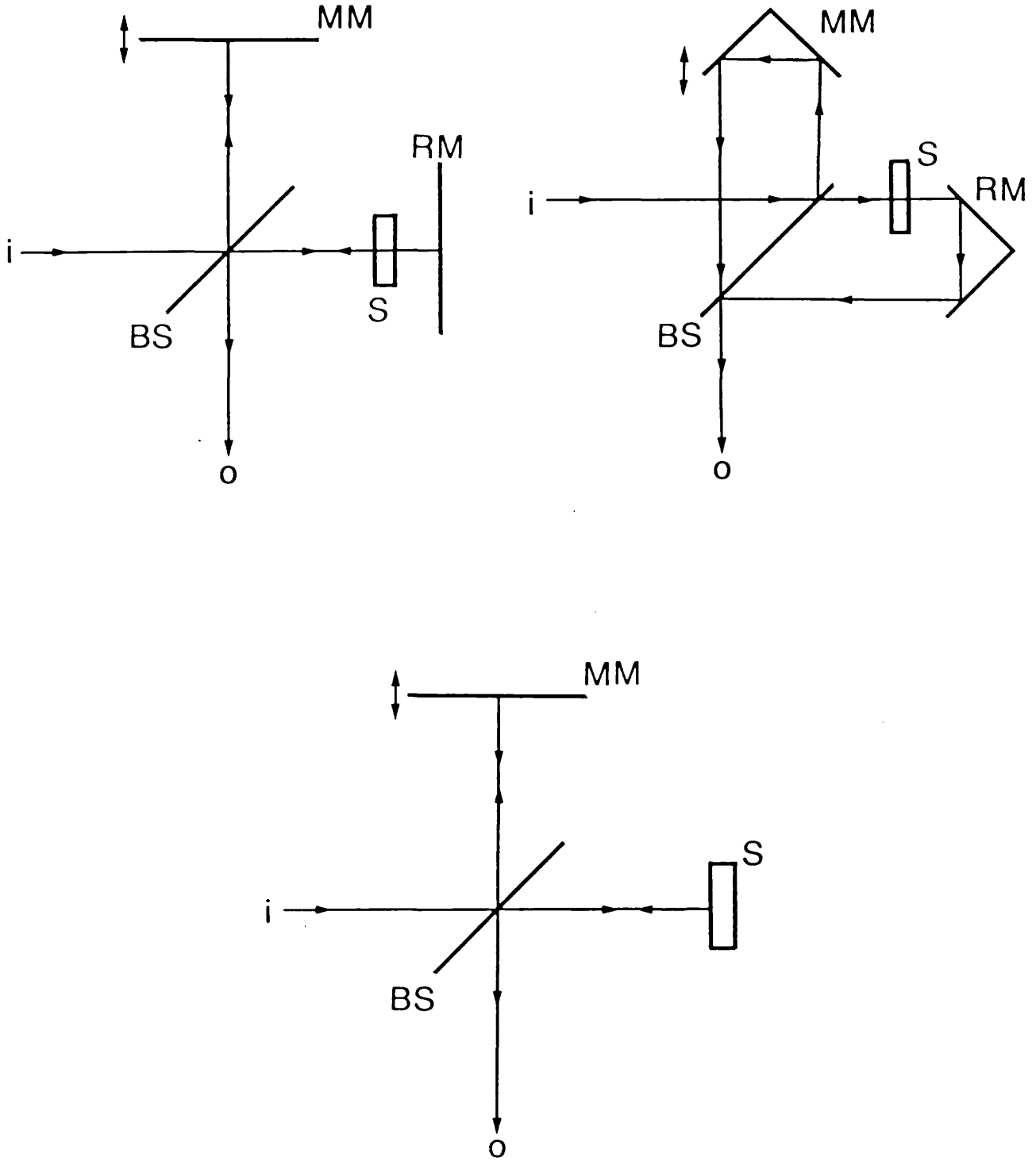

Figure 2.2 Schematic diagram of a dispersive Fourier transform spectrometer (a) Double pass transmission (b) Single pass transmission (c) Reflection.

Key : i input beam, O output beam, MM moving mirror RM reference mirror, BS beam splitter, S sample.

CHAPTER 3

Instrumentation

3.1 Introduction

The instrument under development is based on an NPL / Grubb Parsons cube interferometer. The basic design of the interferometer is shown in figure (3.1). This was first used with a stepper motor to control the moving mirror, but has now been developed using a hydraulic piston to improve the stepping accuracy. Firstly we will deal with the earlier method and show how problems arising from the stepper method can be eliminated by the use of a continuously scanned mirror.

3.2 Step driven interferometer

The basis of this system is the central cube. This holds the beam splitter at an angle of 45° to the incoming beam. The beam splitter is made of either Mylar (polyethylene terephthalate) or tungsten wires. Mylar does have certain advantages over wire grids, namely

(1) Cost.

Mylar can be supplied as large industrial rolls whereas thin tungsten wire (≈ 10μm in diameter) is very expensive due to the difficulties in manufacture.

(2) Ease of manufacture.

If the plastic is broken, a new piece can be stretched in place in a few minutes.

(3) Ease of alignment.

It allows the use of a laser beam which is coincident to the optical axis for alignment.

It does however have one major disadvantage because of the thickness, that of multiple interference. For a perfect Michelson interferometer the maximum efficiency of the beam splitter will be 50%. This is achieved only if the reflectivity R, and the transmittivity T are both 0.5. This is not the case for Mylar because only the primary transmitted and the primary and secondary reflected beams are of importance, as discussed in Bell (1972).

This gives rise to an equation relating the thickness of the beam splitter to the interference maxima and minima, given by

$$m\lambda = 2d \left[n^2 - \frac{1}{2} \right]^{\frac{1}{2}} \qquad (3.1)$$

where d is the thickness of the mylar and

n is the refractive index.

The condition for an interference maximum is when

$m = {}^1/_2, {}^3/_2, {}^5/_2, \ldots$

and for an interference minimum when

$m = 0, 1, 2, \ldots$

Experimentally, say for a 12.5μm beam splitter, the minima occur at 250cm^{-1}, 500cm^{-1}, 750cm^{-1},.. This is usually a large enough spectral range, but the low wave-number response is less than if wire grids are used, see Chantry (1984).

The method of using wire grids instead of Mylar was first put to good use in the Martin-Puplett interferometer, see Martin et al (1969).

Because all of the optical Reststrahlen responses of semiconductors are in the range 100cm^{-1} to 500cm^{-1}, Mylar was used in all this work. Thicknesses of between 12.5μm and 3μm were chosen for this work, depending on the spectral range required.

3.3 The collimator

The radiation source used is a fused quartz encapsulated Mercury lamp (Philips 125-HPK). Around the lamp is a copper heat shield, into which is drilled the exit aperture. The size of the aperture is normally between 5 and 10mm, although care has to be taken that the instrument is not diffraction limited. The shield is coupled to a water cooled jacket. The excess heat generated by the lamp is transferred to the water, which is connected to a water circulator and temperature stabiliser.
The water temperature needs to be stabilised because the IR output of the lamp depends on its operating temperature. Also the two arms of the interferometer have copper pipes around them to stop any thermal fluctuations affecting the path length of the IR beam.

The beam leaving the aperture diverges towards an off-axis parabolic mirror. This then collimates the beam and reflects it through 45° to a plane mirror. The mirror has a small circle of the aluminium removed to allow the

laser beam to pass down the optical axis of the instrument. This is used to align the subsequent optics. The collimated beam then travels towards the beam splitter, where it is divided into the two arms.

3.4 Moving mirror arm

This consists of an optical flat mounted on the end of a high precision micrometer. A 4 phase DC poled stepper motor is used to drive the micrometer in steps of 2.5μm. The number of steps between adjacent sampling points can be chosen to be an integral number of the basic step. This gives control of the step interval, which determines the aliasing zone. The IR beam is deflected through 90° by an optical flat mounted on a vibrating motor. The mirror can be vibrated by applying an A.C voltage to the motor, and so modulate the IR beam. This allows the use of Phase Sensitive Detection techniques to integrate the signal. The amplitude of vibration determines the spectral range in the form of a Bessel function, see Chantry (1971) and Bell (1972). The frequency is matched to the time constant of the detector in use. Therefore the amplitude and frequency of the modulating mirror can be adjusted to suit the requirements of the detector, beamsplitter and filters.

3.5 Reference arm

Because the interferometer is to be used in the dispersive or asymmetrical reflection mode, the sample

replaces one of the mirrors. There are two modules which can be used as the sample/reference arm, depending on the temperature of the measurement to be made. They are :-

(a) Room temperature measurements are performed using a sample plate, held in position by three micrometers. This allows the sample to be aligned accurately using a laser.

(b) Low temperature measurements can be done using a cryostat. This consists of an inner can onto which a block of copper is attached. On one end of this the sample or reference mirror is affixed, usually with silver paint. Outside the can is a vacuum jacket which needs to be pumped to at least 10^{-5} Torr to prevent the sample icing up. The cryostat can either be used with liquid nitrogen at 77K or liquid helium at 4.2K when boiling.

3.6 Output optics

The most common form of output optics is some kind of reflecting arrangement. On this system, after interfering at the beam splitter, the beam is reflected off an optical flat to a spherical mirror. This then condenses the beam to a focus some 10 to 15cm away where the Golay or any other detector sits. Just in front of the focus is room to place various filters, usually black polyethylene. Another method of focusing uses two high density white polyethylene lenses with a focal length of about 5cm. This method suffers because of the thickness of refracting material needed to

converge the beam, which attenuates the higher wave-number response.

3.7 Electronics and control

The pulses used to step the moving mirror are also used to trigger the sample gate of the ADC in the computer. The computer is a Z80 based 8-bit microcomputer built by Transam, and a description of the system has been given by Burton et al (1982).

The analogue signal from the IR detector is fed into a Phase sensitive detector (PSD) made by Brookdeal, model no 9412A. A second input is from the vibrating mirror oscillator, which is fed into the PSD via a phase shifter, model no 421. This is needed so that the phase of the reference and modulated input signal can be matched. The PSD removes the modulation and then integrates the signal, with the output response being determined by a time constant circuit. By scaling the input signal with an attenuation box the output can be scaled to the required 0 to 10 Volt range of the ADC. For the Golay detector the best modulating frequency is around 11 to 16Hz. This usually means step intervals of 1 second or more and a 300ms time constant. The computer then reads the ADC values triggered by the stepper motor, to be stored on magnetic disc for analysis.

3.8 Difficulties

There are three major difficulties that arise using the

methods described, namely

(1) Thermal effect

Both optical arms have to be carefully temperature controlled to negate the effects of thermal fluctuations. With a coefficient of thermal expansion of 25 x 10^{-6} K^{-1} for Aluminium at 300K, and an arm length of at least 100mm, then it follows that the change in length per degree Kelvin will be

$$25 \times 10^{-6}\ K^{-1} \times 100\ mm = 2.5\ \mu m / K$$

So with a change of only 1 degree Kelvin in one arm, the zero path would change by one step interval.

(2) Phase Sensitive Detection

Because of the need to integrate the modulated signal, the sample points are at least 1 second apart, so that a typical run of 1000 points will take over 15 minutes. Even then, at its best, the signal to noise is only about 150 : 1.

(3) Mirror drive

This is where the biggest errors arise. The step length could vary by as much as ± 1μm due to screw and drive errors. One type of error common in micrometers is the appearence of "ghost" lines in the spectra. This can be attributed to the micrometer being bent.

Because of these difficulties a new interferometer was constructed to eliminate the above problems.

3.9 New interferometer

Since the biggest error lay with the stepper motor, the

new drive consists of a hydraulic piston to move the mirror, with laser fringes monitoring the position of the mirror. The new interferometer is shown in figure (3.2). The micrometer was replaced by a high precision cross roller bearing made by E.S.E. Ltd, model no NK3 - 180. The parallelism tolerance is less than 7μm over the complete 10cm travel. Onto this is mounted a 50mm diameter optically flat mirror. Springs were attached to the linear bearing to return the mirror. The bearing is coupled to the piston via a $^1/_4$ inch silver steel rod, which passes through a Wilson vacuum seal. A stainless steel ball was glued to both the linear bearing and the piston to give a better contact. Also the ends of the rod had a machined cone which improved contact. This was necessary to stop the contact point with the rod from varying when scanning. The piston was connected via two nylon pipes to the hydraulic reservoirs and control. This consisted of an air line to switch the hydraulic vane switches, and to drive the piston. Full details of the hydraulic set-up have been given by Burton et al (1984), and all the components were obtained from Activ-Air Automation Ltd. There are two hydraulic needle valves which allow the scan speed to be varied from 1μms^{-1} to 10mms^{-1}. Faster speeds could be obtained by increasing the bore diameter of the piston or by removing the hydraulic fluid.

The other major improvement is in the accuracy of the sampling points. This is achieved by using a Helium-Neon laser, supplied by Scientifica-Cook Ltd, directed down the optic axis of the system, through the etched hole in the

collimator mirror. Because the laser is a monochromatic source, the associated interferogram will be a cosine wave. The variation in intensity is detected by a small photo-diode (RS 305-462) and converted to a voltage. Given that the wavelength of the laser is 632.8nm, the interference fringes will be 316.4nm apart. Since the position of each laser fringe is determined to an accuracy of about 2% of the fringe spacing, this gives a sampling accuracy of 6nm compared to about 1μm for the stepper drive, an improvement of a factor of over 150 in sampling accuracy.

There is also the advantage that the laser shares the same path as the optic axis. This means that if there is any change in the path length of one of the arms due to thermal effects, the laser fringes will automatically compensate. Therefore the need to use temperature stabilisation is redundant.

One other advantage is that the laser fringe intensity can be used as a sensitive method of alignment. When the largest signal is obtained from the photo-diode, the IR signal is also the largest.

Originally, the system was designed with a double sided mirror mounted on the linear drive. A separate laser interferometer was constructed outside the instrument to perform the laser interference. This method was tried but it was found that because the laser channel was independent of the optic axis, thermal drift once more became a problem.

One major difference of continuous scanning compared to

a modulated interferometer is that PSD techniques are not used. This is because each IR component is modulated at a frequency dependent upon the scan speed. This gives rise to a filtering envelope and will be discussed later on in this chapter.

3.10 Electronics

To control the interferometer and acquire data involves three electronic lines, which are :-

(1) Laser fringes (input)

(2) Analogue signal (input)

(3) Hydraulic control (output)

3.10.1 Laser fringes

The laser fringes are detected by a small photo-diode placed inside the output optics chamber. The radiation excites electrons across the band-gap to produce a voltage. This is sent via a feedthrough to a low noise amplifier, Brookdeal type 435. This unit can amplify a signal from a few dB to over 100dB. The input fringes are of the order of 100mV and are amplified to about 700mV. The unit also has a low and a high pass filter. Since the scan speed produces fringes from 100Hz to 1KHz, the low pass filter is set to 100Hz, while the high pass is set to 1KHz. After the amplifier, the signal is sent to a fringe counting unit, see figure (3.3).

The signal is passed through two 741 op-amps, which can

amplify the fringes to 10V. The gain, as well as the D.C. offset, can be varied as required. After the amplifier the signal passes to a Schmidt trigger (TTL 7414) which generates a very sharp rising edge to 5V when the input signal is greater than about 2V. This will convert the cosine wave into a square wave. Also it can be seen that by changing the D.C. offset, the trigger point of the Schmidt can be varied. After the signal has been squared, it can either pass directly to the monostable (TTL 74221) or pass into the counting chain. The chain is constructed of two reversible binary counters (TTL 74193) which are triggered by rising edges. The counters can divide the fringes from 2 to 256, depending on the counter switch. Since each fringe is 316.4nm, this gives control of the spatial separation of the ADC pulses from 316.4nm to 80.998μm. The counted output fringe passes to the monostable (TTL 74221) to generate a narrow 5V trigger pulse. The width of the pulse can be varied by the RC pair to suit the ADC in use. Typically the values of 4.7KΩ and 47nf are used to give a pulse width of 50μs.

3.10.2 Analogue signal

Originally, the output from the IR detector was sent to a PSD unit. At first this was used, but without a reference signal as the beam was not being modulated. This way it acted as a low noise amplifier but with the addition of the time constant switches. This leads to some problems described below

(1) The standard output from a Golay was an A.C swing at the zero path of 5V, while the maximum input to the PSD unit is 150mV. This required the signal to be attenuated by a large factor (≈ 10) so that the PSD was not overloaded.

(2) The PSD electronics were designed to operate at above 10Hz (ie the modulating frequency), whereas the actual modulation frequency of the IR beam is only 1 or 2Hz. So if the PSD is not used in the modulated mode, it will be operating near to the D.C. limit. This has the effect of decreasing the signal to noise ratio.

(3) The electronics generated a mains 50Hz ripple of about 5mV amplitude on the output line, which was inherent to the PSD. This produced a sharp peak in the spectrum corresponding to 50Hz.

Instead of using the PSD, a simple op-amp was constructed as shown in figure (3.4). The circuit works as follows. The input from the detector is divided by 10 using a resistor chain and then coupled to the first amplifier. It was found that this method was better than using a coupling capacitor, as the capacitor would act as an RC circuit and affect the shape of the interferogram. The chain divides a 5V zero path signal on the 18V D.C. offset of the detector, to a 500mV signal on a 2V D.C. offset. This residual offset could be varied by the 5K potentiometer so that the final output D.C. voltage was between 0 and 10V. The signal was amplified by about a factor of 8 using the 39KΩ resistor, which controls the gain of the op-amp. After this, the signal was fed into the second op-amp, which controlled the

final output size of the signal by the use of the 100KΩ potentiometer. A 47nf capacitor was coupled to the output line to filter any high frequency noise propagating up the connecting line from the computer.

Originally two 741 op-amps were used, but these were later upgraded to two 301 op-amps, which have better noise characteristics. Since the amplifier unit is matched to operate with a Golay detector, the signal does not need to be attenuated, as well as having less mains pick-up.

3.10.3 Hydraulic control

The piston of the hydraulic movement is controlled by two relays. By applying 12V across one of the relays it will open, and so allow the compressed nitrogen to push the hydraulic fluid, and so push the piston in one direction. Now by switching the 12V to the other relay, the piston will reverse direction. The computer, via the IEEE interface unit, can generate pulses which can be used to switch states of the relays. These pulses switch the hydraulic direction, via the switching box, through a three stage system, as shown in figure (3.5). This allows the piston to scan forward, stop and change direction, scan backwards, stop and change direction, etc. Because of this, multiple scanning and averaging of the data runs is possible.

3.11 Data aquisition

The IEEE interface unit is a modular system called Microlink, built by Biodata Ltd. It consists of a mainframe with a power supply, which can accomodate 7, 12 or 18 modules, depending on the specifications required. There are at least 20 units available, but for this application only 3 are needed. They are as follows :-

HSC — High speed clock. This is used to trigger the ADC unit from the electronic trigger. It can also be used to multiplex more than one input signal if needed. This gives a maximum data rate of 20 Kilobytes / second.

AN-1 — Analogue signal conditioning. This has a switch to select the input analogue signal from 0.1V to 10V. Also there is a Gain trimmer to set full scale input, and an Offset trimmer to alter the D.C. base level.

A-12D — Analogue to Digital conversion. This converts the analogue signal to a 12 bit digit to be read by the HSC.

To control the input and output of signals from the interface unit, there are a number of commands which can be called up from the computer. These are listed and explained in Appendix 2.

The computer used to control the system is a Sirius computer (now traded under the name of Victor). It has two $5^1/_4$ inch floppy disc drives, each capable of storing about 600 Kilobytes of data, as well as having 512 Kilobytes of memory. All the programs are written in Pascal, although other languages are available.

There are two methods of using the laser fringes to sample the interferogram. Either every laser fringe is used to sample, and then manipulated by the programming to select the appropriate step interval, or the electronic counter is used. Both ways have their advantages and disadvantages, and will be discussed later on in the chapter.

Both methods use the same program, as given in the appendix 2. After the interferogram has been recorded and co-averaged, it is then stored on the floppy disc. The interferogram can either be plotted on the screen, the Hewlett Packard plotter, type 7475a, or sent to the Fourier Transform program. This can either plot the power spectrum, or by using a background and sample interferogram pair, compute the optical constants.

3.12 Ancillary equipment

In the far IR, water vapour is a problem due to its high absorption. This is why most astronomical observations are limited to balloon borne or satellite platforms. To eliminate most of the water absorption, the system is vacuum pumped. A rotary pump is used to rough out the system, producing a pressure of ~ 10^{-1} Torr, which is usually sufficient when operating at room temperature. When the cooled cryostat is to be used, there is a diffusion pump which can produce a pressure of ~ 10^{-5} Torr. This is to stop the sample in the cryostat from icing up, due to residual vapour. Also there is a carbon granual absorption

pump, surrounded by a liquid nitrogen flask. This produces a slightly better vacuum than the rotary pump, about 3 x 10^{-2} Torr, but has the added advantage that it is vibrationless.

The instrument is mounted on an optical table, supported by four gas controlled pneumatic isolation legs, made by Ealing Optics Ltd. The pneumatic legs reduce the effect of floor bound vibrations being transmitted to the instrument.

As mentioned earlier, the lamp has a water jacket to control the thermal response of the IR output.

3.13 Spectral response versus scan speed

The modulation frequency of a given spectral component versus scan speed can be given by the formula below ,

$$S = \frac{f_m}{2} \times \frac{1}{\bar{\nu}_a} \qquad (3.2)$$

where f_m = modulation frequency (Hz)

$\bar{\nu}_a$ = spectral component (cm^{-1})

S = scan speed (cms^{-1})

Since the scan speed is determined by the laser fringe frequency, equation (3.2) can be rewritten as

$$L_f = \frac{f_m}{6.328 \times 10^{-5}} \times \frac{1}{\bar{\nu}_a} \qquad (3.3)$$

where L_f = laser fringe frequency (Hz)

6.328×10^{-5} = laser wavelength (cm)

This function has been plotted for various modulation frequencies, and is shown in figure (3.6). The axes were

chosen to be logarithmic so as to show the various modulation frequencies as straight lines.

From figure (3.6) it can be seen that to operate a Golay detector modulated at about 1Hz in the spectral range of 10 - 1000cm^{-1}, the scan speed would have to be between 10 and 1000 laser Hertz. By varying the scan speed, a given spectral component will be modulated at a different frequency. Figure (3.7) shows the response of a Golay against modulation frequency, with the best response around 1 to 2 Hz. Because of the non-linearity of response to modulation frequency, the spectral throughput varies with scan speed. This is shown in figure (3.8), where a Diamond Golay and a 6.25μm beam splitter have been used for the three scan speeds of 20 Hz, 200 Hz and 800 Hz. As shown in the diagram, the peak response shifts to lower wave-number as the scan speed is increased, as predicted by figure (3.6). Also the power throughput varies, with the peak response when the scan speed is around 150 Hz. However, it has been found that scanning at 2 or 3 times the peak response speed improves the spectrum by filtering out some of the higher wave-number components. This is because as shown in figure (3.7), the response of the Golay decreases very rapidly with modulation frequency. By using figures (3.6), (3.7) and (3.8), the scan speed can be matched to the spectral region of interest.

3.14 Electronic sampling Versus software

As mentioned earlier, there are two methods employed in

sampling the laser fringes. Either every laser fringe is used to sample the data, with a step length of 0.316μm, and then software is used to pick out the required data, or the electronic fringe counter as shown in figure (3.3) can transmit the trigger pulse at the required step interval by counting the laser fringes.

If the laser fringes are counted using the required step interval, it can be shown that there is a cosine decay of the power throughput with wave-number. This effect is shown in figure (3.9), and the throughput decays to $1/\sqrt{2}$ at the maximum wave-number $\bar{\nu}_{max}$, where

$$\bar{\nu}_{max} = \frac{1}{4 \times \Delta x} \qquad (3.4)$$

where Δx = step length in centimeters. The decay is due to the zero path not exactly coinciding when multiple scans are recorded. The difference between the two methods is shown schematically in figure (3.10).

By taking every laser fringe there is no ambiguity in defining the zero path. This is because of the sampling distance being 316.4nm, giving about 10 points across the maxima and minima of the zero path. After the zero path maxima or minima has been defined, the program then selects a certain number of equally spaced points from the data. The number of fringes chosen determines the step interval, and therefore the aliasing zone. The main disadvantage of this method is that because every fringe is stored, very large arrays are needed. The Sirius has a limit of 16000 points which can be stored in an array, which limits the resolution by software control to about $2cm^{-1}$ if 8 fringes

are used per sampling point.

To test the decay experimentally, a low resolution water vapour spectrum (4 cm^{-1} resolution) was recorded. The power throughputs for the two different systems are shown in figure (3.11). Also shown in figure (3.12) is the ratio between the two systems, showing the decay function. As can be seen in figure (3.11), there is no effect in the water vapour structure, while in figure (3.12), the ratio response is in very close agreement to a cosine wave.

3.15 Water vapour testing

To test the whole system, a test material with well known spectral components is needed. The ideal choice is that of water vapour because of the thousands of absorption bands in the I.R. These have been measured and catalogued by various groups, but the results of Rao et al (1966) have been used in this work.

A high resolution run of 0.25 cm^{-1} was taken of water vapour at a pressure of about 10 Torr, and is shown in figure (3.13). Spectral positions for some of the absorption lines are recorded in table (3.1), and are compared to the work of Rao et al. As can be seen, the results agree very well with the reported values for the bands.

3.16 References

Activ-Air Automation Ltd, 30 Station Road, Belmont, Sutton, Surrey.

Bell R.J; "Introductory Fourier transform spectroscopy" Academic Press, New York (1972).

Biodata Ltd, 6 Lower Ormond Street, Manchester.

Brookdeal Electronics Ltd, Market Street, Bracknell, Berkshire.

Burton N.J, Mok C.L and Parker T.J; Int. J. Infrared and Millimetre Waves, 3, 331, (1982).

Burton N.J and Parker T.J; Int. J. Infrared and Millimetre Waves, 5, 803, (1984).

Chantry G.W; "Long wave optics", Academic Press, New York (1984).

E.S.E Ltd, 22-26 Mount Pleasant, Alperton, Middlesex.

Hewlett Packard Ltd, Eskdale Road, Winnersh, Wokingham, Berkshire.

Martin D.H and Puplett E; Infrared Phys, 10, 105, (1970).

Rao K.N, Humphreys C.J and Rank D.H; "Wavelength standards in the infrared", Academic Press, New York, (1966).

R S Components Ltd, 8 Fairway Estate, Green Lane, Hounslow, Middlesex

Scientifica-Cook Ltd, 78 Bollo Bridge Road, Acton, London

Transam components Ltd, 59-61 Theobalds Road, Holborn, London.

Table 3.1

Comparison between reported and experimental (figure 3.13) values for some water vapour absorption lines

Reported values cm^{-1} Ref 1	Experimental values cm^{-1}
100.53	100.6
105.67	105.8
111.11	111.3
121.88	122.0
127.02	126.9
139.02	139.0
150.52	150.6
151.30	151.4
153.46	153.5
170.37	170.4
188.21	188.3
202.60	202.7
208.46	208.5

Ref 1 Rao K.N, Humphreys C.J and Rank D.H; 1966.

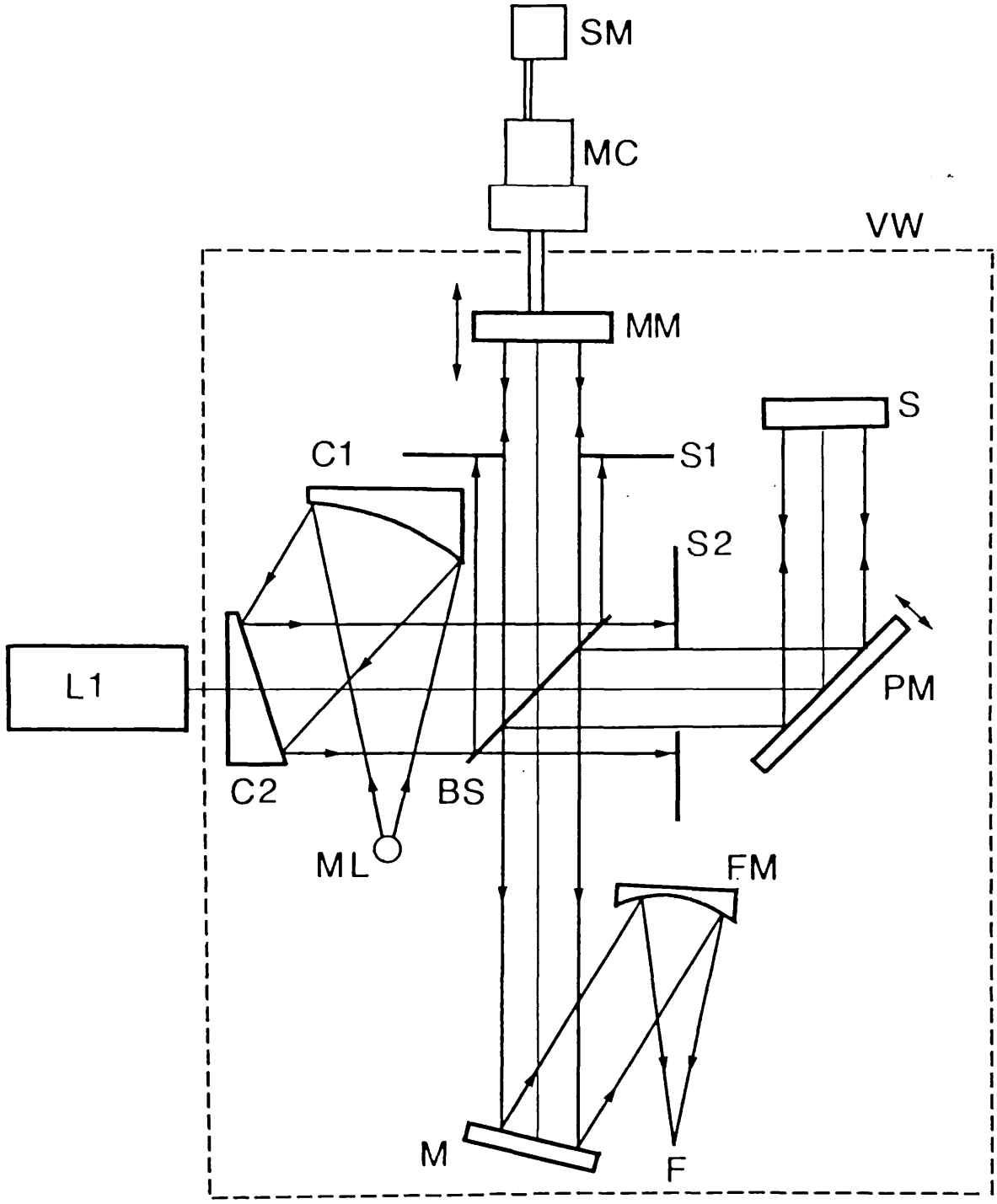

Figure 3.1 Optical layout of step driven interferometer.

Key : SM stepper motor, MC micrometer, MM moving mirror
S1,S2 optical stops, PM phase modulated mirror
C1,C2 collimating mirrors, BS beam splitter
ML mercury lamp, FM focussing mirror, F focus
S sample, L1 aligning laser, VW vacuum wall

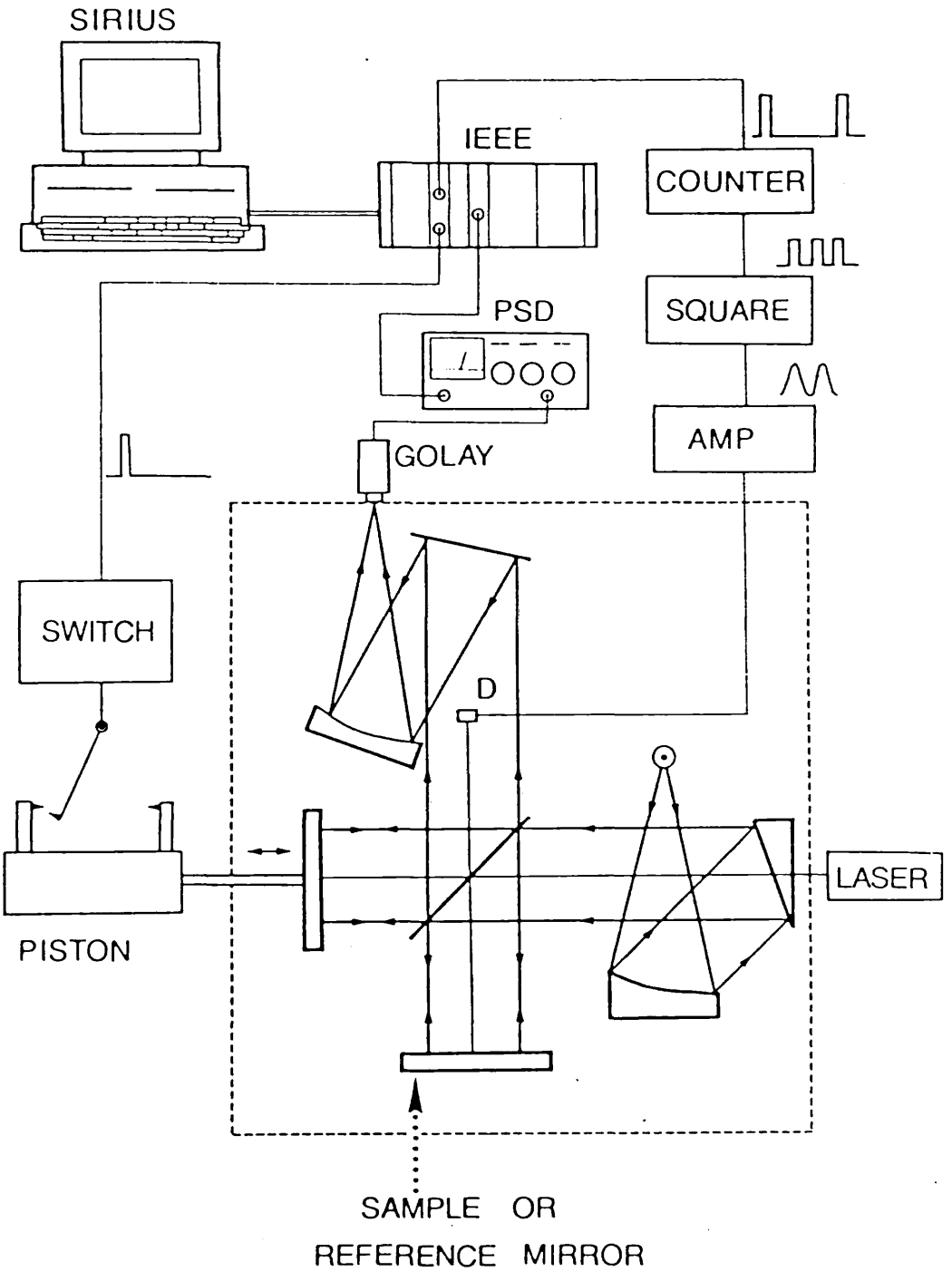

Figure 3.2 Diagram of the new hydraulically controlled interferometer.

Key : D laser diode detector.

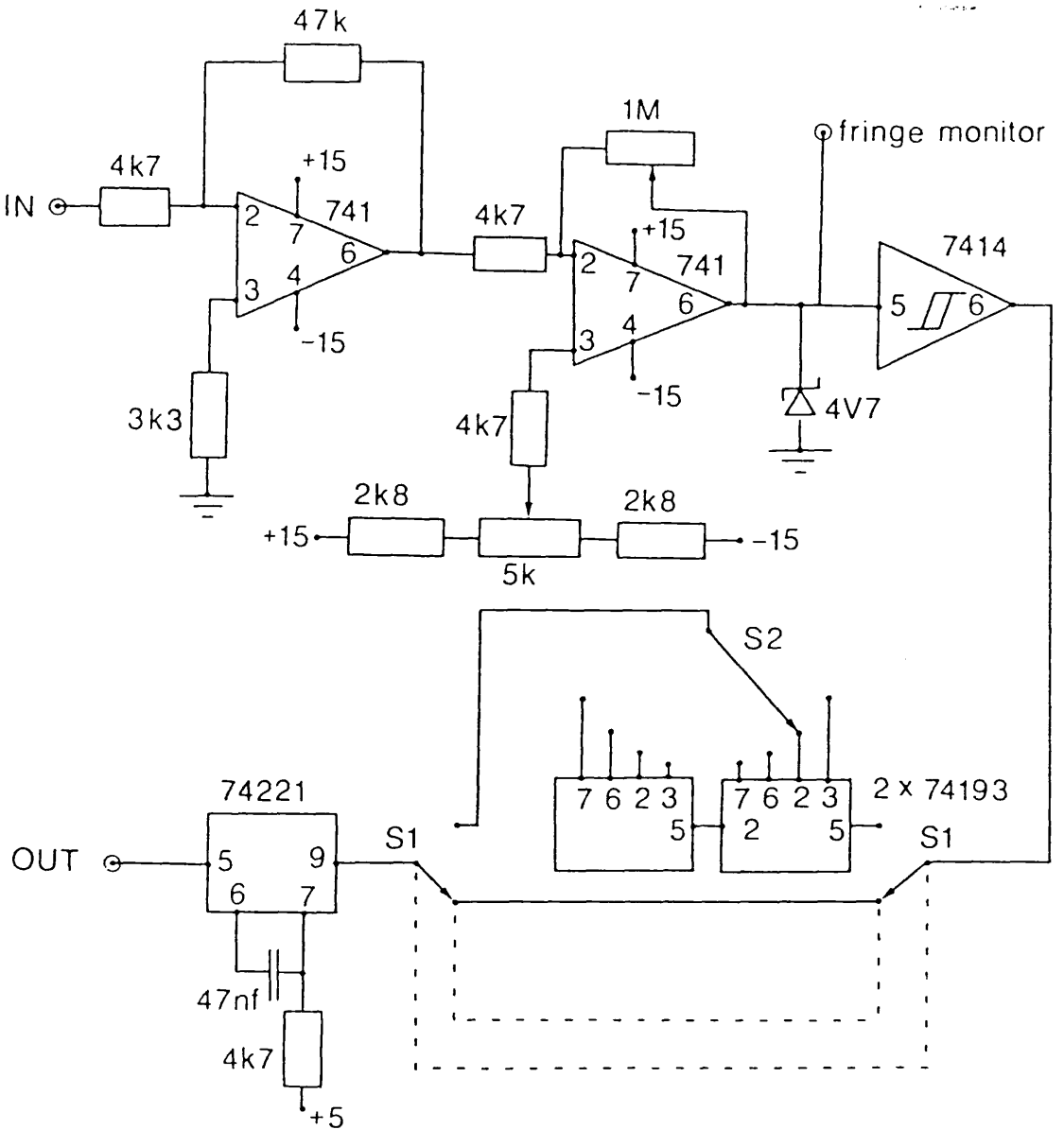

Figure 3.3 Laser fringe amplifier and counting circuit diagram.

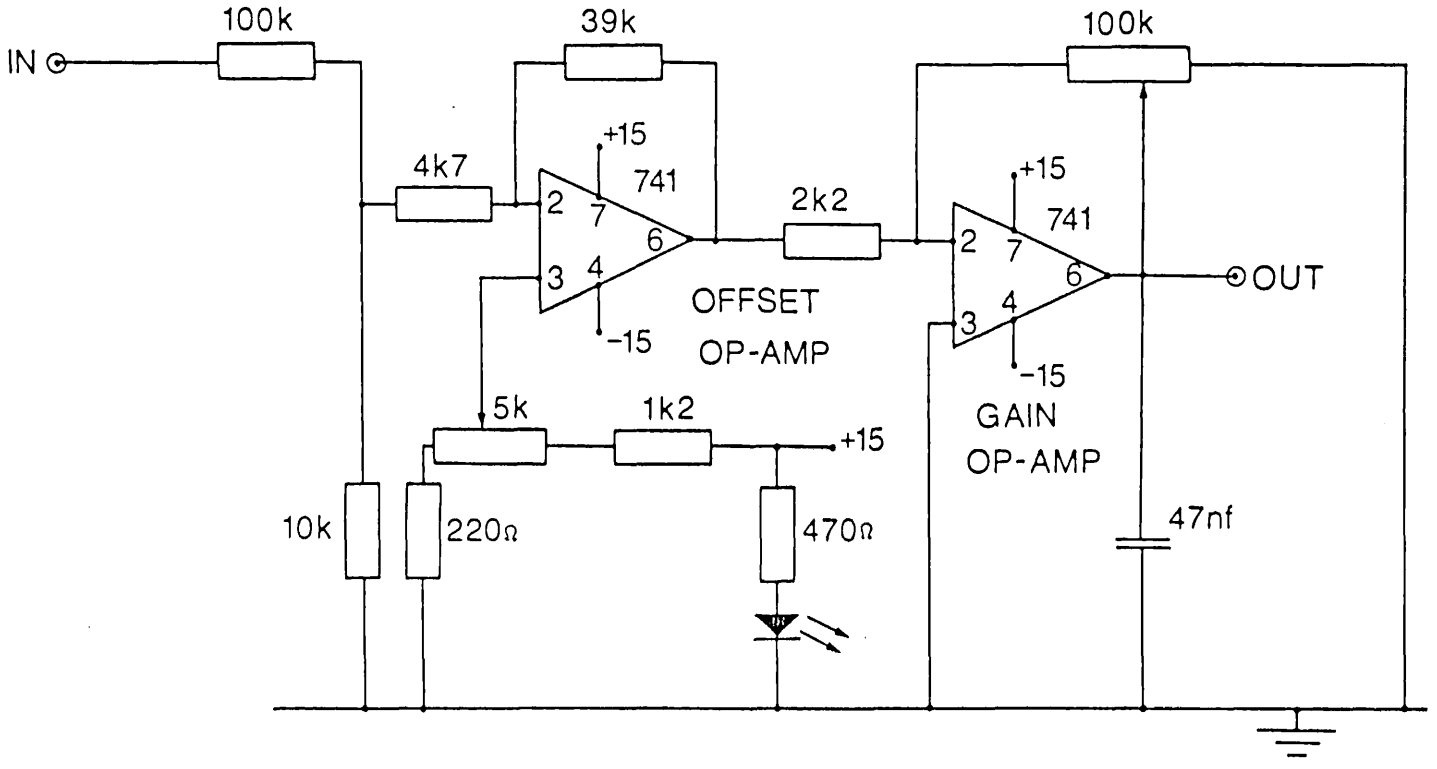

Figure 3.4 Circuit diagram of the amplifier for the infrared detector

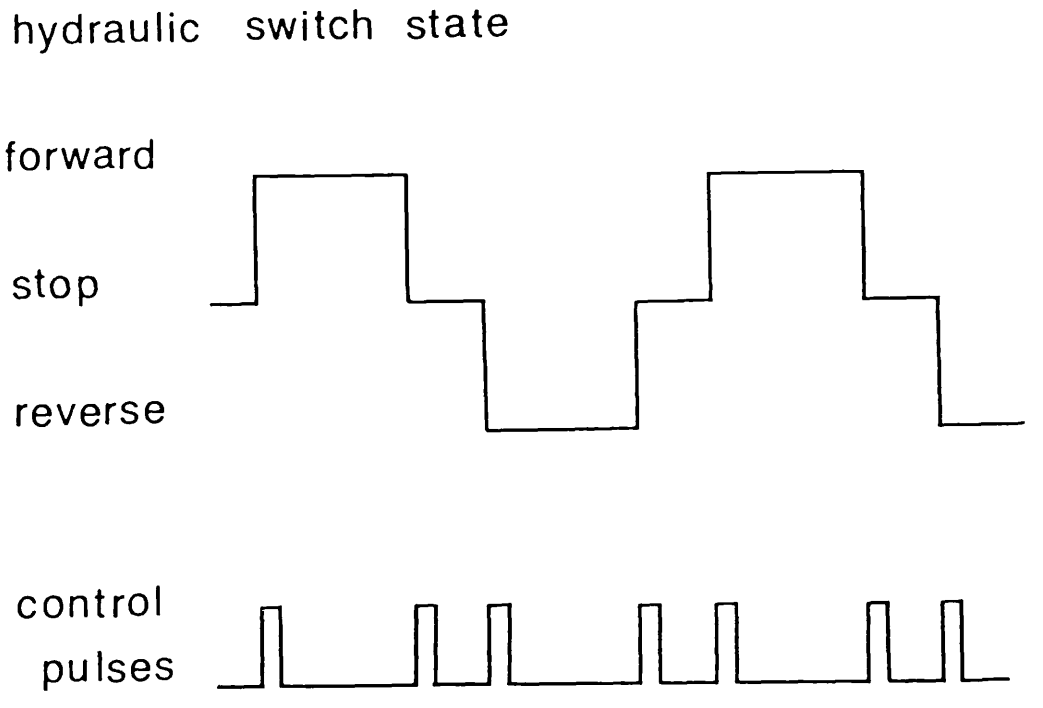

Figure 3.5 Schematic diagram showing the control of the hydraulic piston direction.

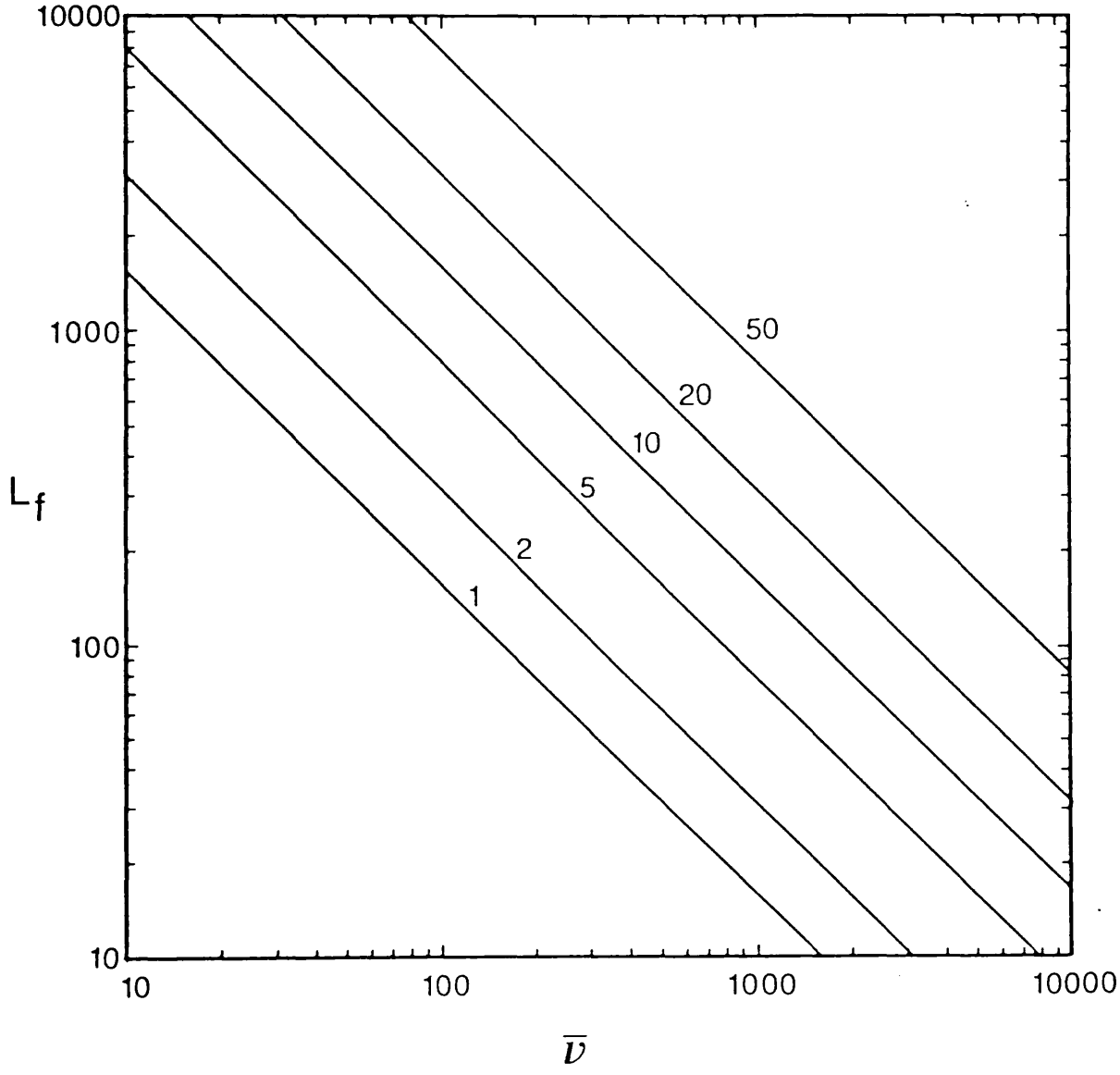

Figure 3.6 Plot of laser fringe frequency L_f versus wavenumber $\bar{\nu}$ for various infrared modulation frequencies.

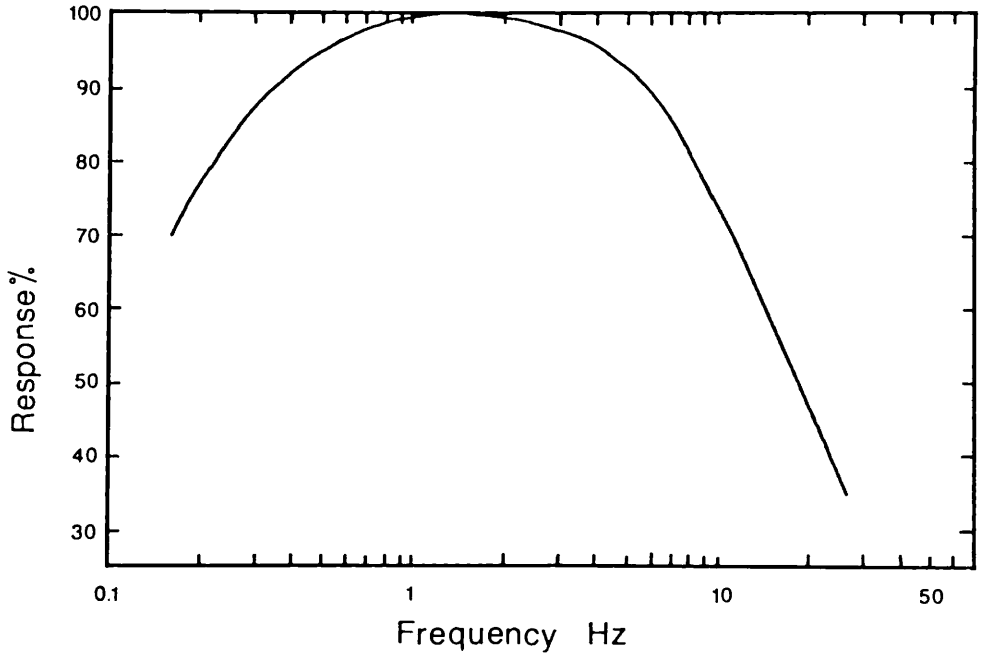

Figure 3.7 Plot of absolute response versus frequency of modulated infrared signal for a Golay detector.

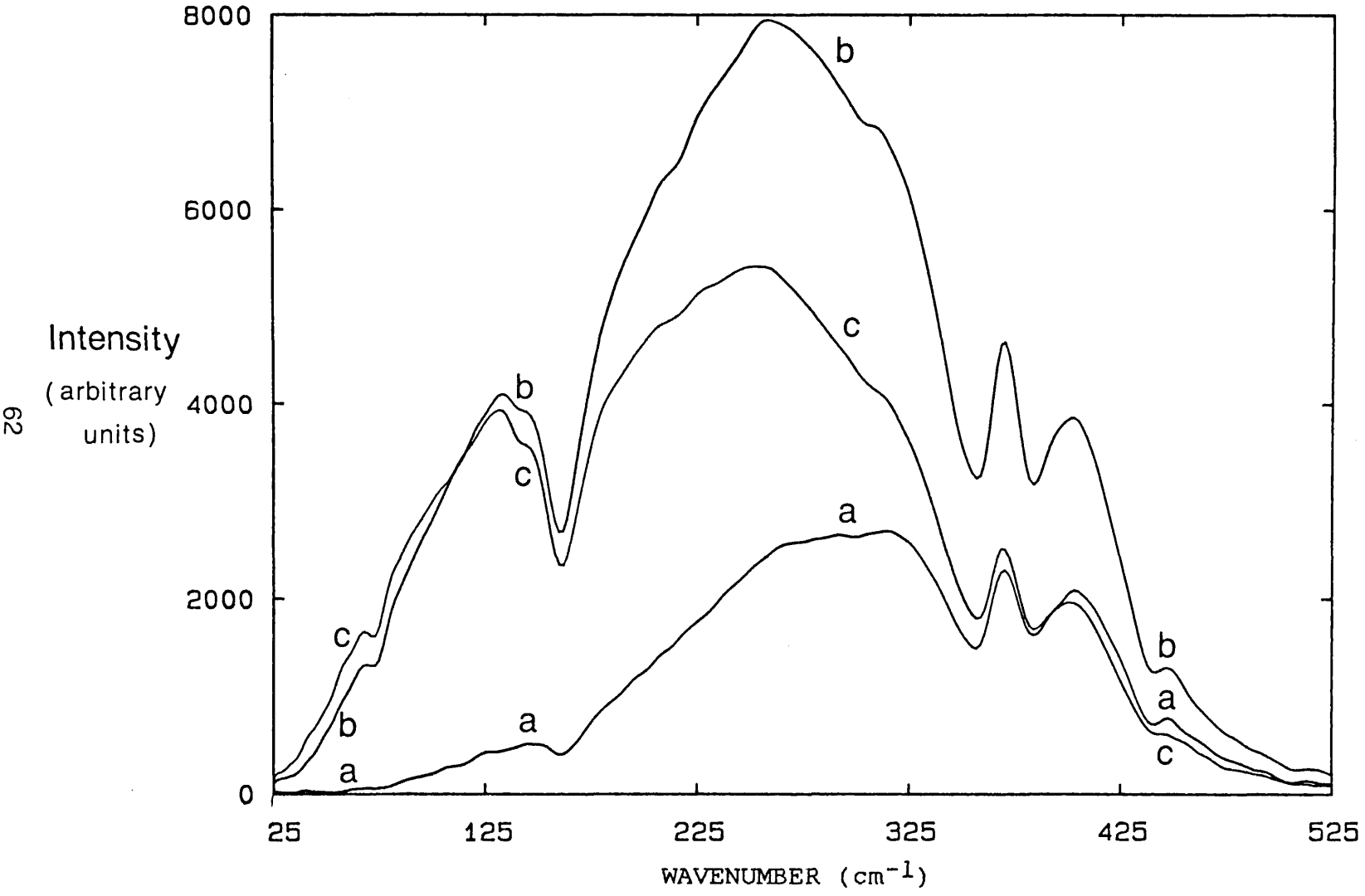

Figure 3.8 Spectral response versus fringe frequency (a) 20 Hz (b) 200 Hz (c) 800 Hz

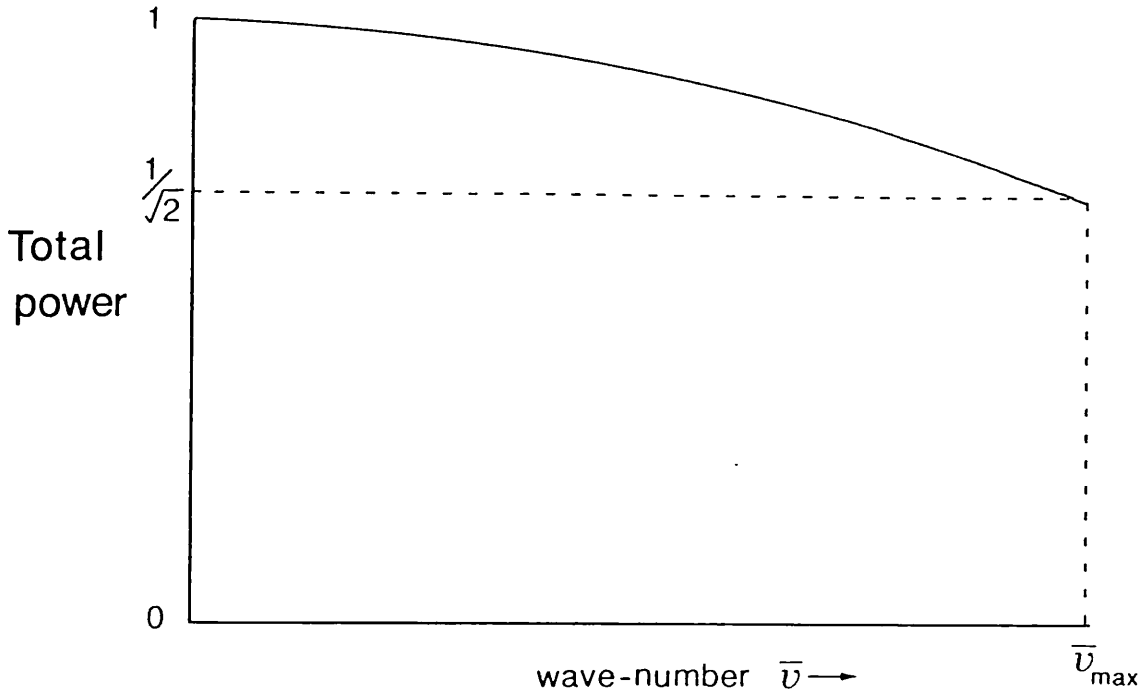

Figure 3.9 Spectral decay due to the mis-match of zero paths when co-averaging numerous interferograms

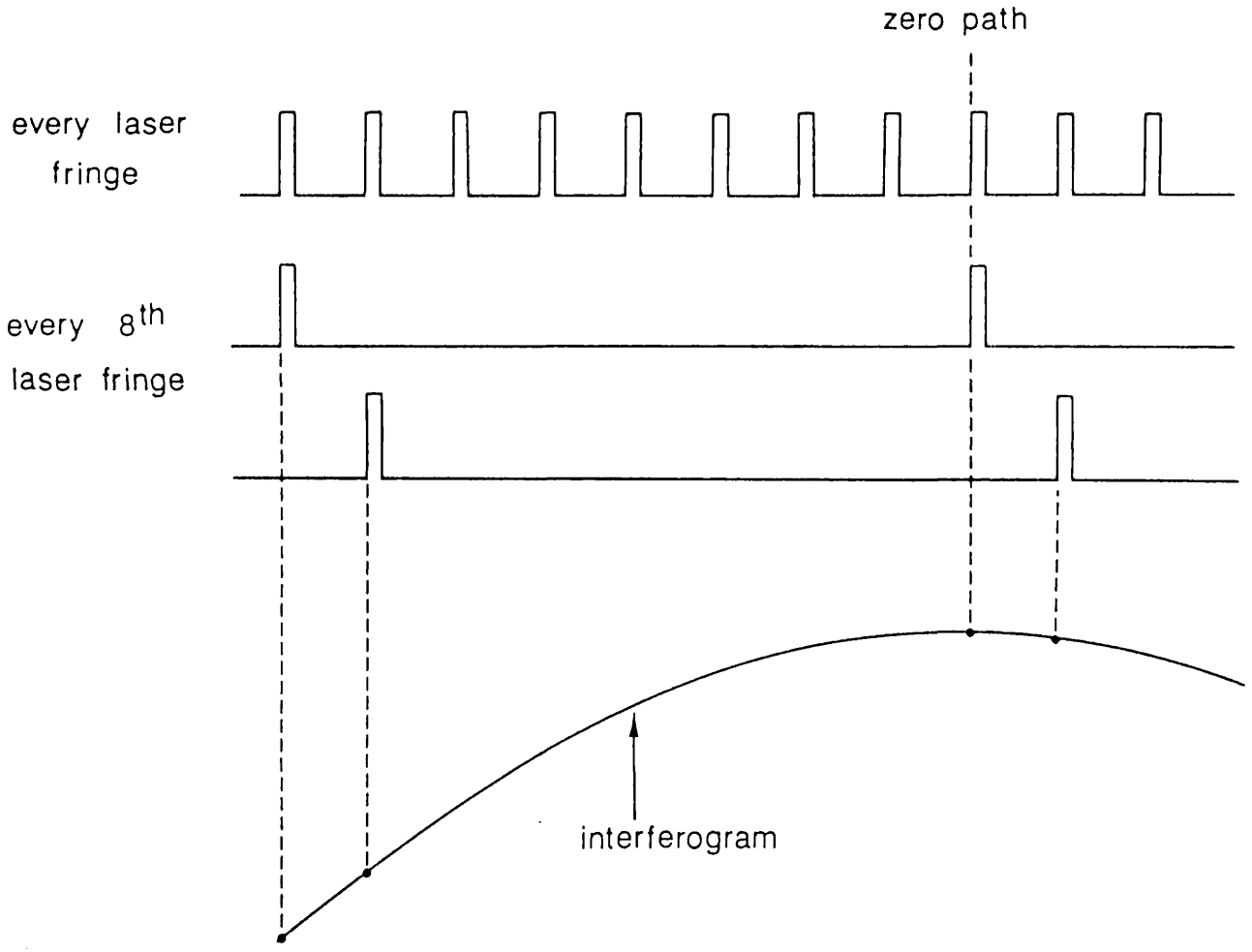

Figure 3.10 Schematic diagram showing the difference between electronic and software sampling

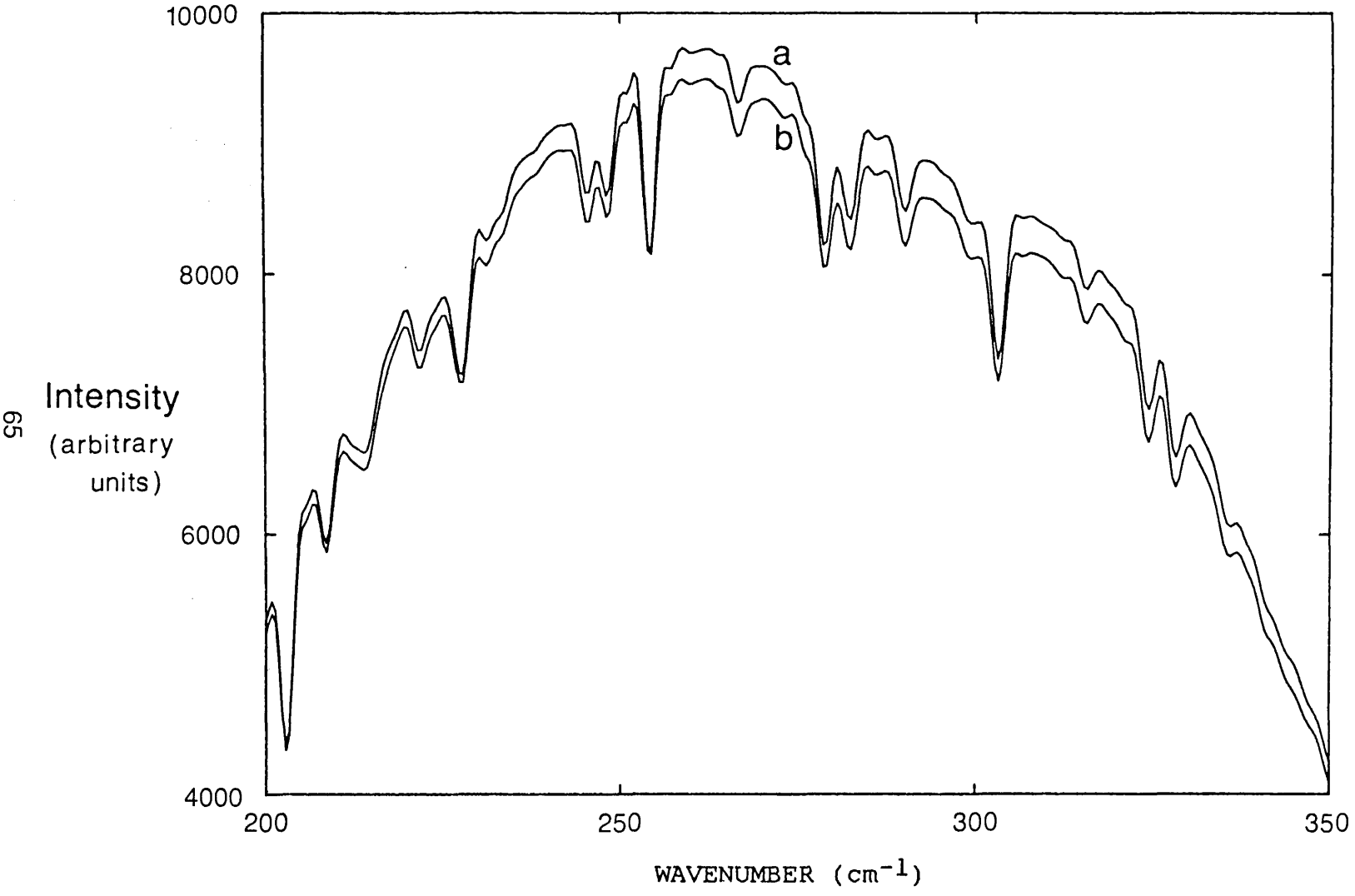

Figure 3.11 Water vapour spectra comparing software (a) with electronic (b) counting

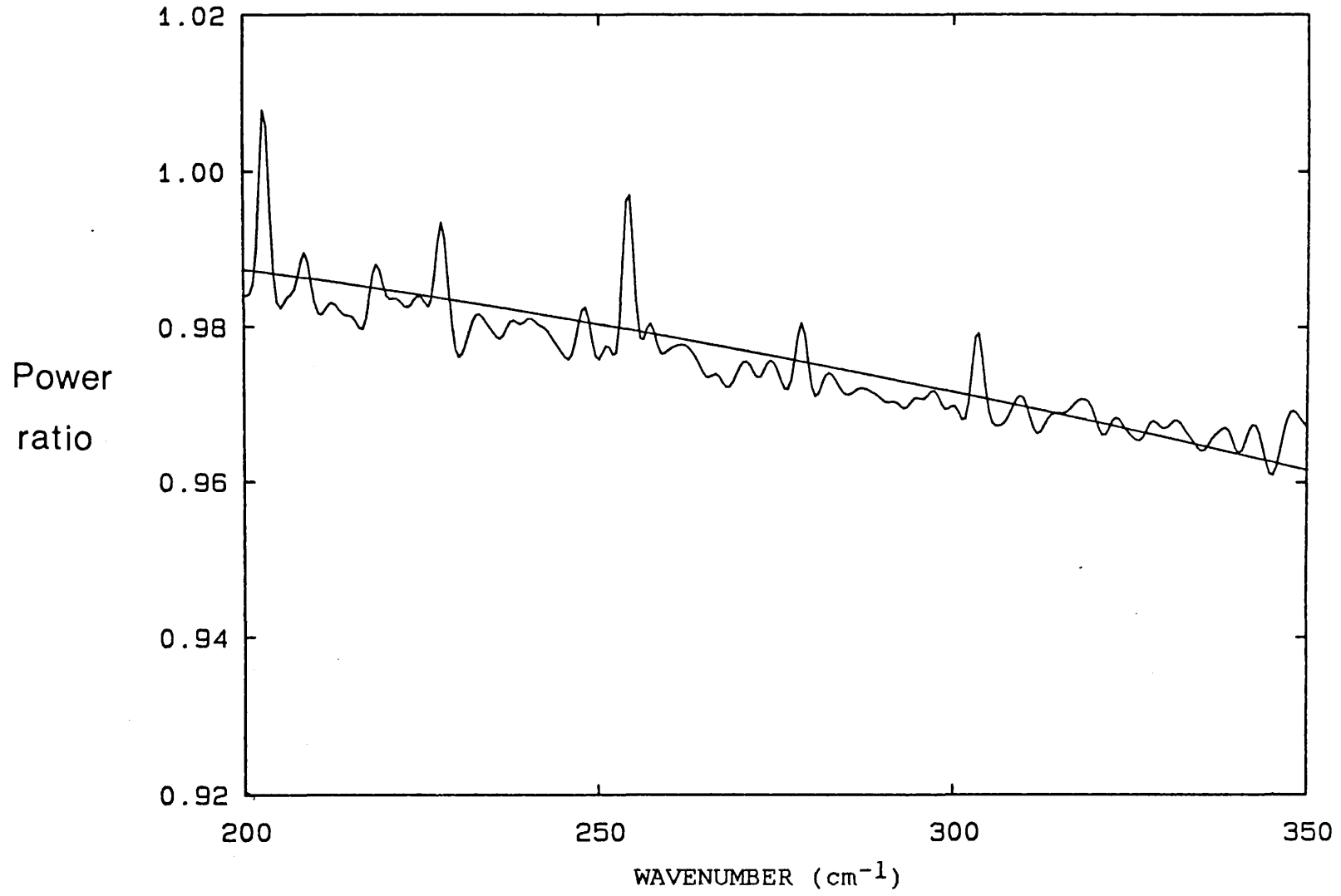

Figure 3.12 Ratio between software and electronic sampling, compared to a cosine function

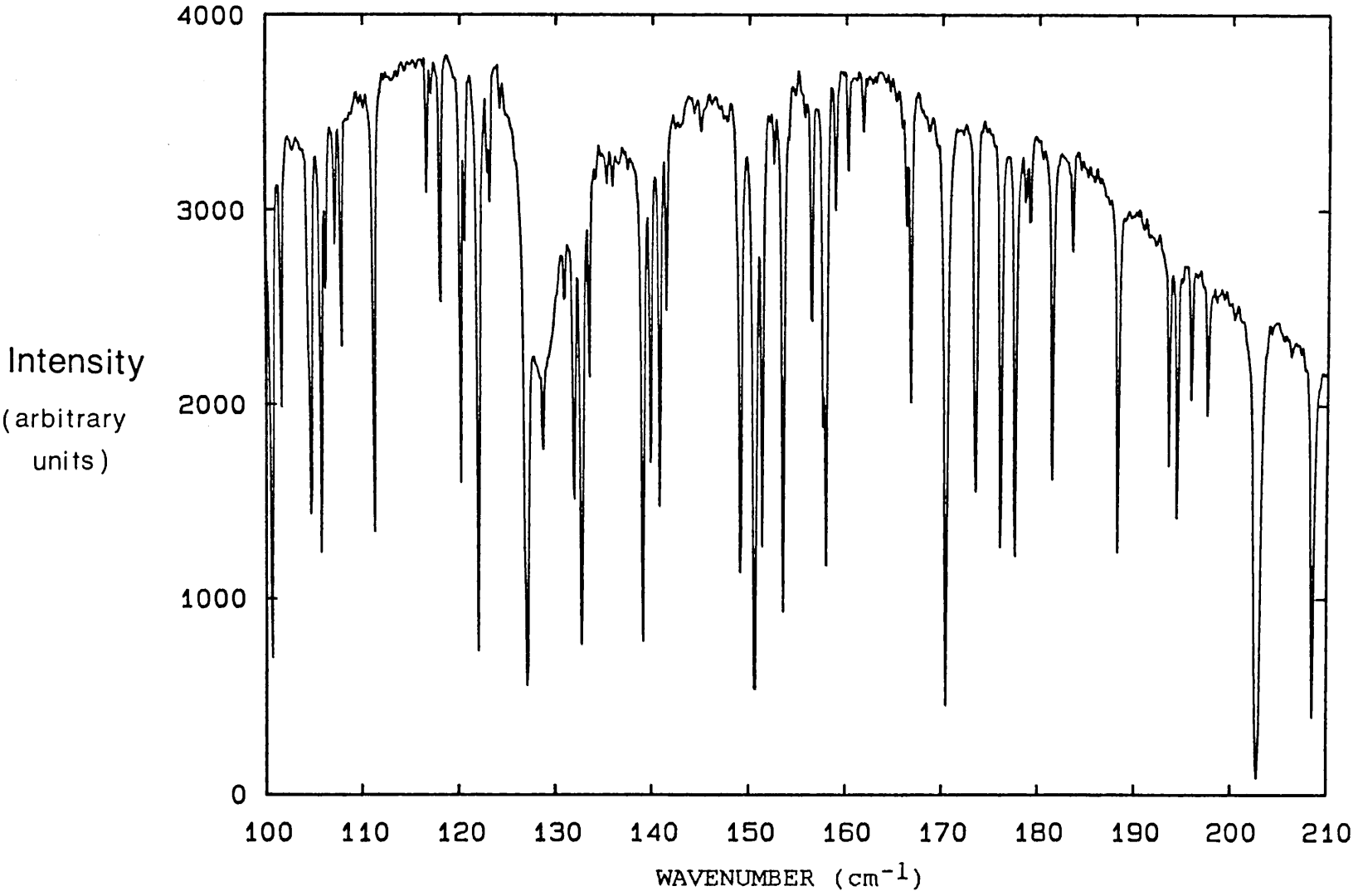

Figure 3.13 High resolution (0.25 cm^{-1}) water vapour spectrum

CHAPTER 4

Optical response of Solids in the Far infrared

4.1 Introduction

The main features of the lattice dispersion curves of simple crystalline solids can be calculated using a linear chain model. This can be generalised to three dimensions, which introduces longitudinal and transverse waves. Electromagnetic radiation of about 10^{13} Hz ($\nu \approx 300 cm^{-1}$) can couple to the transverse optic phonon modes within the sample. This interaction can be examined by using a simple rigid ion model in the long wavelength limit to give the main features of the far infrared dielectric response $\epsilon(\omega)$. From this function it can be shown that within a frequency band between the transverse and longitudinal optic modes strong reflection occurs known as the Reststrahlen band. Then by the use of a quantum mechanical perturbation model for the decay of this resonance, the anharmonic self-energy function Γ results. This can be used to show small features in the spectra due to phonon combination modes.

4.2 Dispersion relation

It can be shown (Kittel 1976) that with a simple linear chain model of two atoms per primitive cell, with masses M_1

and M_2, lattice spacing a, and a spring constant of C, two branches occur in the dispersion curve. They are known as the acoustic and optic branches, and are shown in figure (4.1). Also shown on the diagram is the wavevector for electromagnetic radiation.

If there are p atoms in the primitive cell, there will be 3p branches in total. These will be divided into 3p-3 optical branches, and 3 acoustic branches. This gives rise to 3 optical and 3 acoustic branches for the Zinc blende lattices with two atoms per primitive cell. Both branches will consist of two transverse modes and one longitudinal mode. If the wavelength of the optical phonons is large ($\approx$ 100μm), then it can be seen that the positive sub-lattice moves out of phase with the negative sub-lattice. This gives rise to a change in the charge density, which can allow radiation to couple with this induced dipole. The coupled phonon-photon interaction is called a Polariton.

Consider the lattice to be composed of rigid ions, with charges of +e and -e (as with 3-5 materials), then the polarization per unit volume $\underline{P}$ is given by

$$\underline{P} = N e \underline{u} \qquad (4.1)$$

where N = number of ions per unit volume

$\underline{u}$ = induced displacement

The interaction of radiation when the wavevector K $\approx$ 0 is where the two dispersion curves for light and optical lattice waves intersect, allowing the phonons to couple with the photons to give the polariton interaction. To see how the coupling between photons and phonons affects the optical properties, the derivation of the dielectric

response is needed.

4.3 Dielectric response

It has been seen in chapter 2 that at the intersection of the photon and phonon dispersion curves, the two sub-lattices vibrate out of phase. This will give two equations of motion

$$M_1\ddot{u}_+ = -\beta(u_+ - u_-) + eE \qquad (4.2)$$

$$M_2\ddot{u}_- = -\beta(u_- - u_+) + eE \qquad (4.3)$$

where E = local electric field

β = restoring force

This will give

$$M\ddot{u} = -\beta u + eE \qquad (4.4)$$

where $M = \dfrac{M_1 M_2}{M_1 + M_2}$ = reduced mass

$u = u_+ - u_-$ = induced displacement

Equation (4.4) is the equation of motion for the lattice, but ignoring any damping. This can be included by adding a damping term, as well as the time dependence of the electric field $E = E_0 e^{i\omega t}$:-

$$M\ddot{u} + M\Gamma\dot{u} + \beta u = eE_0 e^{-i\omega t} \qquad (4.5)$$

where Γ is a frequency independent damping coefficient

Now assume that $u = u_0 e^{-i\omega t}$, so that the solution is

$$u_0 = \frac{(eE_0/M)}{\omega_0^2 - \omega^2 - i\omega\Gamma} \qquad (4.6)$$

where $\omega_0 = \left(\frac{\beta}{M} \right)^{\frac{1}{2}}$ = natural frequency of the undamped system

From equation (4.1), the polarisation P will be given by

$$P = \frac{(Ne^2/ M)\ E_0 e^{-i\omega t}}{\omega_0^2 - \omega^2 - i\omega\Gamma} \qquad (4.7)$$

But from the definition of polarisation, we have

$$P = \epsilon_0 \chi E$$

where χ = dielectric susceptibility, and therefore

$$\chi = \frac{(Ne^2/ M\epsilon_0)}{\omega_0^2 - \omega^2 - i\omega\Gamma} \qquad (4.8)$$

Using the results obtained earlier (equations 2.44 and 2.45) that the real part of the dielectric constant is

$$\epsilon' = 1 + \chi'$$

we obtain

$$\epsilon' = 1 + \frac{\omega_0^2\ S\ (\omega_0^2 - \omega^2)}{(\omega_0^2 - \omega^2)^2 + \omega^2\Gamma^2} \qquad (4.9)$$

and the imaginary part

$$\epsilon'' = \chi''$$

$$\epsilon'' = \frac{\omega_0^2\ S\ \omega\Gamma}{(\omega_0^2 - \omega^2)^2 + \omega^2\Gamma^2} \qquad (4.10)$$

where $S = \frac{Ne^2}{M\epsilon_0\omega_0^2}$ = oscillator strength

To examine how the coupling between photons and phonons affects the dielectric response, we need to compare the expression above to that for light. To simplify the

analysis let the damping $\Gamma = 0$. From Maxwell's equation (Kittel 1976) it is known that

$$\frac{\omega}{K} = \frac{c}{\sqrt{\epsilon}} = v_p = \text{phase velocity} \qquad (4.11)$$

$$\text{i.e} \qquad \epsilon = \frac{K^2c^2}{\omega^2} \qquad (4.12)$$

For the lattice wave, with $\Gamma = 0$, equation (4.10) will give $\epsilon'' = 0$, so that except for when $\omega = \omega_0$

$$\epsilon' = 1 + \chi' = 1 + \frac{\omega_0^2 S}{\omega_0^2 - \omega^2} \qquad (4.13)$$

Using equations (4.12) and (4.13), this allows the two equations to be solved simultaneously

$$\frac{K^2c^2}{\omega^2} = 1 + \frac{\omega_0^2 S}{\omega_0^2 - \omega^2} \qquad (4.14)$$

This gives an expression of K versus ω, a dispersion relation

$$K^2c^2 = \omega^2 \left[\frac{\omega_0^2 - \omega^2 + \omega_0^2 S}{\omega_0^2 - \omega^2} \right] \qquad (4.15)$$

Now let $\omega_0^2(1 + S) = \omega_1^2$ (4.16)

where $(1 + S) = \epsilon_0$, so equation (4.15) becomes

$$K^2 = \frac{\omega^2}{c^2} \left[\frac{\omega_1^2 - \omega^2}{\omega_0^2 - \omega^2} \right] \qquad \underline{\omega \text{ Vs } K} \qquad (4.17)$$

and

$$\epsilon' = \left[\frac{\omega_1^2 - \omega^2}{\omega_0^2 - \omega^2} \right] \qquad \underline{\omega \text{ Vs } \epsilon} \qquad (4.18)$$

These functions can be examined by taking various limits of the frequency ω.

As $\omega \to 0$, $K^2 \to \frac{\omega^2 \epsilon_0}{c^2}$

when $\omega^2 = \omega_1^2$, $K^2 = 0$,

when $\omega^2 = \omega_0^2$, $K^2 = \infty$

when $\omega^2 \to \infty$, $K^2 \to \frac{\omega^2}{c^2}$

and when $\omega_0^2 < \omega^2 < \omega_1^2$, K^2 is negative, so that K is imaginary. Figures (4.2) and (4.3) show the dispersion curves and the real part of the dielectric response when there is the polariton interaction. It has been shown earlier that ω_0 is the resonance frequency when there is no coupling. This is equivalent to the transverse optic mode ω_t. It now remains to find a physical interpretation for ω_1.

For the transverse phonon mode the particle motion is perpendicular to the wavevector K, which means div E = 0. But for the longitudinal mode the particle motion is parallel to K. This means that the polarisation P is also parallel to K, so div E $\neq$ 0. So for this case ϵ = 0, which reduces equation (4.13) to

$$\omega_0^2 - \omega^2 + \omega_0^2 S = 0 \qquad (4.19)$$

Then the identity from equation (4.13) can be used to show

$$\omega^2 = \omega_0^2 (1 + S) = \omega_1^2 \qquad (4.20)$$

This means that ω_1 is the frequency of the longitudinal optic mode. The model used so far is usually known as a Rigid Ion Model because no account has been made for the electronic polarisation. Because of this, the model predicts that the real dielectric response would tend at

the high frequency limit ϵ_∞ to 1. The electronic polarisation can be accounted for phenomenologically by using the high frequency limit ϵ_∞ of the dielectric response in equation (4.13), as shown below

$$\epsilon' = \epsilon_\infty + \frac{\omega_0^2 S}{\omega_0^2 - \omega^2} \qquad (4.21)$$

So at $\omega = 0$, $\epsilon_0 = \epsilon_\infty + S$

Therefore $S = \epsilon_0 - \epsilon_\infty$, and so

$$\epsilon' = \epsilon_\infty + \frac{\omega_0^2 (\epsilon_0 - \epsilon_\infty)}{\omega_0^2 - \omega^2} \qquad (4.22)$$

From equation (4.19) and (4.20), it can be shown that when $\epsilon = 0$, $\omega = \omega_1$, which reduces equation (4.22) to

$$\epsilon_\infty \omega_0 - \epsilon_\infty^2 \omega_1 + \omega_0^2 (\epsilon_0^2 - \epsilon_\infty) = 0 \qquad (4.23)$$

which give the famous Lyddane-Sachs-Teller (LST) relationship

$$\frac{\omega_1^2}{\omega_0^2} = \frac{\epsilon_0}{\epsilon_\infty} \qquad (4.24)$$

as given in their paper (1941).

From equation (4.18) it was seen that between ω_0 and ω_1 the real part of the dielectric response was negative. This gives the result that $N = \sqrt{\epsilon}$ is imaginary and so waves cannot propagate into the material, giving rise to a spectral region of high reflectivity, called the Reststrahl. The reflectivity R at normal incidence is given by

$$R = \left| \frac{1 - \tilde{N}}{1 + \tilde{N}} \right|^2 \qquad (4.25)$$

with $\tilde{N} = n + ik$ and $\tilde{\epsilon} = \epsilon' + i\epsilon''$

When $\tilde{\epsilon}$ is real but negative, $\tilde{N} = iK$, since $n = 0$ and thus $R = 1$. When $\tilde{\epsilon} = 1$, $N = 1$ and then $R = 0$. This give the function as shown in figure (4.4) in the case of no damping.

4.4 Anharmonicity and the dielectric response

The equation for the dielectric response is given in equation (4.22), but with the frequency independent damping coefficient Γ, giving

$$\tilde{\epsilon}(\nu) = \epsilon_\infty + \frac{(\epsilon_0 - \epsilon_\infty)\,\omega_0^2}{\omega_0^2 - \omega^2 - i\Gamma\omega} \qquad (4.26)$$

where ω_0 is the oscillator frequency (the frequency of the tranverse optic mode), ϵ_0 and ϵ_∞ are the static and limiting values of the dielectric constant, and the term $(\epsilon_0 - \epsilon_\infty)$ is the oscillator strength. This model is not capable of explaining any structure seen on the spectrum because it ignores any interactions in the decay of the TO resonance. To deal with this, perturbation theory is used to account for phonon-phonon interactions. Cowley (1963) has shown that these interactions can be taken into account by writing the response as

$$\tilde{\epsilon}(\nu) = \epsilon_\infty + \frac{(\epsilon_0 - \epsilon_\infty)\,\omega^2(oj)}{\omega^2(oj) - \omega^2 + 2\omega(oj)[\Delta(oj,\omega) - i\Gamma(oj,\omega)]} \qquad (4.27)$$

where $\Delta(oj,\omega)$ and $\Gamma(oj,\omega)$ are the real and imaginary parts of the anharmonic self-energy function of the transverse optic phonon. The real part can be written as a

sum of two components, as given below

$$\Delta(oj,\omega) = \overset{E}{\Delta}(oj) + \overset{A}{\Delta}(oj,\omega) \tag{4.28}$$

where the term $\overset{E}{\Delta}(oj)$ is frequency independent and arises due to thermal expansion, while the term $\overset{A}{\Delta}(oj,\omega)$ is frequency dependent and is due to anharmonic interactions. By using equation (4.27) it can be shown that the real and imaginary parts of the anharmonic self-energy function can be written as

$$\overset{A}{\Delta}(oj,\omega) = \frac{1}{2}\left\{\omega(oj)\left[(\epsilon_0 - \epsilon_\infty)\eta'(\omega) - 1\right] + \frac{\omega^2}{\omega(oj)}\right\} - \Delta(oj) \tag{4.28}$$

$$\Gamma(oj,\omega) = -\frac{1}{2}\omega(oj)(\epsilon_0 - \epsilon_\infty)\eta''(\omega) \tag{4.29}$$

where $$\eta'(\omega) = \frac{\epsilon'(\omega) - \epsilon_\infty}{[\epsilon'(\omega) - \epsilon_\infty]^2 + \epsilon''(\omega)^2} \tag{4.30}$$

and

$$\eta''(\omega) = \frac{-\epsilon''(\omega)}{[\epsilon'(\omega) - \epsilon_\infty]^2 + \epsilon''(\omega)^2} \tag{4.31}$$

The interactions between phonons which accompany the decay of the TO phonon give rise to features in the amplitude and phase. These features can be studied more conveniently by using the more sensitive function Γ to observe the summation and difference phonon combinations. By the use of critical point analysis of the lattice dispersion curves for these zincblende structure crystals, the experimental data can be compared to the expected values for the phonon bands. The measured features can also be compared to the results from various lattice dynamical models like the

Rigid Ion Model or the Shell model. This can provide additional evidence to support the model as well as describing phonon frequencies at certain critical points like W, which have not yet been obtained from neutron scattering data.

4.5 Free Carrier Absorption

The samples studied are usually referred to as being "pure". This is only true in so far as the concentrations of impurities (site defects, interstitials etc) have been reduced to the state of the art limit. By careful growth and refining methods this limit is normally about 10^{14} cm^{-3}. The concentration of impurities gives rise to a carrier concentration of charges which are very loosely bound to the lattice sites. These free carriers can behave like an electron gas, with a dielectric response as given in Kittel (1979) in S.I. unit as

$$\epsilon'(\omega) = 1 - \frac{ne^2}{\epsilon_0 m_* \omega^2} \qquad (4.32)$$

where n = carrier concentration

m_* = effective mass of the free carrier

ϵ_0 = permittivity of free space

This equation defines the Plasma Frequency as

$$\omega_p^2 = \frac{ne^2}{\epsilon_0 m_*} \qquad (4.33)$$

From these results it can be shown that at frequencies below the plasma frequency the dielectric function $\epsilon'(\omega)$ is

negative. This means that electromagnetic waves cannot propagate, and hence are totally reflected. Also it can be shown that when $\epsilon'(\omega) = 0$, $\omega = \omega_p$. Equation (4.33) can be rewritten in terms of wavenumber, and is given by

$$\bar{\nu}^2 = 8.9 \times 10^{-14} \frac{n}{m_*} \qquad (4.34)$$

where n = carrier concentration per cm^{-3}

m_* = mass of free carriers in electron masses

$\bar{\nu}$ = plasma frequency in wavenumbers

4.6 References

Cowley R.A; Adv Phys, 12, 421, (1963).

Kittel C; "Introduction to solid state physics", Wiley & Sons Inc, New York (1976).

Lyddane R.H, Sachs R.G and Teller E; Phys.Rev, 59, 673, (1941).

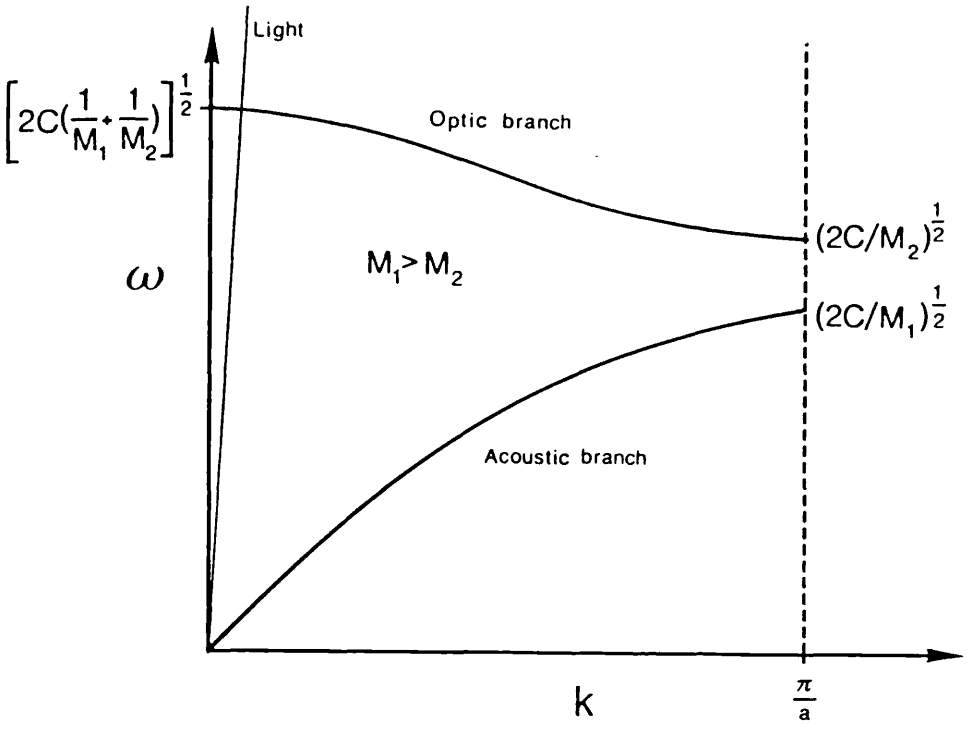

Figure 4.1 Diagram showing the dispersion curves for a diatomic linear chain, with masses M_1 and M_2, force constant C and an atomic seperation a.

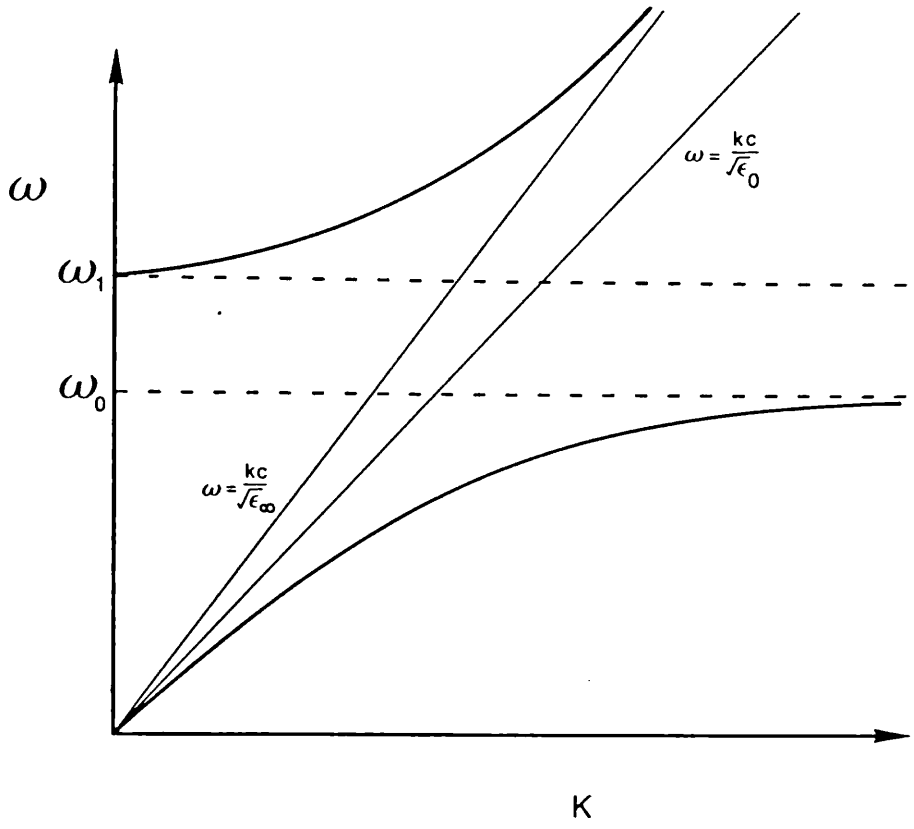

Figure 4.2 Diagram showing the dispersion curves for transverse electromagnetic modes (polaritons) propagating in a diatomic ionic crystal.

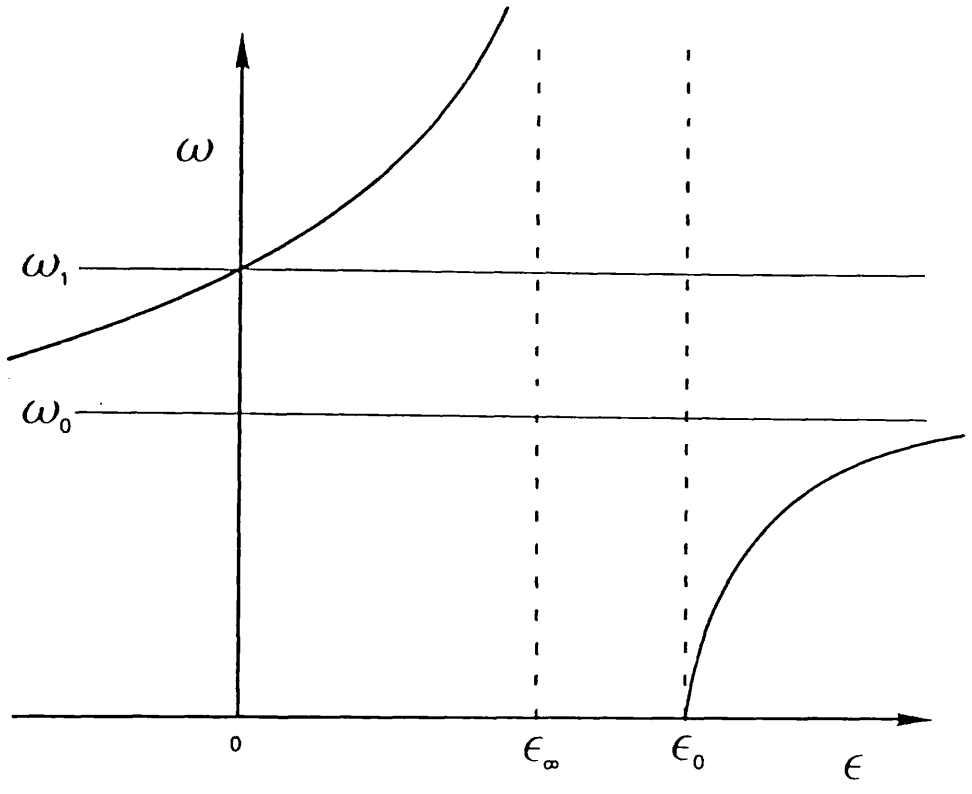

Figure 4.3 Diagram of the real part of the frequency dependent dielectric function in the region of the polariton interaction.

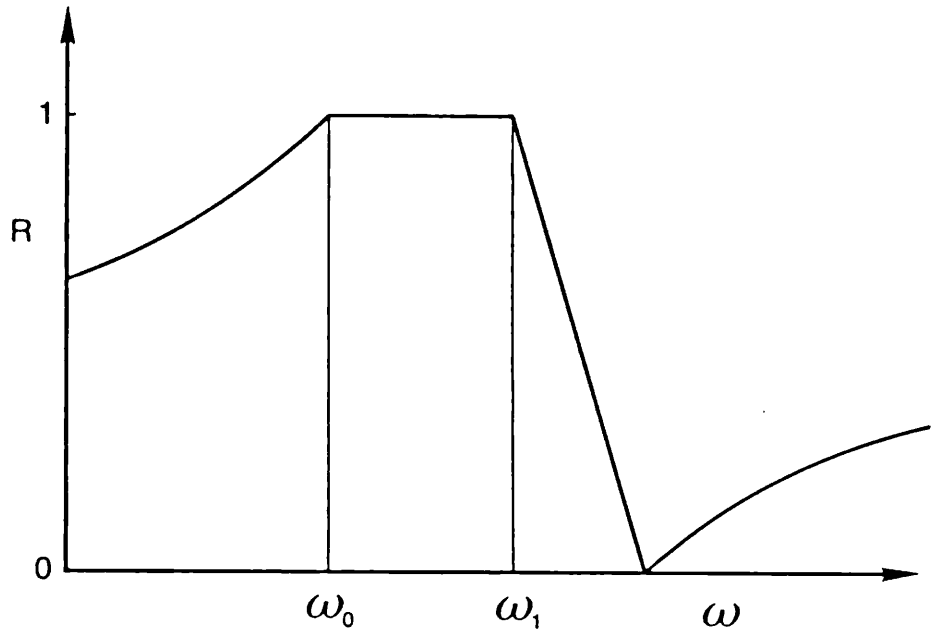

Figure 4.4 Diagram of the reflectivity R within the region of the polariton interaction. The frequency of ω_0 is the transverse optic mode at the zone centre, while the frequency of ω_1 is the longitudinal optic mode at the zone centre. The region between ω_0 and ω_1 is known as the Restrahlen region.

CHAPTER 5

Optical constant data on various solids

5.1 Introduction

The amplitude r and the phase ϕ of the complex reflectivity have been measured for 10 materials, of which 8 have a zinc blende crystal structure. Many crystals with this structure have been very closely studied in the past, and the selection rules for infrared active processes are well documented. For the other two materials, which are alkaline earth flourides, comparatively little work has been published.

In zinc blende structure crystals, there are two atoms per unit cell, giving three acoustic and three optic branches. At the zone centre, where the wavevector K = 0, the two transverse optic modes TO(Γ) are degenerate. It has been shown by Poulet (1955) that in this crystal structure the lattice bonding is particularly ionic, which will give rise to a macroscopic electric field associated with the longitudinal mode LO(Γ). This has the effect of increasing the force constant of the mode, and so increasing its frequency above that of the TO(Γ). This can be observed in first order Raman scattering, which produces two main peaks, the higher frequency one being the LO(Γ), while the lower one is the TO(Γ). Subsidiary features arise from two and three phonon processes, like summation, difference and overtone combinations. Since the wavevectors of these

phonons are usually much greater than that of the incident photon, then to conserve momentum the two phonons must have equal and opposite wavevectors. This means that the two phonons should arise from the same symmetry point in the Brillouin zone. These combinations of phonons should give peaks in the two phonon density of states. These give rise to features in the anharmonic self energy function Γ, which can be experimentally determined using the equations in chapter 4. Not all combinations of two phonons are allowed by the selection rules, which are given below

(1) All summation and difference combinations of two different phonons at either the X point or L point.

(2) All summation and difference combinations of two different phonons at either the Σ point or W point.

(3) Summation and difference combinations of TO and LO at Γ.

(4) Overtones of TO, LO, TA and LA at L, TO and TA at X, TO and LO at Γ and all phonons at the Σ point are allowed.

Forbidden combinations are overtones of LO and LA at X, and all overtones at the W point.

These selection rules can be found in the paper of Birman (1963), which gives the infrared and Raman activities of two and three phonon combination processes for diamond and zinc blende structure crystals. The frequencies of phonons throughout the Brillouin zone were obtained theoretically from an eleven parameter rigid ion

model (RIM), by Patel (1982). These have been compared to frequencies obtained by neutron scattering data, Raman scattering, I.R absorption data and in the case of InAs, by X-ray scattering. Although phonon combinations are not observed in neutron scattering studies, values obtained for the critical points have been used to calculate the frequencies of some of the combinations. Also from the measured data of r and ϕ, the dielectric functions ϵ' and ϵ'' give the values of the zone centre frequencies. When the function $\epsilon' = 0$, the frequency of LO(Γ) can be determined, and at the peak of ϵ'' the frequency of TO(Γ) can also be determined.

To determine the value of the self energy function Γ from the dielectric functions, equations (4.27) and (4.29) require values of the static, ϵ_0, and high frequency limiting value, ϵ_∞, of the real part of the dielectric function, as well as the value for TO(Γ). For this work, the values taken from the papers by Kunc et al (1975) have been used.

The experimental configuration used to measure the spectra for the various materials is given in table (5.1), along with an explanation of the parameters used. The values plotted for the amplitude must, of course, physically lie between 0 and 1, with the value of the amplitude reflectivity of 1 being equivalent to a perfect mirror. Because of the accurate alignment by use of laser fringe monitoring, the reflectivity is accurate to better than 1% over most of the measured range, requiring no external scaling. Also the uncertainty in the phase is less

than about 0.5° over most of the measured range. The experimentally measured phase ϕ is the difference between the phase response of the sample ϕ_S and the phase response of a perfect mirror π, i.e $\phi = \phi_S - \pi$, and is the function plotted in all the figures. The refractive and absorption indices, n and k, have been calculated from the amplitude r and the phase $\phi_S = \phi + \pi$, as have the dielectric responses ϵ' and ϵ''. The function Γ has been plotted linearly for most materials, but for some i.e InAs, to expand any features the logarithmic value of Γ has been plotted.

Figure (5.1) shows the interferogram obtained using a Diamond Golay detector with two identical mirrors in the arms, while figure (5.2) shows the interferogram when one of the mirrors has been replaced with a polished sample of InAs. The ADC has a resolution of 12 bits, giving 4096 elements each of 2.5 mV. As can be seen in the wings of the interferogram, subsidiary interferograms (signatures) are present. These are due to multiple interference effects caused by the Golay cell window. Figure (5.3) shows an expanded view of these signatures, and as can be observed the sample signatures are dispersive. This limits the resolution obtainable with this detector as the interference signatures do not ratio out between the reference and sample interferograms. The CsI Golay has a thick window, and so the signatures are far out in the wings of the interferogram and do not appear in this data. The Quartz Golay has been modified by using a wedged window to eliminate signatures.

The filtering used was black polyethylene, which along

with the scan speed filtering was sufficient to cut off any high wavenumber components. This is required so that no spurious effects occur due to aliasing. Mylar was used as the beam splitter material as the interferometer was not operating in the polarising mode, with different thicknesses used to suit the spectral range. It has been found that a scan speed of around 400 Hz gives the best signal to noise ratio when operating with a peak spectral response of around 250 cm^{-1}. The speed was reduced when the higher wavenumber regions were needed for the alkaline earth flourides.

TABLE 5.1

Experimental parameters for the

I.R reflection data

Material	InAs	InSb	InP	GaAs	GaSb	GaP	ZnSe	CdTe	CaF_2	BaF_2
Detector see note 1	Dia	Dia	CsI	Dia	Dia	Dia	Dia	Quartz	CsI	Dia
filtering see note 2	2.3_1	1.5_2	2.3_1	1.0_2	2.3_1	2.3_1	2.3_1	2.3_1	1.3_2	1.5_2
Beam splitter see note 3	6.25	6.25	6.25	6.25	6.25	6.25	6.25	12.5	3	3
Scan speed see note 4	400	400	400	400	400	400	400	400	200	200
Resolution (cm^{-1})	4	4	2	4	4	4	4	2	2	4
Spectral range see notes 5	40 - 440	40 - 440	200 - 450	40 - 440	40 - 440	40 - 440	40 - 440	20 - 240	200 - 650	50 - 650

Notes for TABLE 5.1

NOTE 1

Three different window materials were used in the Golay detectors, which define the spectral range.

Dia — Diamond, which has a flat response across the whole of the far infrared.

CsI — Caesium Iodide, which has a Reststrahlen region and does not transmit below 150 cm^{-1}.

Quartz — which does not transmit above 250 cm^{-1}.

NOTE 2

The filtering used is black polyethylene, which comes in two densities, labelled with the subscripts 1 and 2. The polyethylene labelled 1 is of a lower density than that labelled 2, so the thickness required to block the higher wavenumber region is greater.

NOTE 3

The table gives the thickness of the Mylar in micrometers (μm).

NOTE 4

The figures give the scan speed in terms of the laser fringe frequency, instead of displacement per second, since the laser fringe is directly measured. These two parameters are related by equations (3.2) and (3.3).

NOTE 5

The values give the range over which the spectral response is reproducible to a few percent.

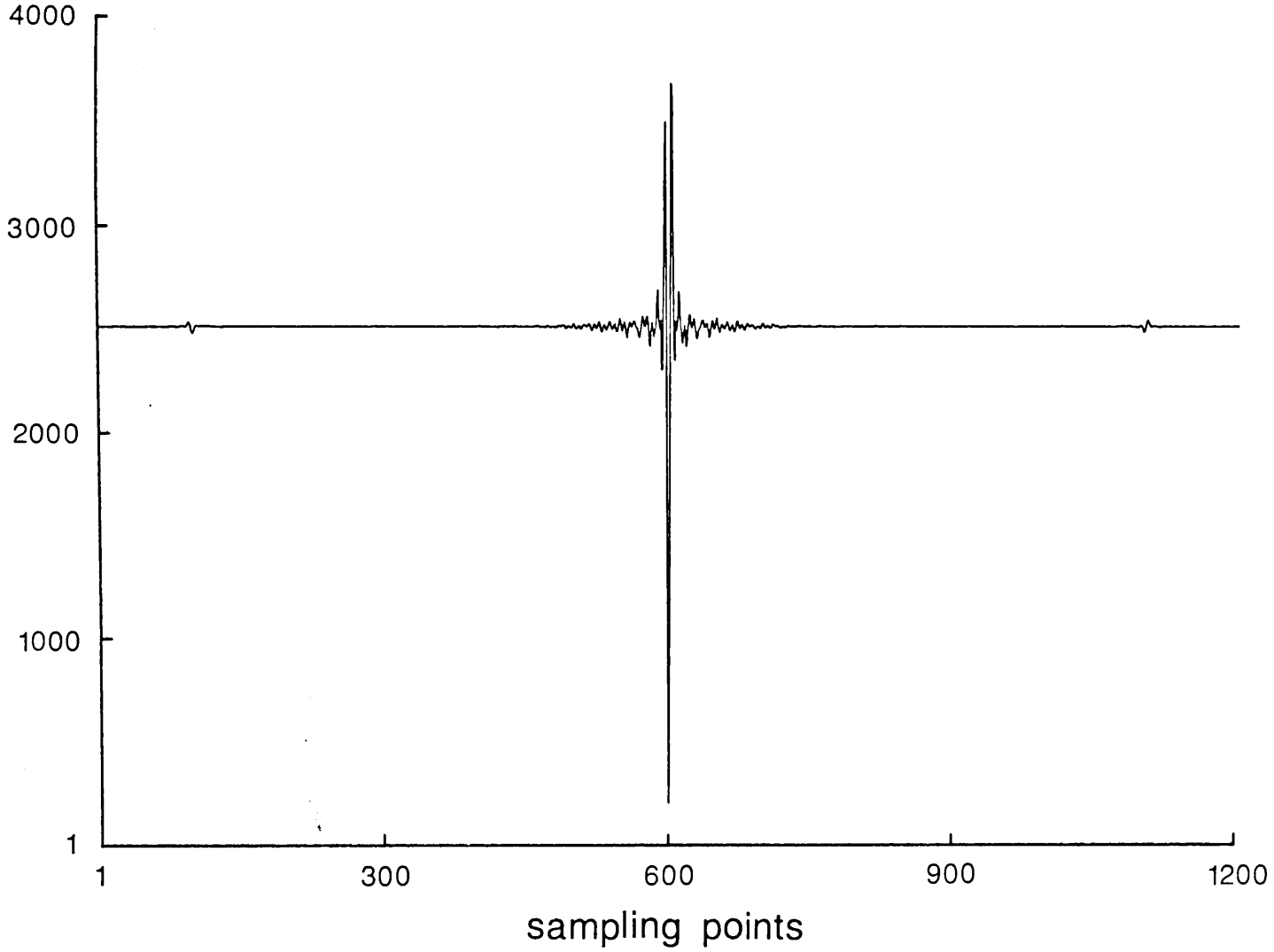

Figure 5.1 Reference interferogram obtained with two identical mirrors

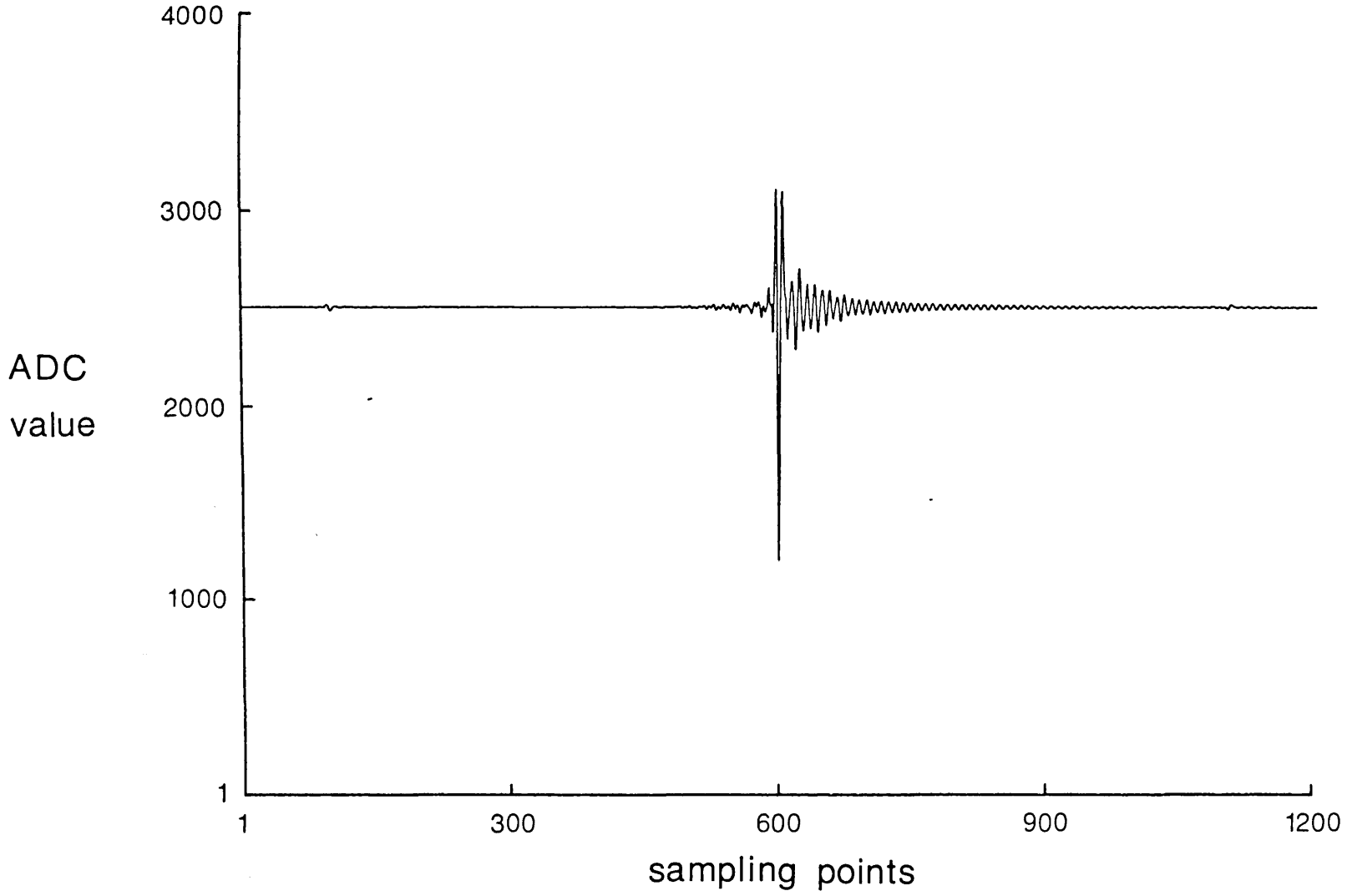

Figures 5.2 Sample interferogram obtained with one of the mirrors replaced with InAs

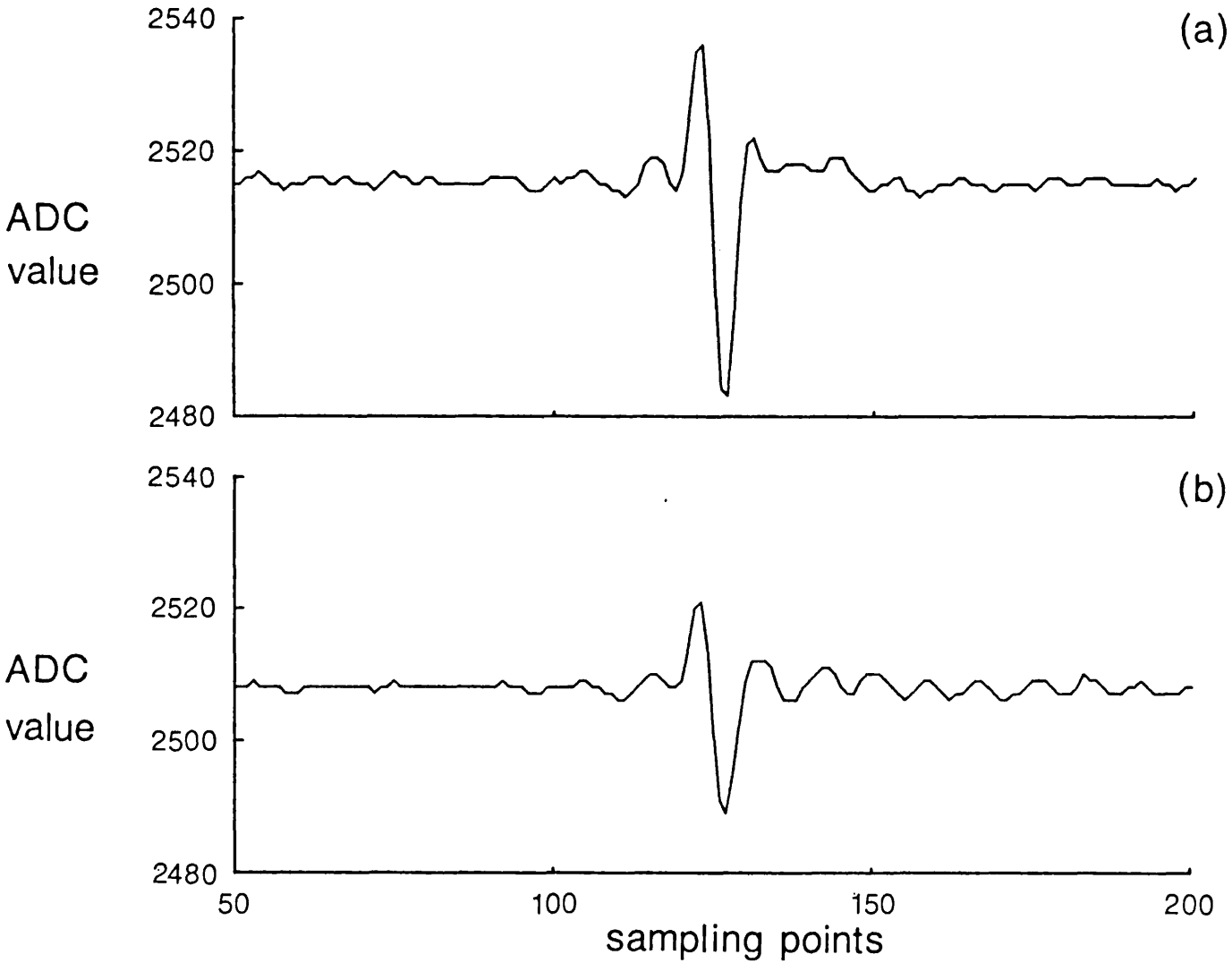

Figure 5.3 Signatures on the reference (a) and sample (b) interferograms

5.2 Optical constant data of InAs

The amplitude r and the phase ϕ of the complex reflectivity of InAs at room temperature are shown in figure (5.4). Free carrier effects can be seen in the low wavenumber region. From this data have been calculated the refractive index n and absorption index k, figure (5.5), using equation (2.36). Also the real part ϵ' and imaginary part ϵ'' of the dielectric function, figure (5.6), can be obtained using equations (2.40) and (2.41). Also shown in figure (5.7) is an enlarged plot of the dielectric function ϵ' showing how the values of LO(Γ) can be determined when $\epsilon' = 0$. Also shown on this diagram is the function 1/(modulus ϵ') which clarifies the determination of LO(Γ). Figure (5.8) shows the enlarged plot of the dielectric function ϵ'' which determines the value of TO(Γ). This also shows that to first order the Reststrahlen response appears like a classically damped oscillator centred at TO(Γ). Figure (5.9) is a logarithmic plot of the anharmonic self energy function Γ, as given by equation (4.29). The features arrowed are the ones that are reproducible within the limits of the experimental uncertainty. The frequencies of these features are compared in table (5.2) to assignments from the rigid ion model of Patel (1982), Raman work of Carles et al (1980) and X-ray data from Orlova (1979). This material absorbs neutrons very heavily, and phonon frequencies at only a couple of critical points are known with any certainty.

The values obtained for the zone centre frequencies

TO(Γ) and LO(Γ) compare quite well with the results of the RIM model and the Raman results. No two-phonon processes could account for any features between 229 and 255 cm^{-1}, so these had to be assigned by three phonon effects. Not all the three-phonon processes have been calculated due to the number involved, about 600, but each of the observed features does have at least one three-phonon assignments to within the errors of the reported critical point phonons.

Also in the low wavenumber region, free carrier absorption can be seen, with the amplitude minimum at 71 cm^{-1}. Using equations (4.33) and (4.34) for the free carrier concentration, and an effective mass of 0.026 m_e, gives a carrier concentration of 1.5 x 10^{15} cm^{-3}.

TABLE 5.2

InAs assignments

OBSERVED FREQUENCY	RAMAN 330 K Ref 1	X-RAY Ref 2	RIM (11) Ref 3	ASSIGNMENTS
213	213.0	203	212.7	LA(X) + TA(X)
218.5	217.3	_	220.7	TO(Γ)
223	_	_	226.7	$IIA\Sigma_1$ + $IA\Sigma_1$
235	_	239	232.0	TO(L) + TA(X) - TA(L)
239	_	_	241.3	2TO(X) - TO(Γ)
242.5	238.6	_	242.9	LO(Γ)
256	252.0	256	256.5	LO(X) + TA(X)
270	260.0	_	267.8	TO(L) + TA(L)

Ref 1 Carles R et al; 1980.

Ref 2 Orlova N.S; 1979.

Ref 3 Patel C; 1982.

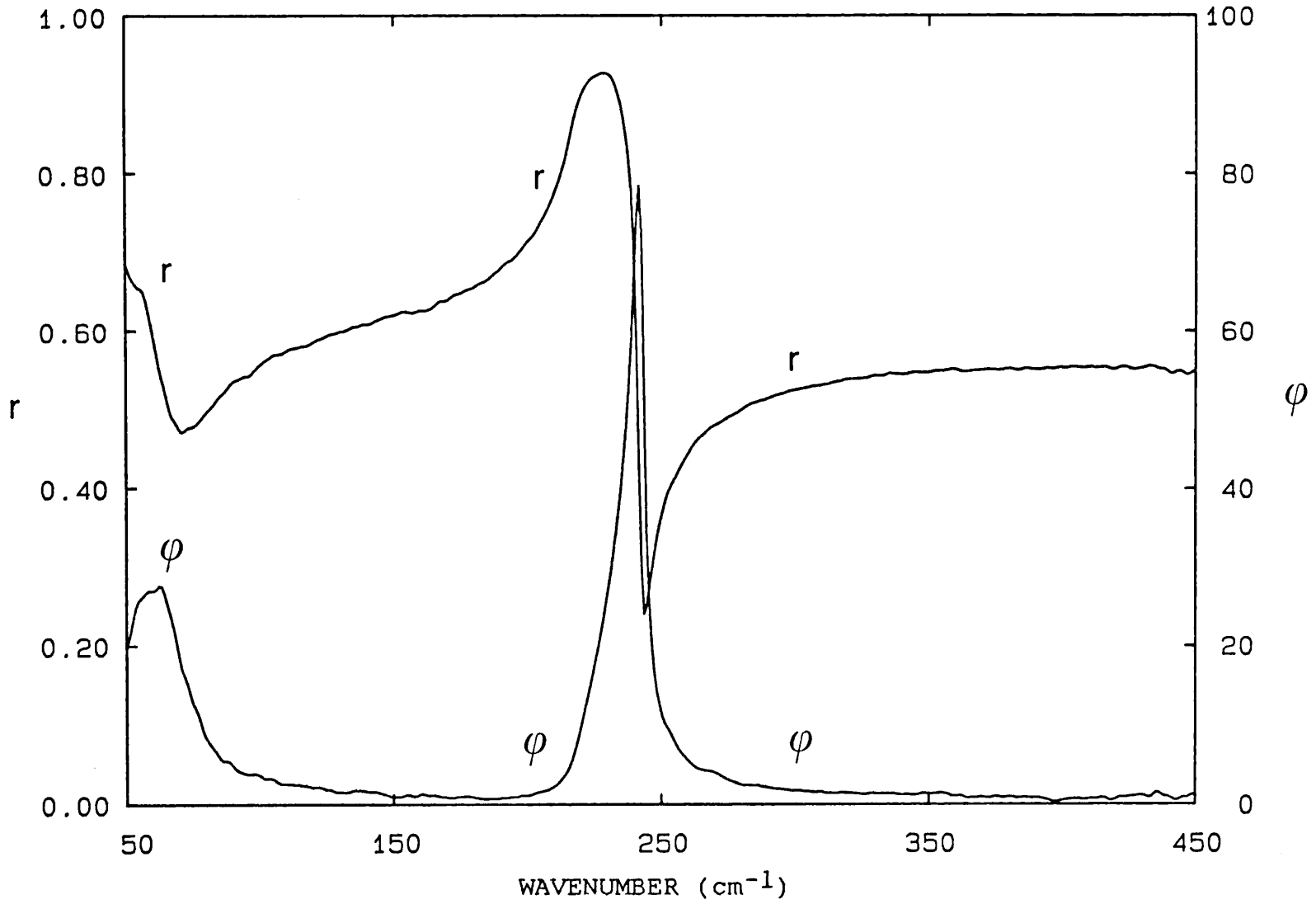

Figure 5.4 Complex reflectivity amplitude r and phase ϕ of InAs at 300K

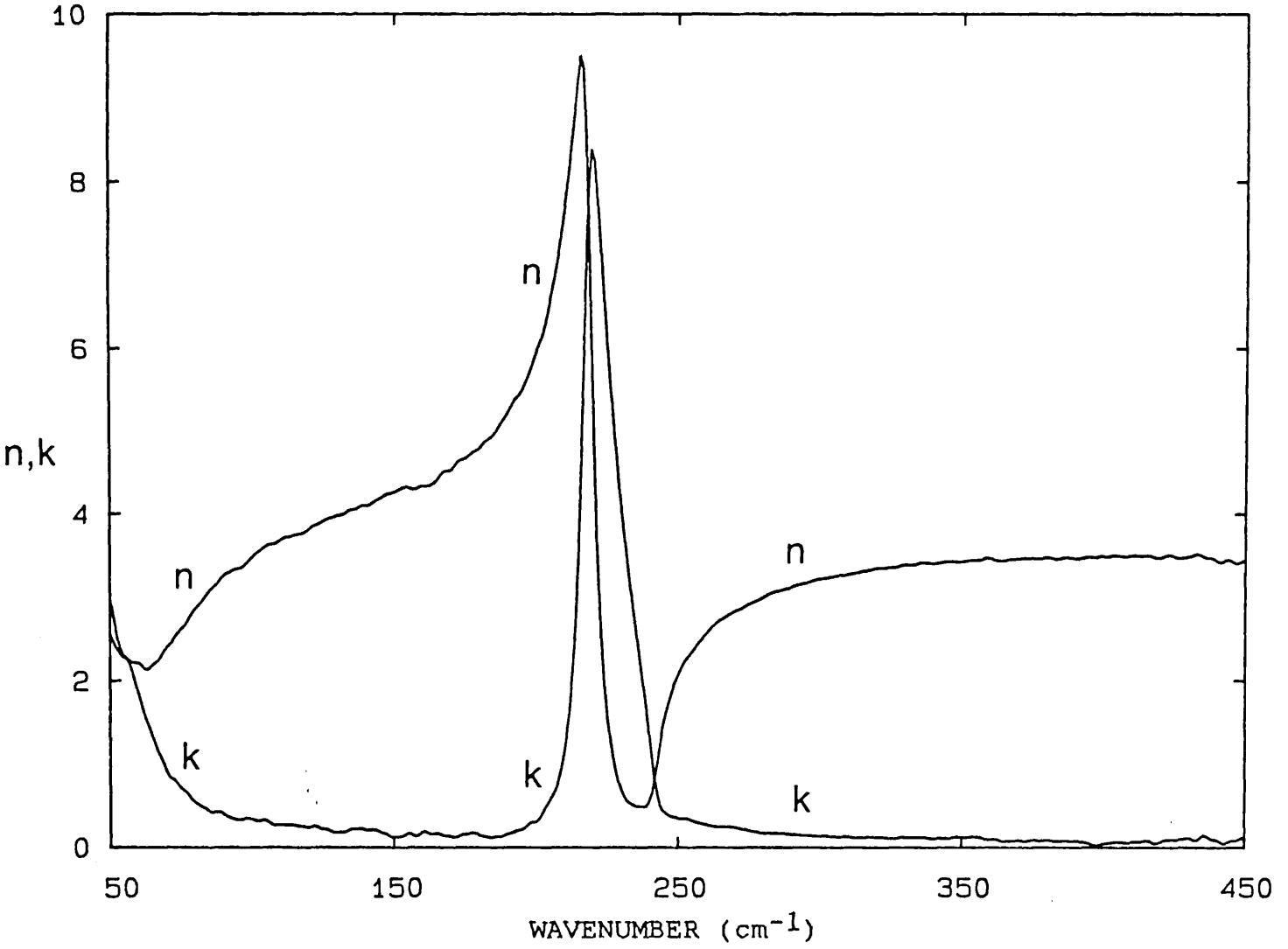

Figure 5.5 Refractive index n and absorption index k for InAs at 300K

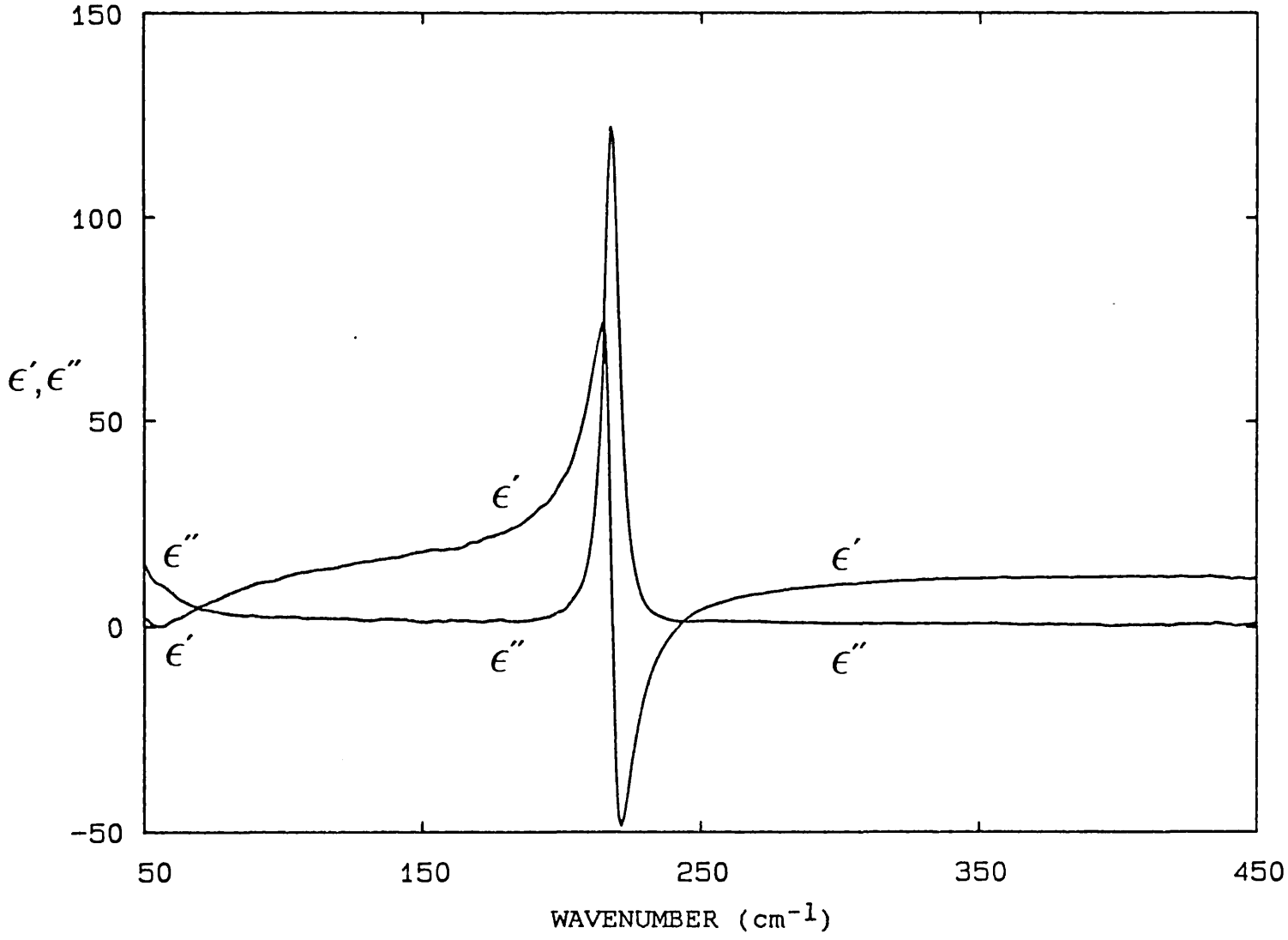

Figure 5.6 Real ϵ' and imaginary ϵ" parts of the dielectric response for InAs at 300K

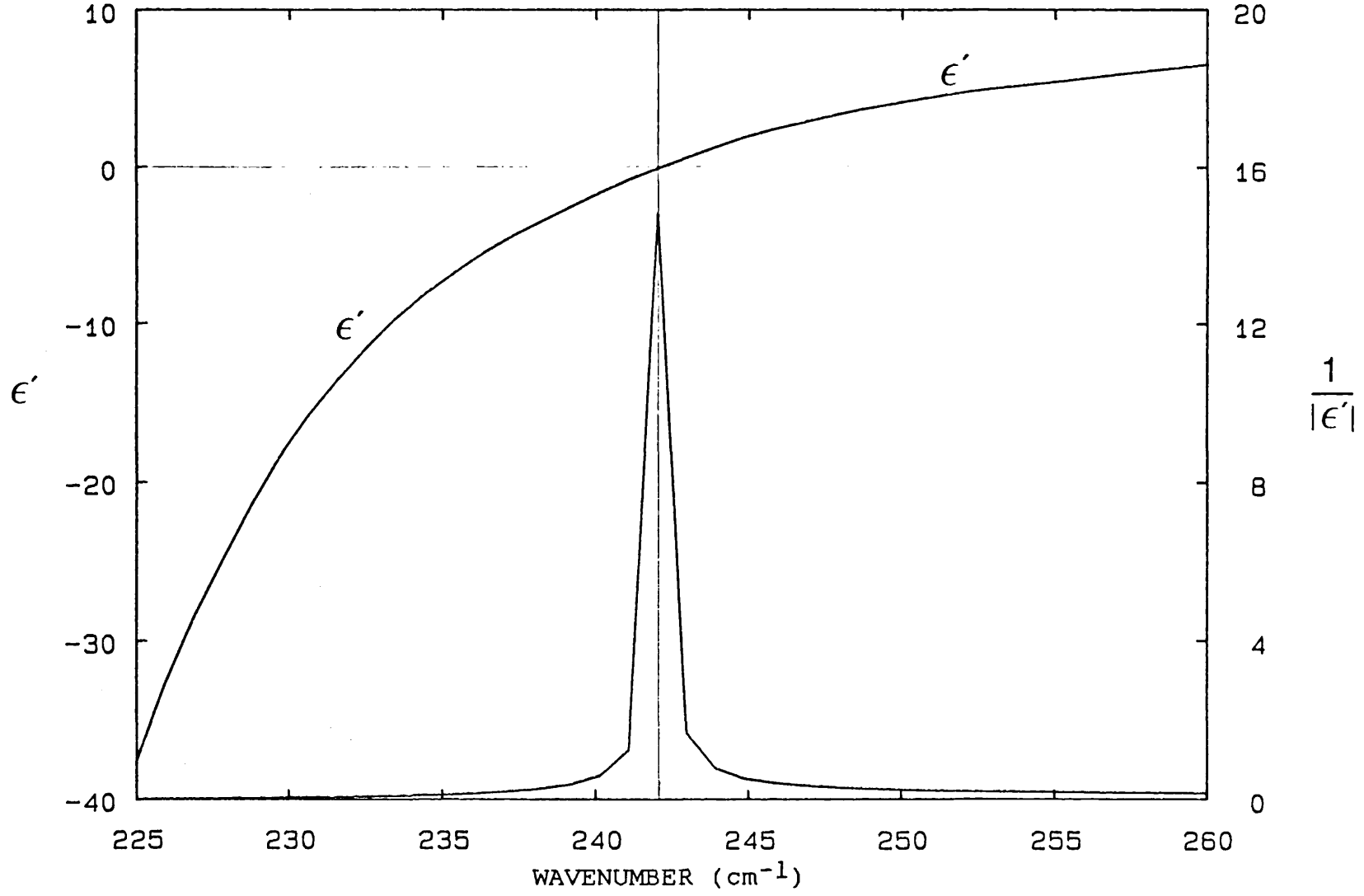

Figure 5.7 Expanded plot of ϵ' and 1/mod ϵ' for InAs at 300K

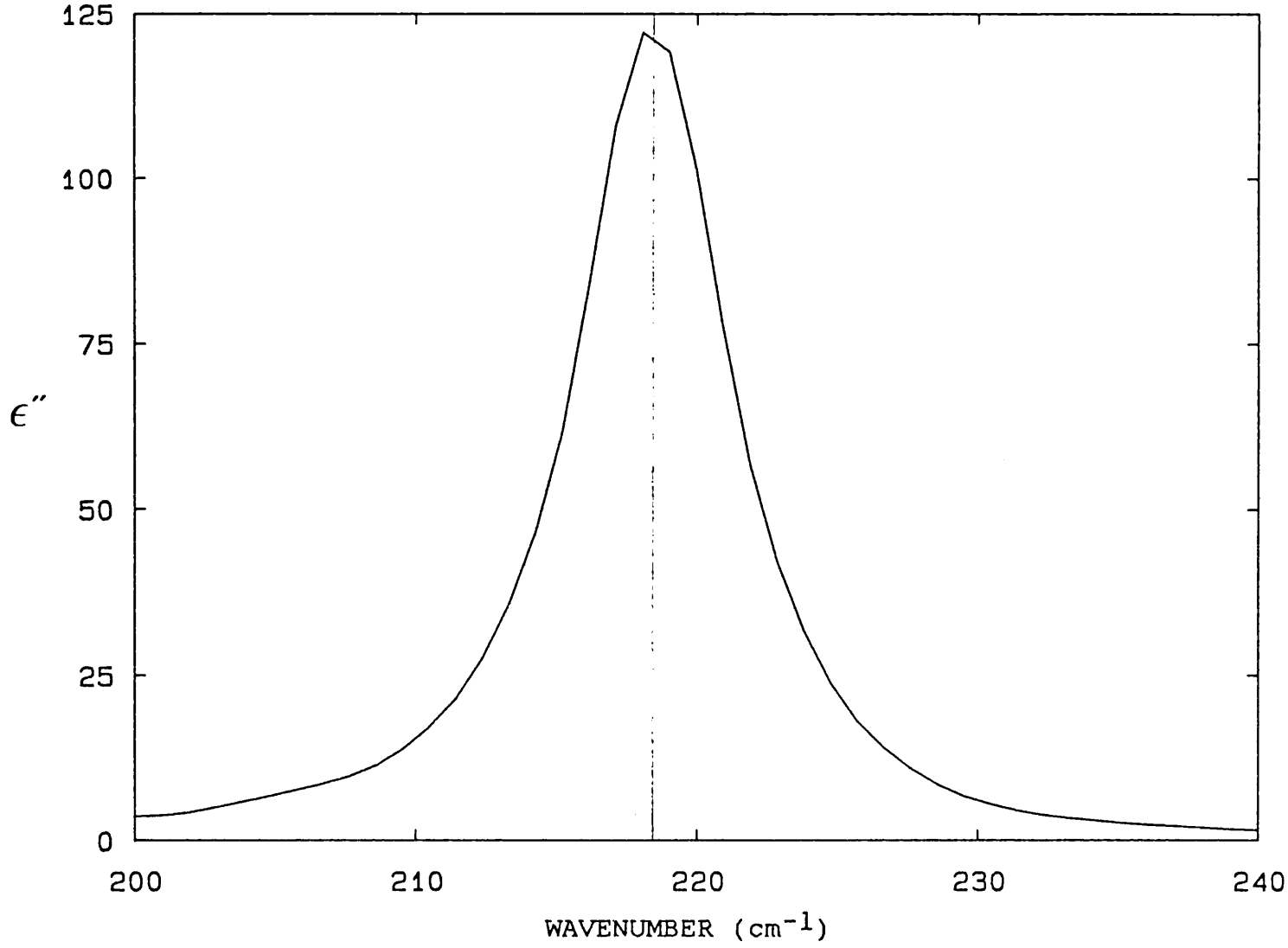

Figure 5.8 Expanded plot of ϵ" for InAs at 300K

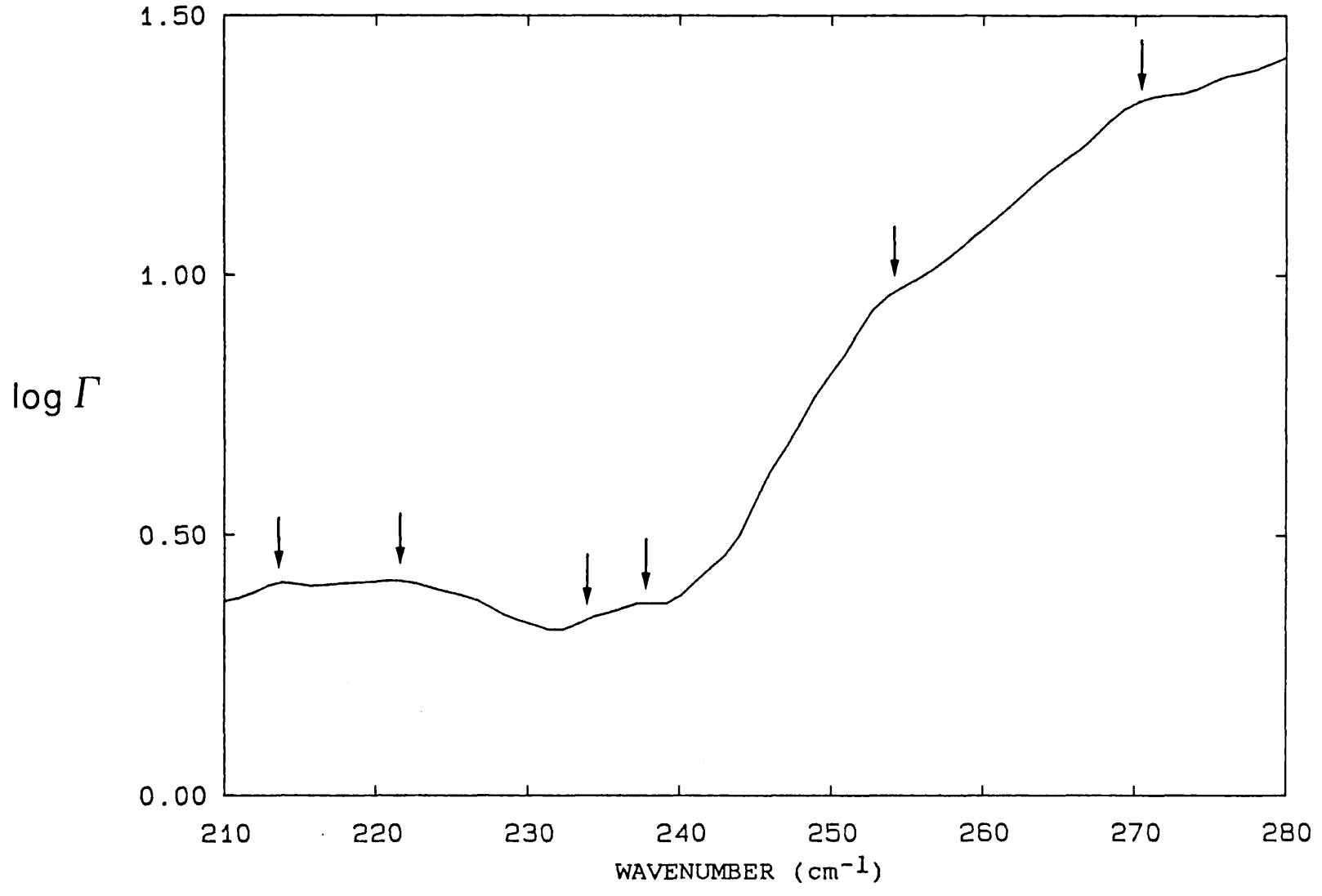

Figure 5.9 Log plot of the anharmonic self energy function Γ for InAs at 300K

5.3 Optical constant data of InSb

Figure (5.10) shows the amplitude r and phase ϕ of the complex reflectivity of InSb at room temperature. Also shown in figure (5.11) are the calculated refractive index n and absorption index k, and in figure (5.12) the real and imaginary parts of the dielectric response. From this data has been calculated the self energy function Γ, as shown in figure (5.13). This shows one major feature at 146 cm^{-1} and a couple of small features, as given in table (5.3). From the dielectric functions, the zone centre frequencies were obtained, and along with the features observed in Γ, compared in table (5.3) with the results of the RIM model by Patel (1982), neutron data by Price et al (1977), I.R absorption work by Koteles et al (1976) and Raman scattering by Kiefer et al (1975).

As can be seen in this table, the observed zone centre frequencies agree quite closely, while the RIM model gives slightly lower values. Since the neutron data has an uncertainty of at least a few wavenumbers, the values are within the experimental errors of the neutron data. The major feature at 146 cm^{-1}, as well as the 199 and 211 cm^{-1} features, have been seen in I.R absorption studies. These all agree quite well with both the RIM model and the neutron data.

Free carrier effects are seen at lower wavenumbers, with the reflection minimum at 75 cm^{-1}. Using this with equation (4.33) and (4.34), with an effective mass of 0.015 m_e, gives a carrier concentration of 9.4×10^{14} cm^{-3}.

TABLE 5.3

InSb assignments

OBSERVED FREQUENCY	NEUTRON Ref 1	I.R ABSORPTION 15 K Ref 2	RAMAN 77 K Ref 3	RIM (11) Ref 4	ASSIGNMENTS
145	144.4	146	_	144.3	TO(L) - TA(L)
181	185.0	_	182.4	179.2	TO(Γ)
193	197.0	_	193.0	190.5	LO(Γ)
195	193.5	_	_	193.5	LO(L) + TA(L)
199	195.8	199	_	193.2	LO(X) + TA(X)
211	209.8	208	_	209.2	TO(L) + TA(L)

Ref 1 Price D.L et al; 1977.

Ref 2 Koteles E.S and Datars W.R; 1976.

Ref 3 Kiefers W et al; 1975.

Ref 4 Patel C; 1982.

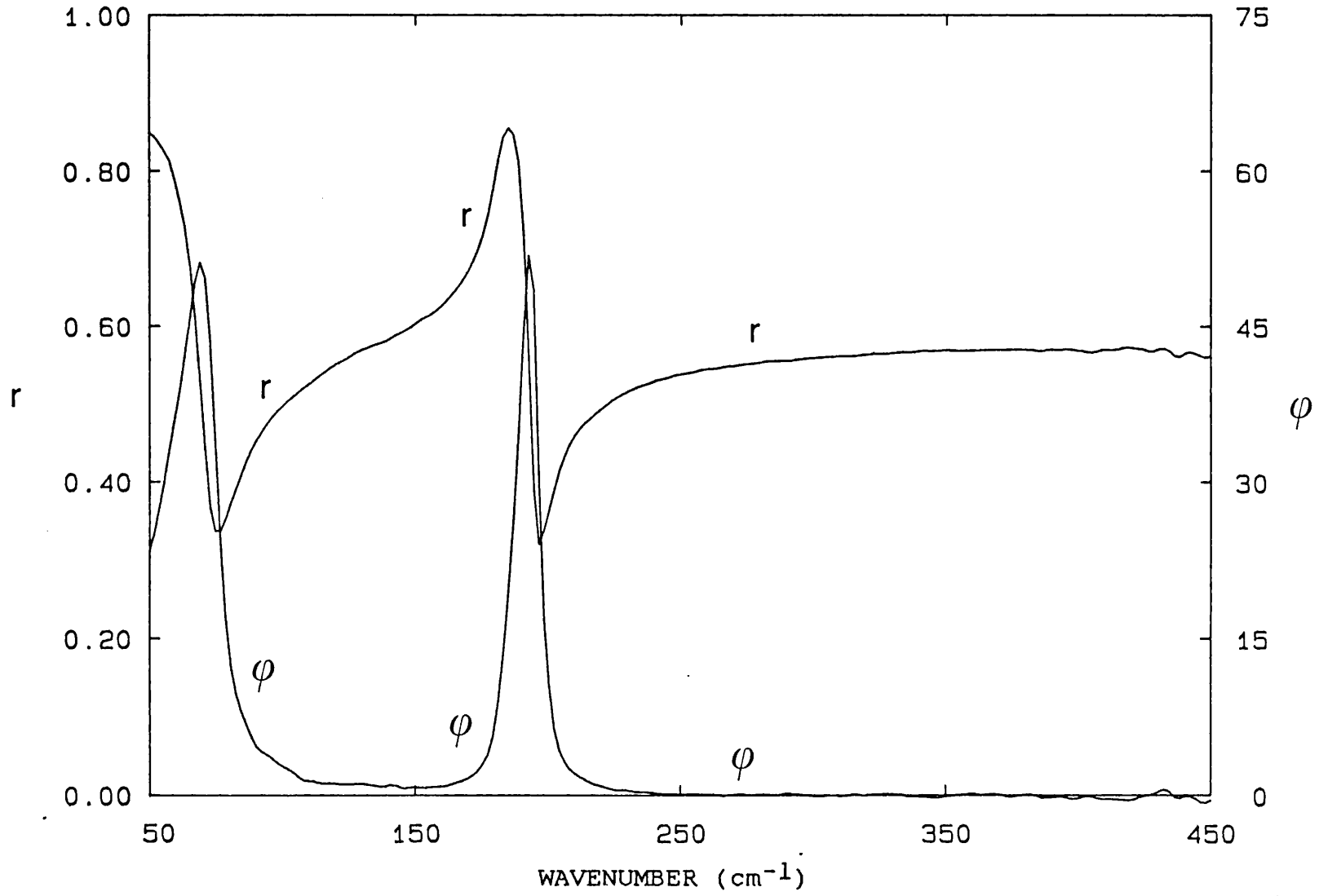

Figure 5.10 Complex reflectivity amplitude r and phase ϕ of InSb at 300K

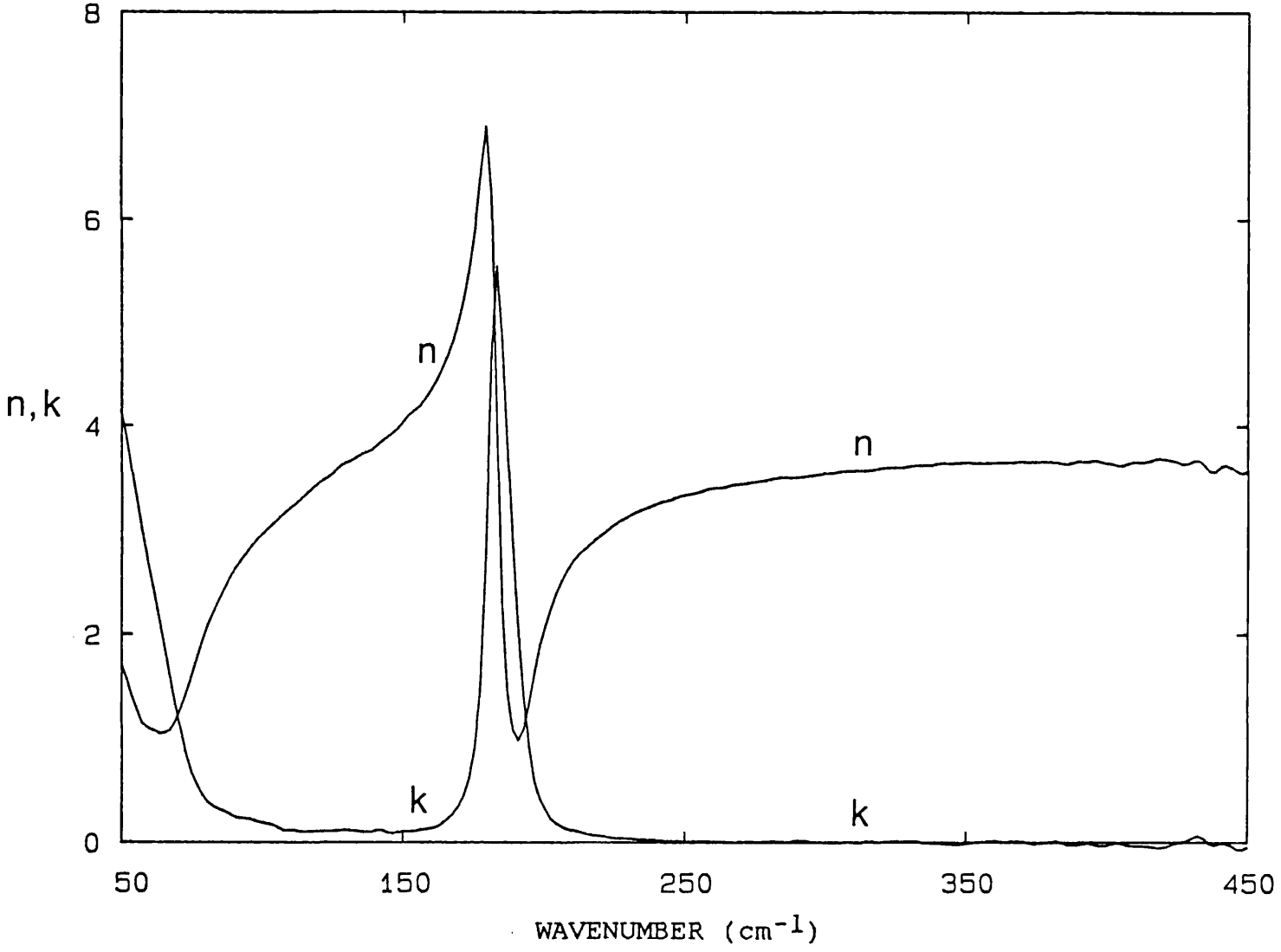

Figure 5.11 Refractive index n and absorption index k for InSb at 300K

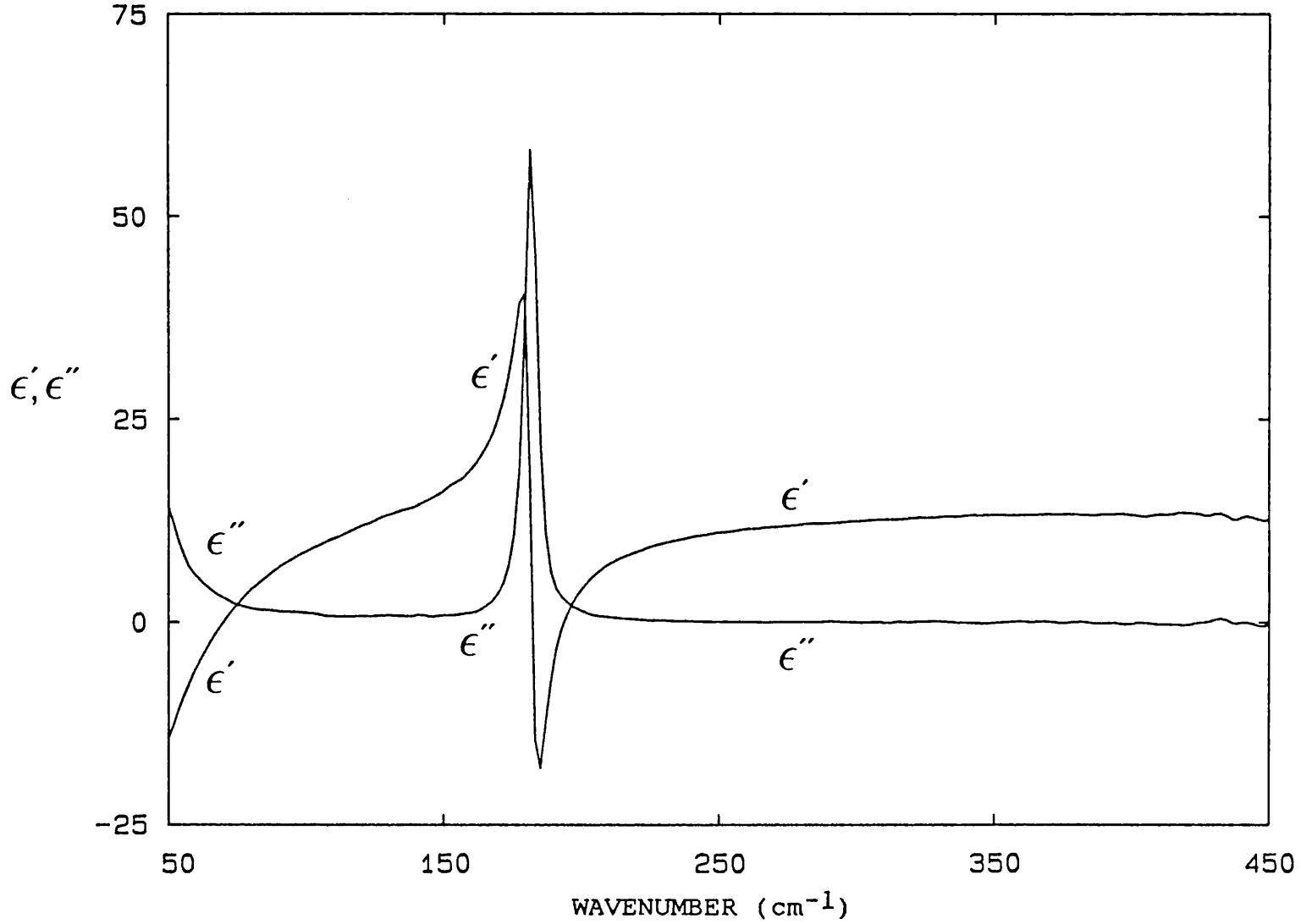

Figure 5.12 Real ϵ' and imaginary ϵ" parts of the dielectric response for InSb at 300K

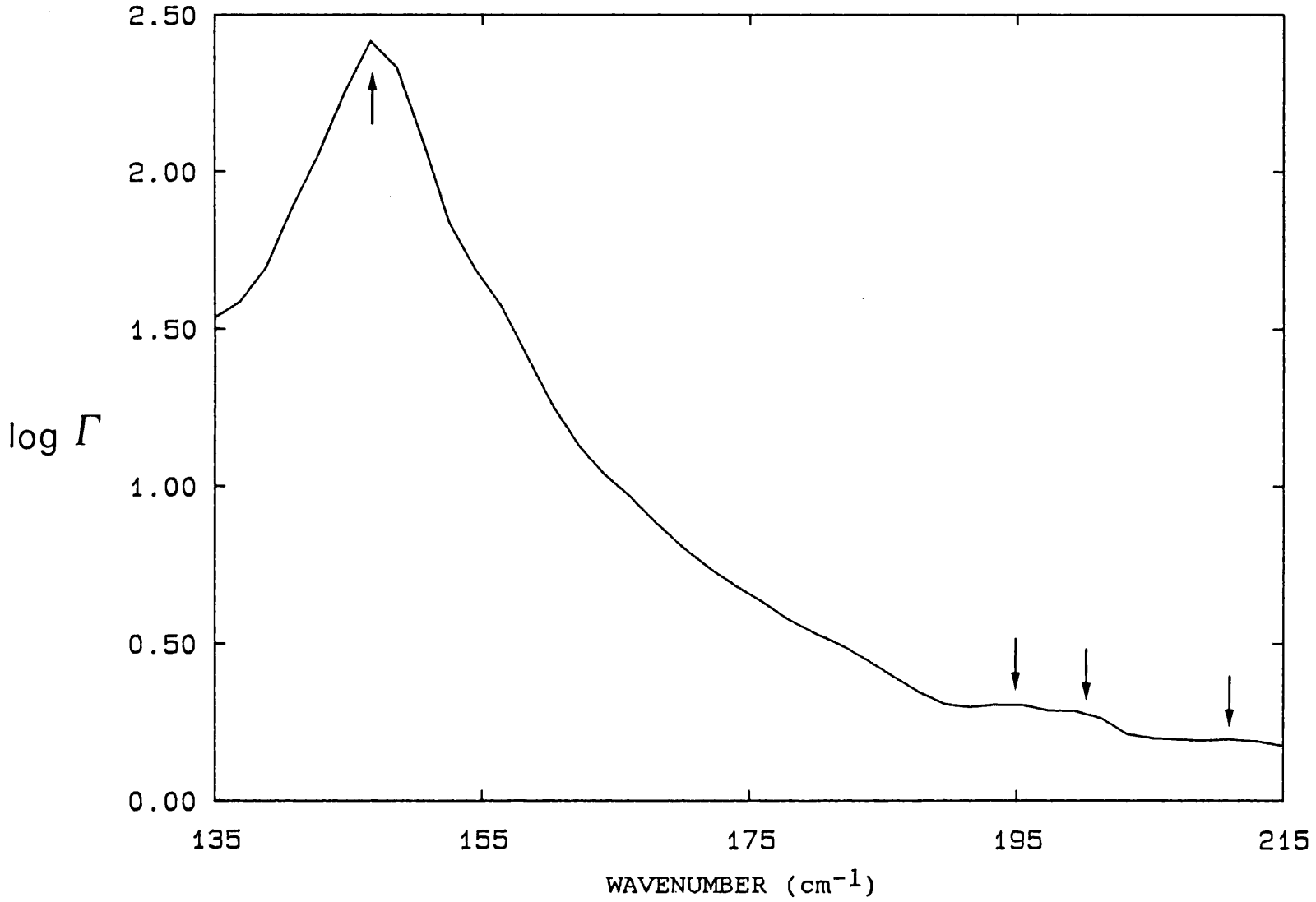

Figure 5.13 Log plot of the anharmonic self energy function Γ for InSb at 300K

5.4 Optical constant data of InP

The amplitude r and phase ϕ of the complex reflectivity of InP are shown in figure (5.14), and the calculated values of n and k are shown in figure (5.15), and ϵ' and ϵ'' in figure (5.16). From these functions has been calculated Γ, figure (5.17), which shows four reproducible features. The two zone centre frequencies from the dielectric functions, as well as the features seen in Γ are presented in table (5.4). These results are compared with the results of the RIM model of Patel (1982), neutron studies by Borcherds et al (1975), I.R absorption measurements at 77 K by Vandevyver et al (1977) and Raman work of Alfrey et al (1972). The values of the critical point frequencies at LA(X), TO(L) and LA(L) determined by neutron scattering have very large error bars in the literature. The values of TO(Γ) and LO(Γ) obtained from the dielectric functions agree very closely with the results of the Raman work, as well as with the values from the RIM model. No two-phonon combinations could account for the features at 309, 347 and 358 cm^{-1}, so these have been assigned to three-phonon processes. The observed band at 347 cm^{-1} agrees with the Raman work, in which it was assigned to a combination of three phonons in the Σ direction. The feature at 377 cm^{-1} has been seen in I.R absorption studies, although the agreement with the model is not very good. No free carrier response was seen down to 30 cm^{-1} in this sample, giving a maximum carrier concentration of 7.4×10^{14} cm^{-3} using an effective mass of 0.073 m_e.

TABLE 5.4

InP assignments

OBSERVED FREQUENCY	NEUTRON Ref 1	I.R ABSORPTION 77 K Ref 2	RAMAN Ref 3	RIM (11) Ref 4	ASSIGNMENT
304	306.9	–	304.5	305.2	$TO(\Gamma)$
309	–	–	–	311.8	$TO(\Gamma) + W_5 - W_4$
346.5	–	–	346.4	346.7	$LO(\Gamma)$
347	–	–	346.0	347.0	$IIO\Sigma_1 + TO\Sigma_2 - IO\Sigma_1$
358	366	–	–	358.0	$LO(L) - LA(L) + LA(X)$
377	372	373	–	370.2	$TO(L) + TA(L)$

Ref 1 Borcherds P.H et al; 1975.

Ref 2 Vandevyver M and Plumelle P; 1977.

Ref 3 Alfrey G.F and Borcherds P.H; 1972.

Ref 4 Patel C; 1982.

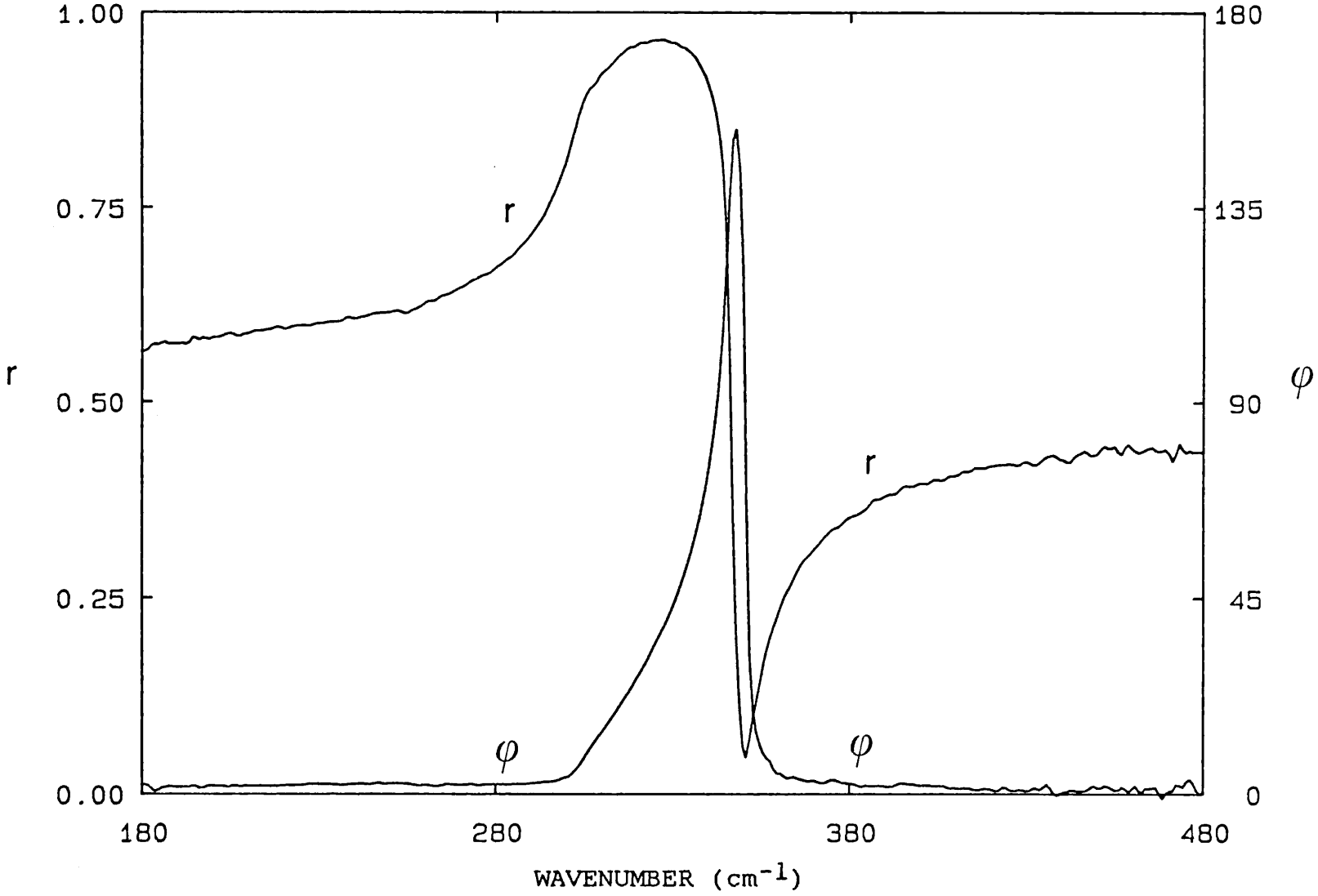

Figure 5.14 Complex reflectivity amplitude r and phase ϕ of InP at 300K

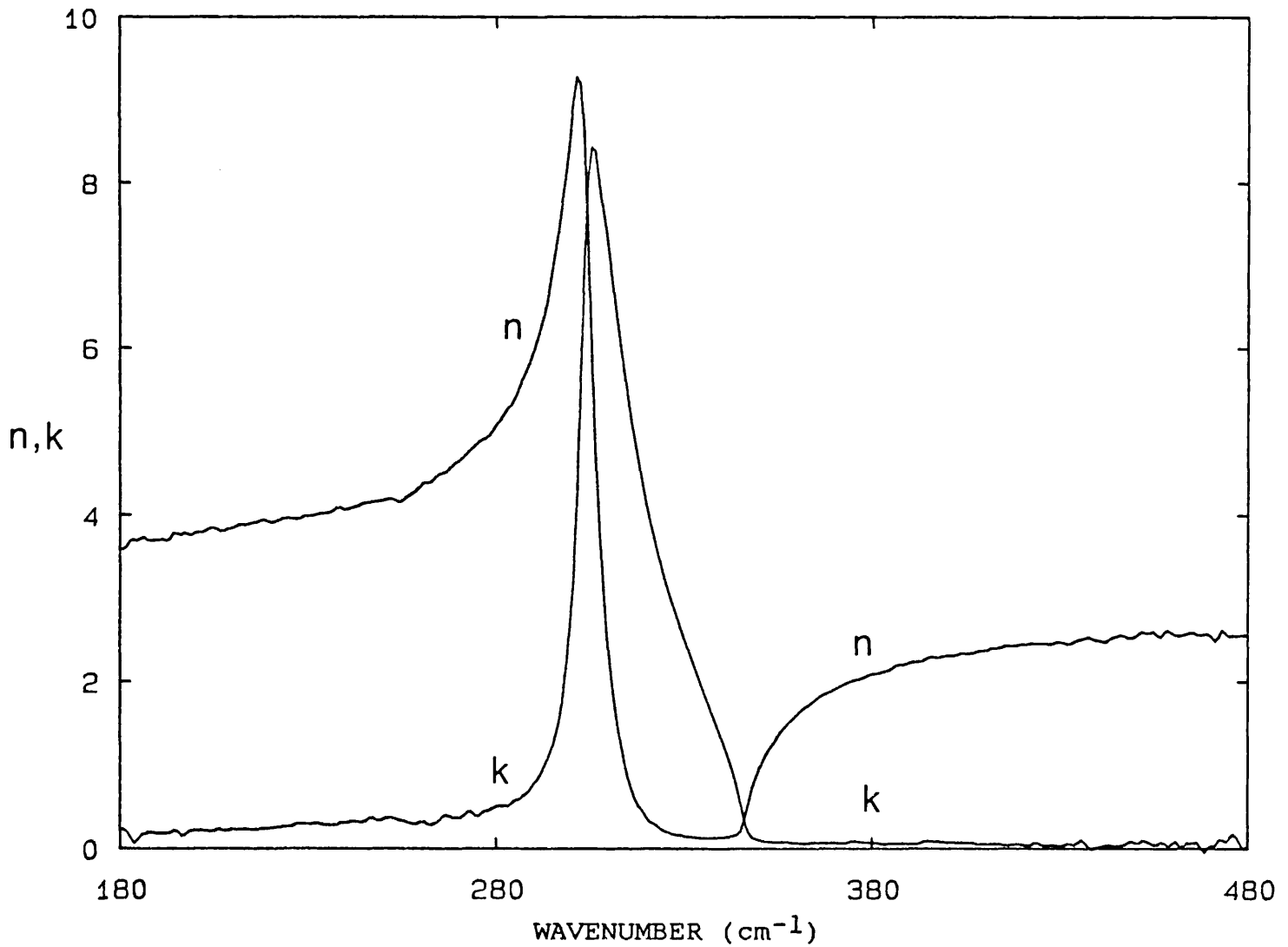

Figure 5.15 Refractive index n and absorption index k for InP at 300K

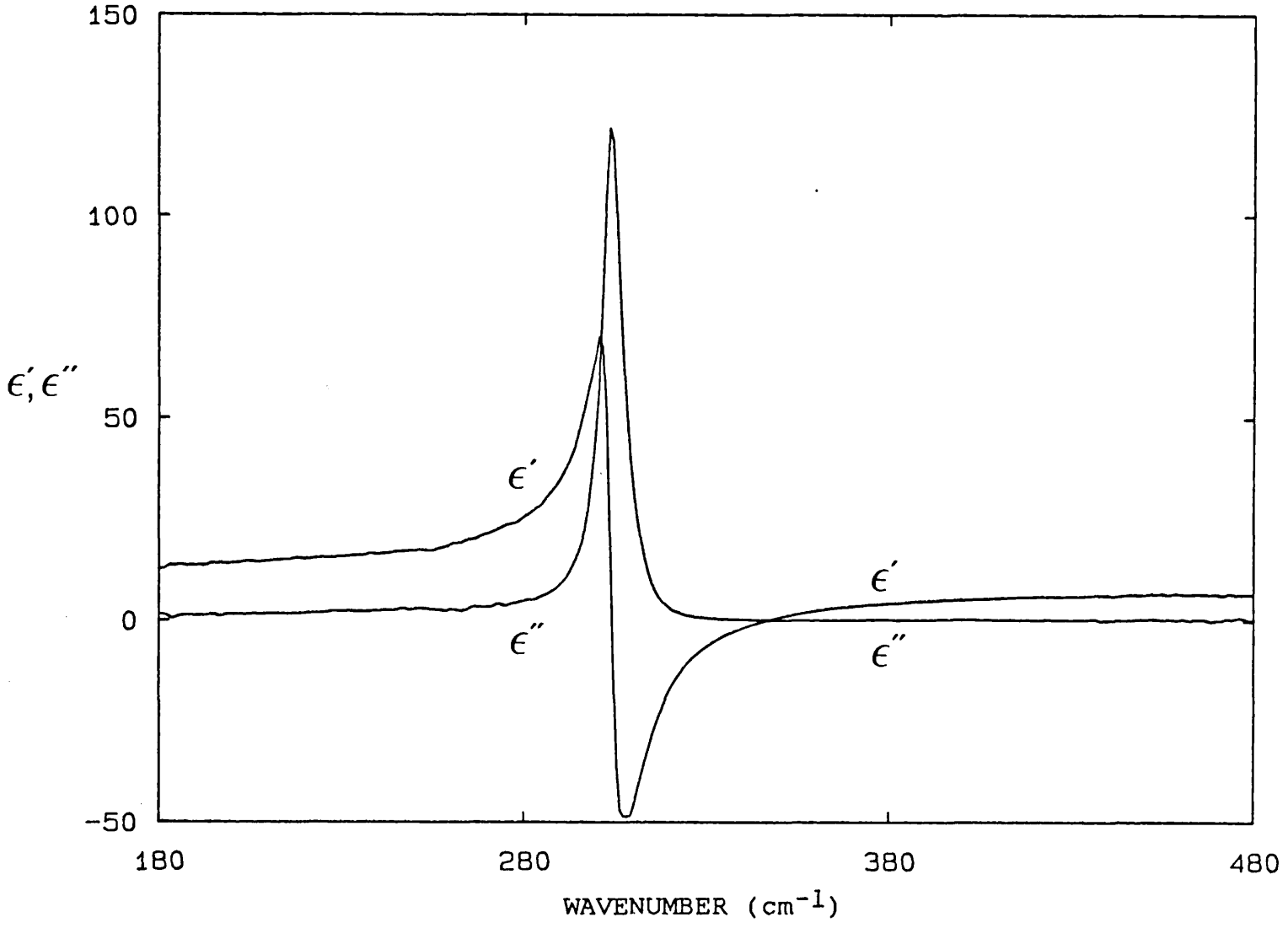

Figure 5.16 Real ε' and imaginary ε" parts of the dielectric response for InP at 300K

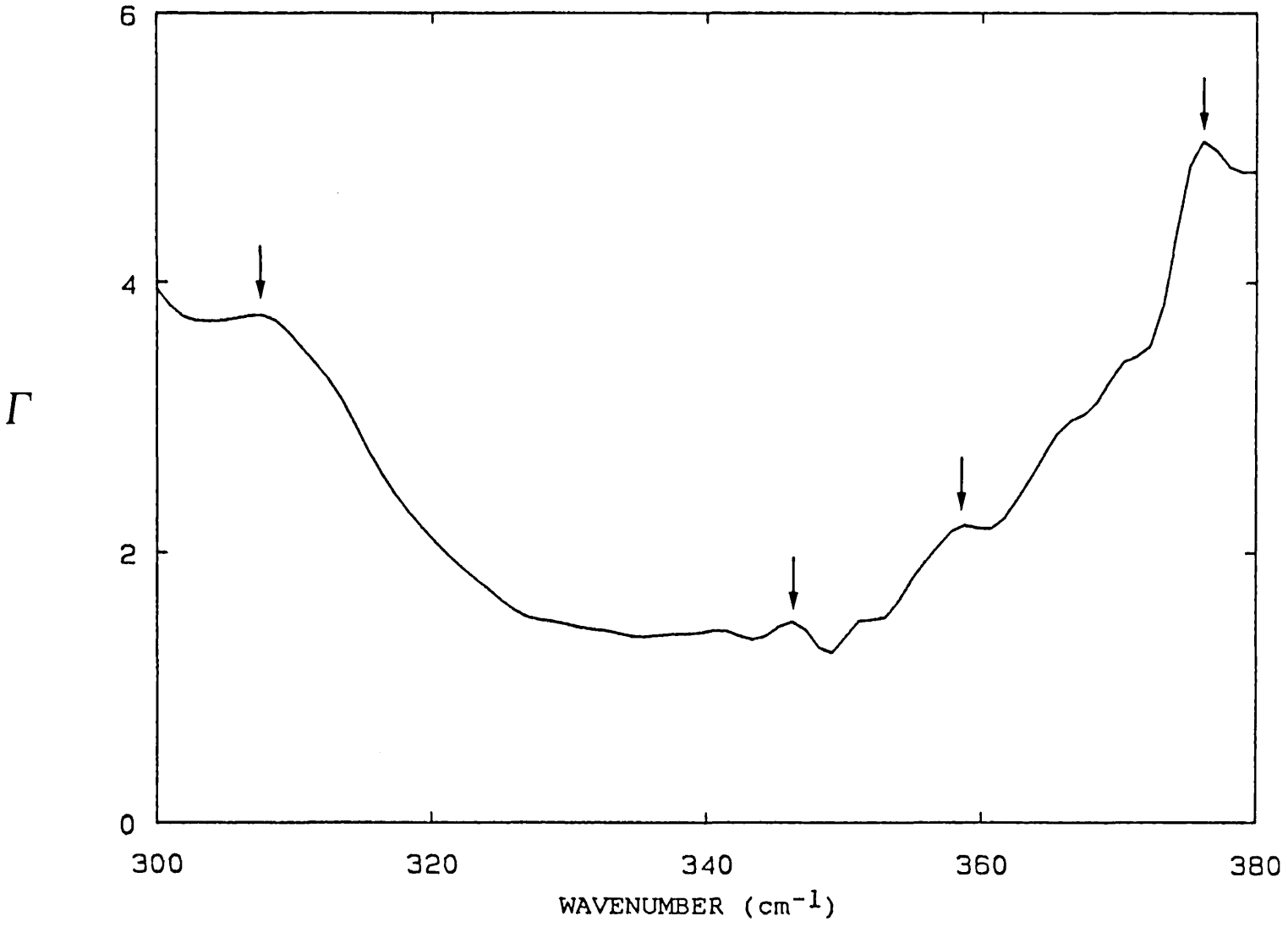

Figure 5.17 Plot of the anharmonic self energy function Γ for InP at 300K

5.5 Optical constant data of GaAs

Figure (5.18) shows the amplitude r and the phase ϕ of the complex reflectivity for GaAs. This data has then been used to calculate the refractive index n and absorption index k, as shown in figure (5.19), as well as the real and imaginary parts of the dielectric response, figure (5.20). From this has been calculated the self energy function Γ, which is shown in figure (5.21). The frequencies of the features observed, plus the frequencies of the two phonons at the zone centre obtained from the dielectric functions, are tabulated in table (5.5). The observed features are compared with results from the RIM model of Patel (1982), neutron data from Dolling and Waugh (1969), I.R absorption work of Koteles et al (1976) and some Raman work of Sekine et al (1977). The two zone centre frequencies agree quite well with the published data, although the reported neutron value for LO(Γ) has error bars of $\pm$ 6.7 cm^{-1}. Due to these large uncertainties, three assignments have been used for the feature at 292 cm^{-1}. This could also be due to a two phonon combination at W according to the RIM model, $W_3 + W_6$ at 289 cm^{-1}, but since these frequencies cannot be verified they have not been listed. Free carrier effects can be seen in the low frequency region, with the minimum of the reflectivity amplitude at 60 cm^{-1}. By using this value as the plasma frequency, with an effective mass of 0.07 m_e, then equation (4.34) gives a free carrier concentration of 2.8×10^{15} cm^{-3}.

TABLE 5.5

GaAs assignments

OBSERVED FREQUENCY	NEUTRON	I.R ABSORPTION	RAMAN	RIM (11)	ASSIGNMENTS
		15 K	295 K		
	Ref 1	Ref 2	Ref 3	Ref 4	
269	267.3	271	269	268.5	TO(Γ)
271	270.7	–	–	268.0	LA(L) + TA(L)
292	296.6	–	–	295.3	$IIO\Sigma_1$ + $TA\Sigma_2$
	300.3	–	–	302.9	LA(X) + TA(X)
	305.4	–	–	302.8	LO(L) + TA(L)
293	285.0	295	291	292.1	LO(Γ)
310	319.4	310	–	312.8	LO(X) + TA(X)
	310.0	–	–	312.7	$IIA\Sigma_1$ + $IA\Sigma_1$

Ref 1 Dolling G and Waugh J.T.L; 1965.

Ref 2 Koteles E.S and Datars W.R; 1976.

Ref 3 Sekine T et al; 1977.

Ref 4 Patel C; 1982.

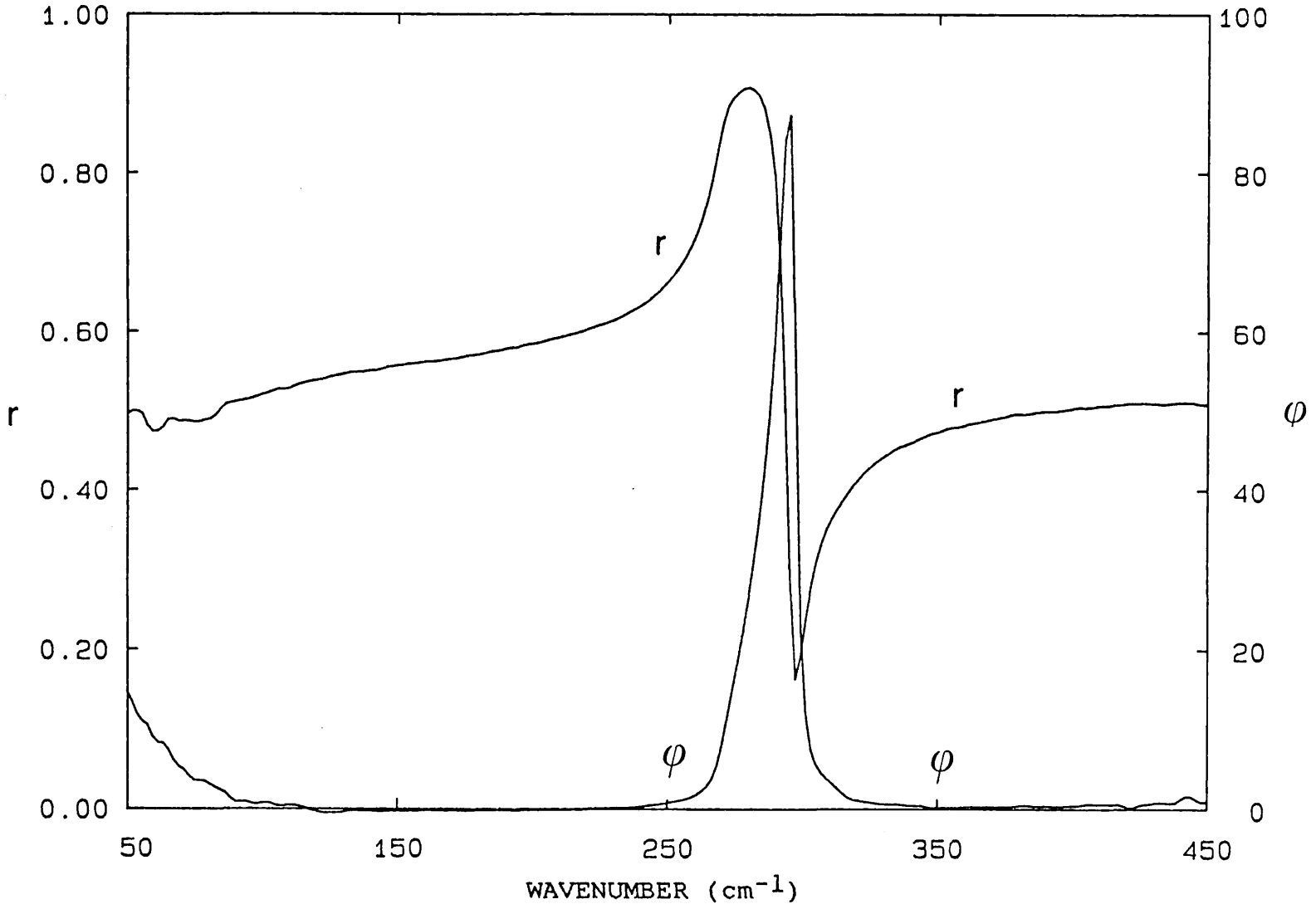

Figure 5.18 Complex reflectivity amplitude r and phase ϕ of GaAs at 300K

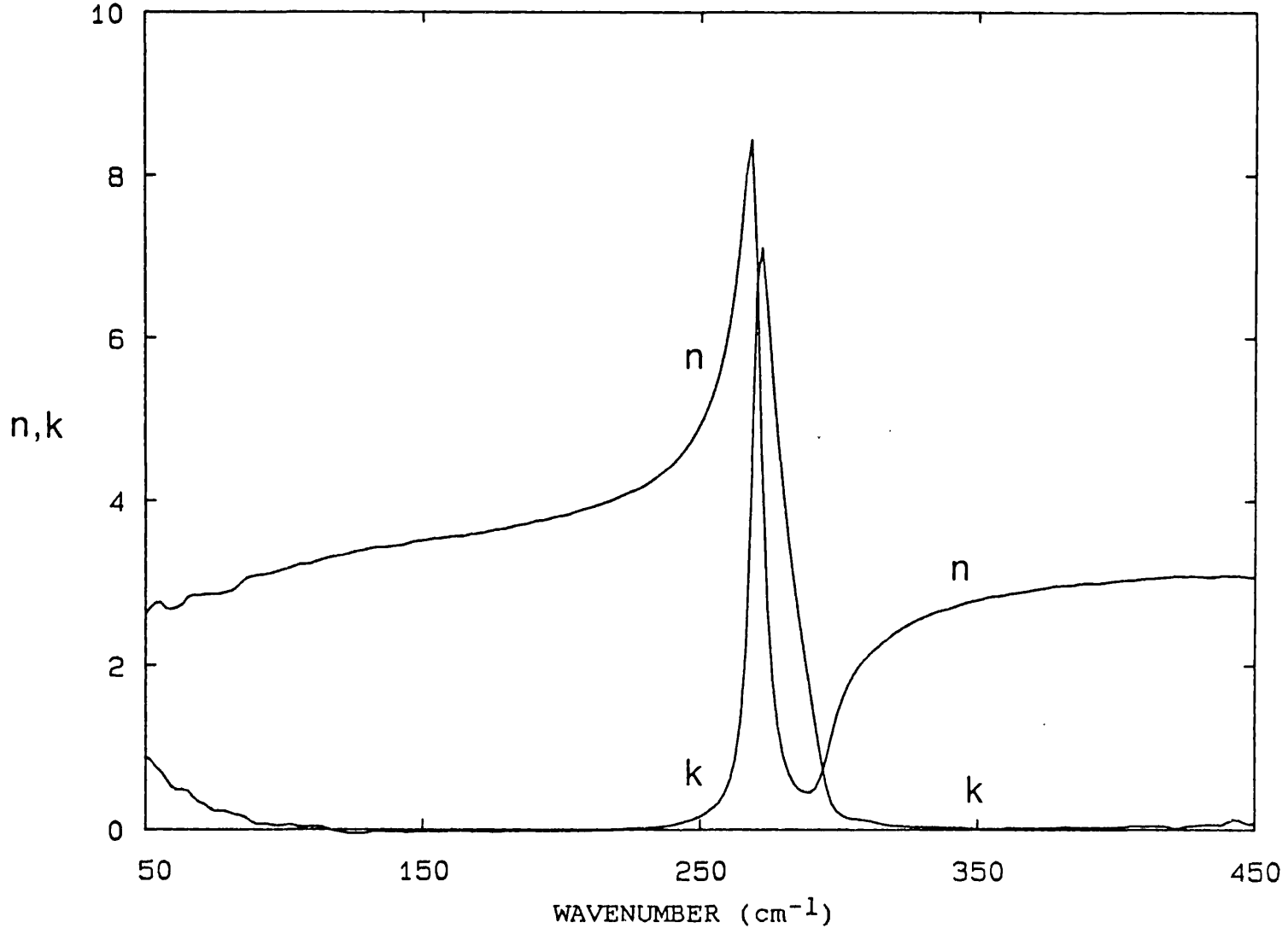

Figure 5.19 Refractive index n and absorption index k for GaAs at 300K

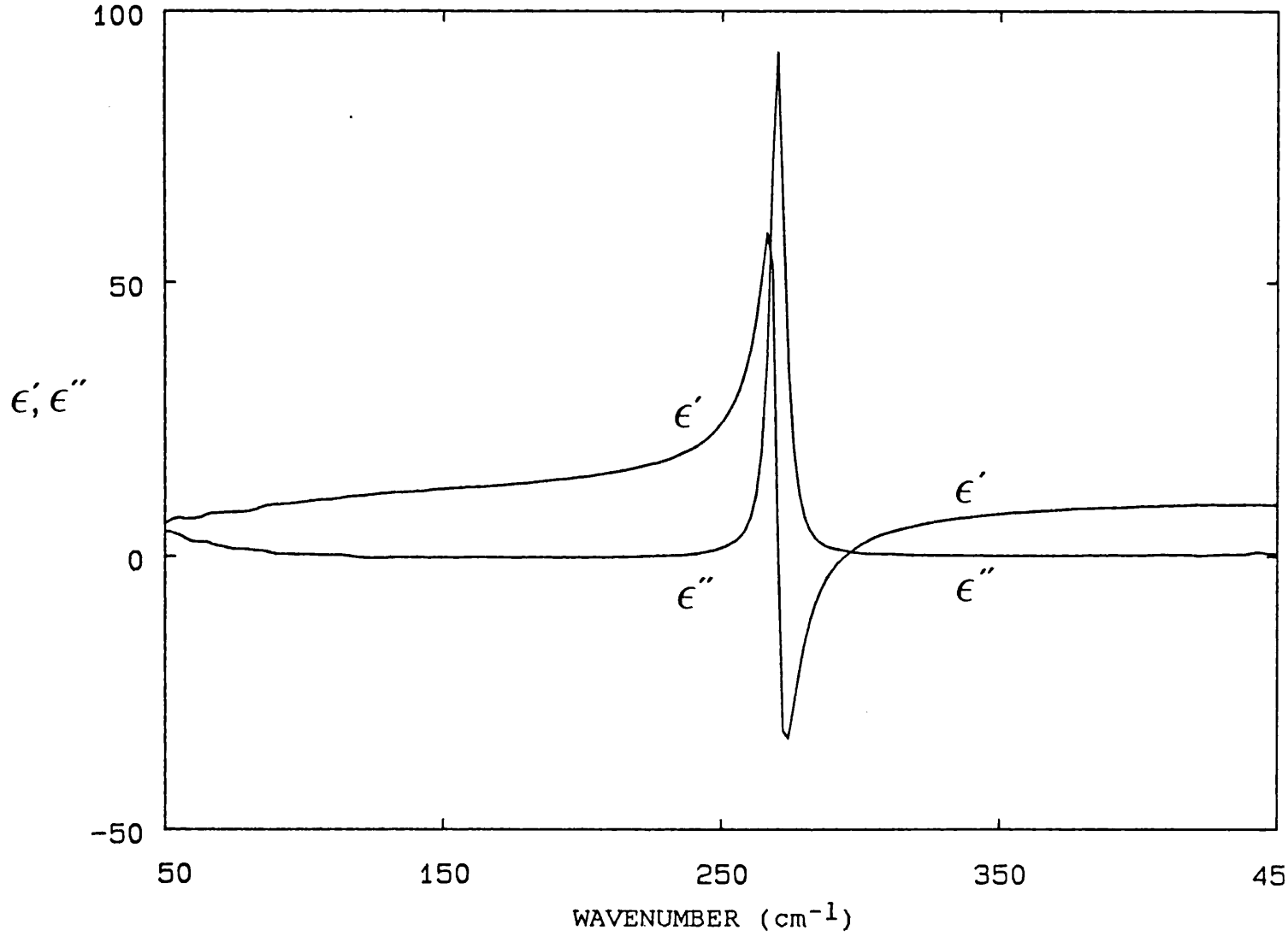

Figure 5.20 Real ϵ' and imaginary ϵ'' parts of the dielectric response for GaAs at 300K

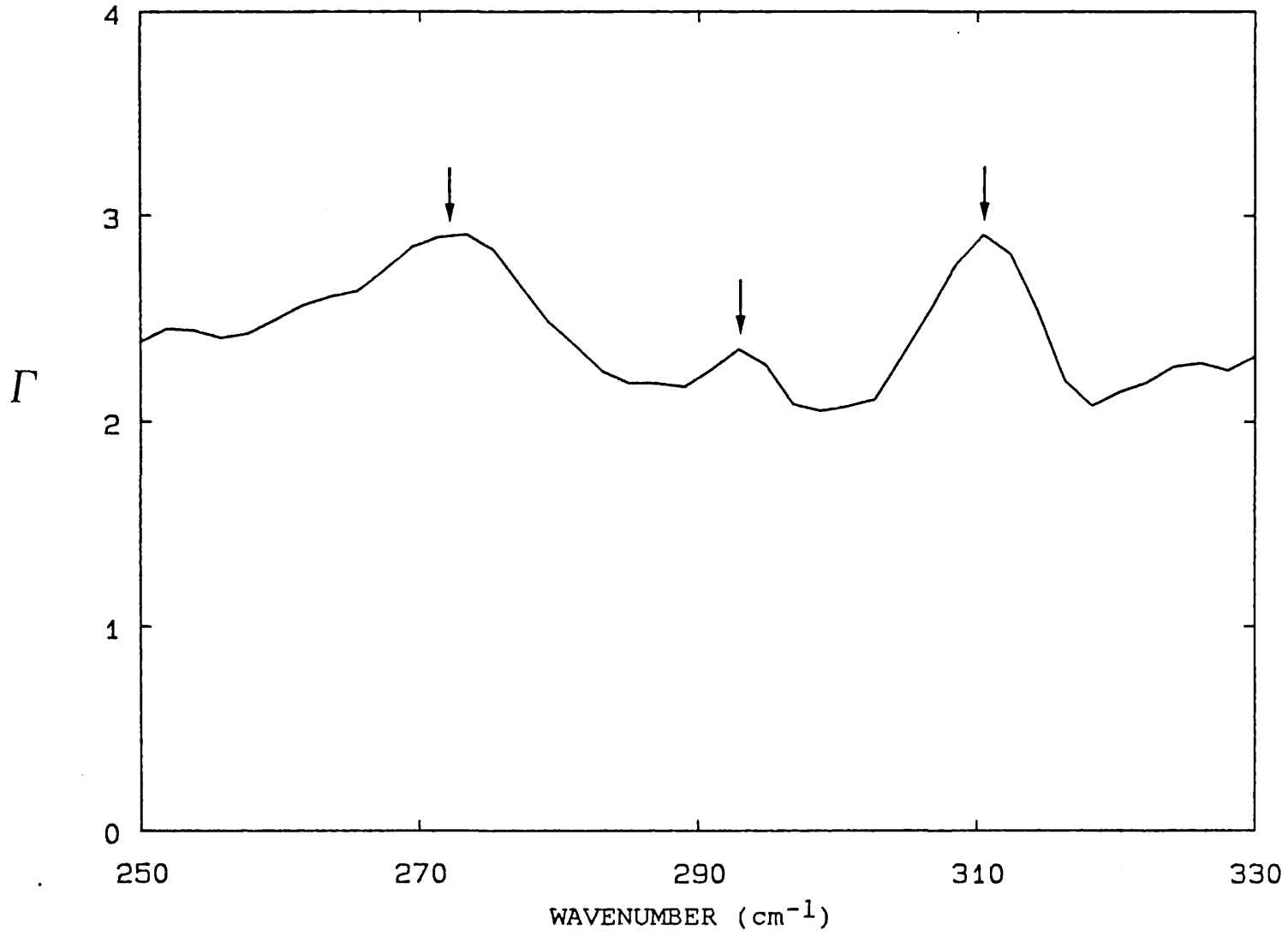

Figure 5.21 Plot of the anharmonic self energy function Γ for GaAs at 300K

5.6 Optical constant data of GaSb

The amplitude r and phase ϕ of the complex reflectivity were obtained for GaSb, as shown in figure (5.22). From these results were calculated the optical indices, n and k, shown in figure (5.23), and the dielectric functions, ϵ' and ϵ'', as shown in figure (5.24). From these the self energy function Γ was calculated, as shown in figure (5.25). This shows a number of prominent features, which have been assigned in table (5.6). These features along with the zone centre frequencies, TO(Γ) and LO(Γ), are compared with the RIM model of Patel (1982), neutron scattering data by Farr et al (1973), I.R. absorption work by Hrostowski and Fuller (1958) and Mitra (1963), and Raman scattering by Sekine et al (1976). The value obtained for the zone centre frequency TO(Γ) agrees very well with the Raman data and the RIM model, but the RIM result for LO(Γ) is too high. Also, all the possible two phonon combinations between 225 and 265 cm^{-1} are listed in table (5.5), and very good agreement is obtained with the experimental features. Free carrier effects were seen in the low frequency region, with the minimum of the reflectivity occurring at 30 cm^{-1}. By using this value as the plasma frequency, with an effective mass of 0.047 m_e, then equation (4.34) gives a free carrier concentration of 4.7 x 10^{14} cm^{-3}.

TABLE 5.6

GaSb assignments

OBSERVED FREQUENCY	NEUTRON	I.R ABSORPTION		RAMAN	RIM (11)	ASSIGNMENTS
	Ref 1	Ref 2	Ref 3	Ref 4	Ref 5	
227	222.9	–	–	–	227.7	LA(X) + TA(X)
227.5	229.0	231	–	227	228.8	TO(Γ)
237	–	–	–	–	239.9	$IIA\Sigma_1$ + $IA\Sigma_1$
237.5	–	240	–	237	243.1	LO(Γ)
243	–	–	244	–	242.1	W_4 + W_5
249	–	–	250	–	251.4	$IO\Sigma_1$ + $TA\Sigma_2$
258	250.6	–	–	256	255.5	LO(L) + TA(L)
	–	–	–	–	256.7	W_3 + W_6

Ref 1 Farr M.K et al; 1973.

Ref 2 Mitra S.S; 1963.

Ref 3 Hrostowski H.J and Fuller C.S; 1958.

Ref 4 Sekine T et al; 1976.

Ref 5 Patel C; 1982.

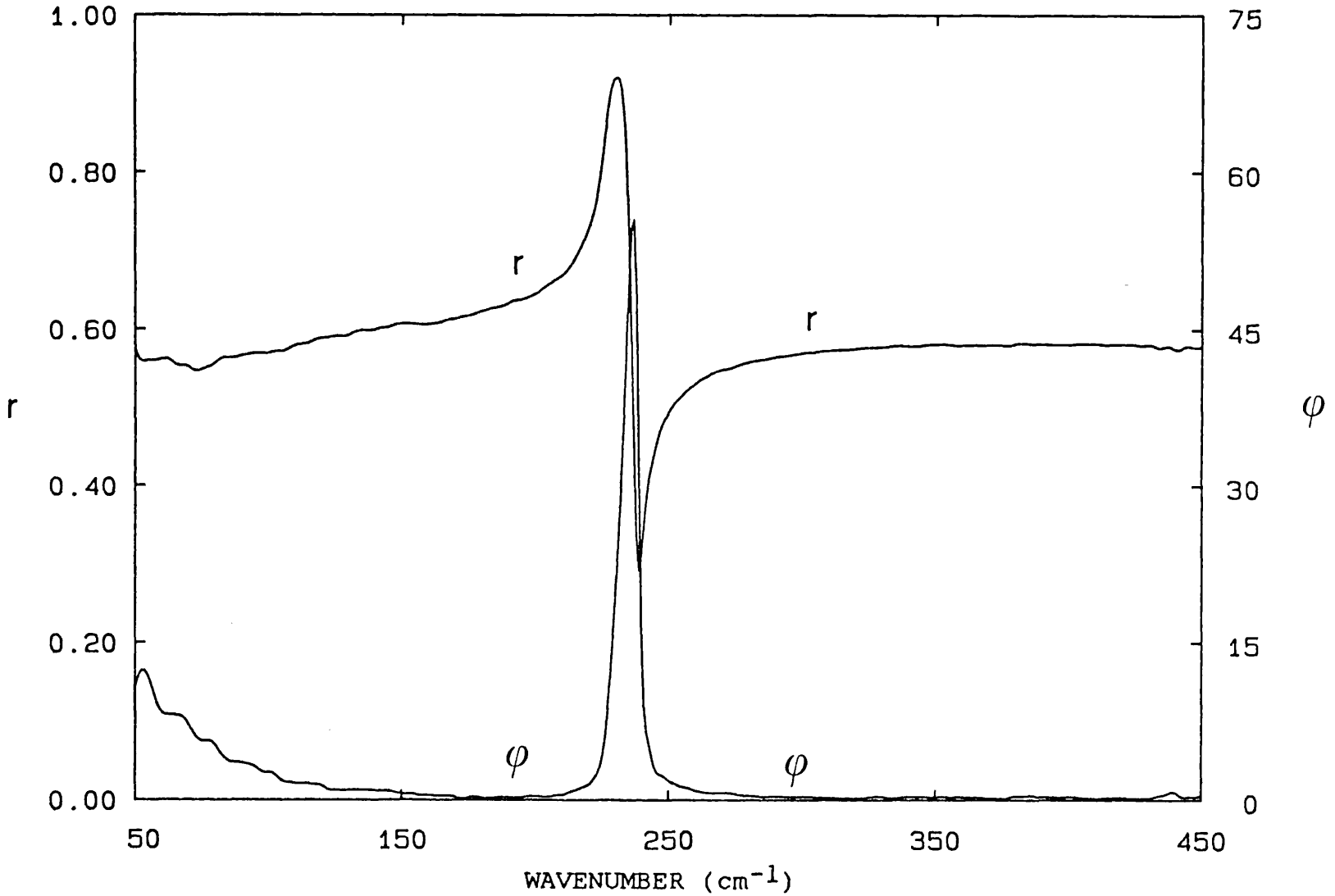

Figure 5.22 Complex reflectivity amplitude r and phase ϕ of GaSb at 300K

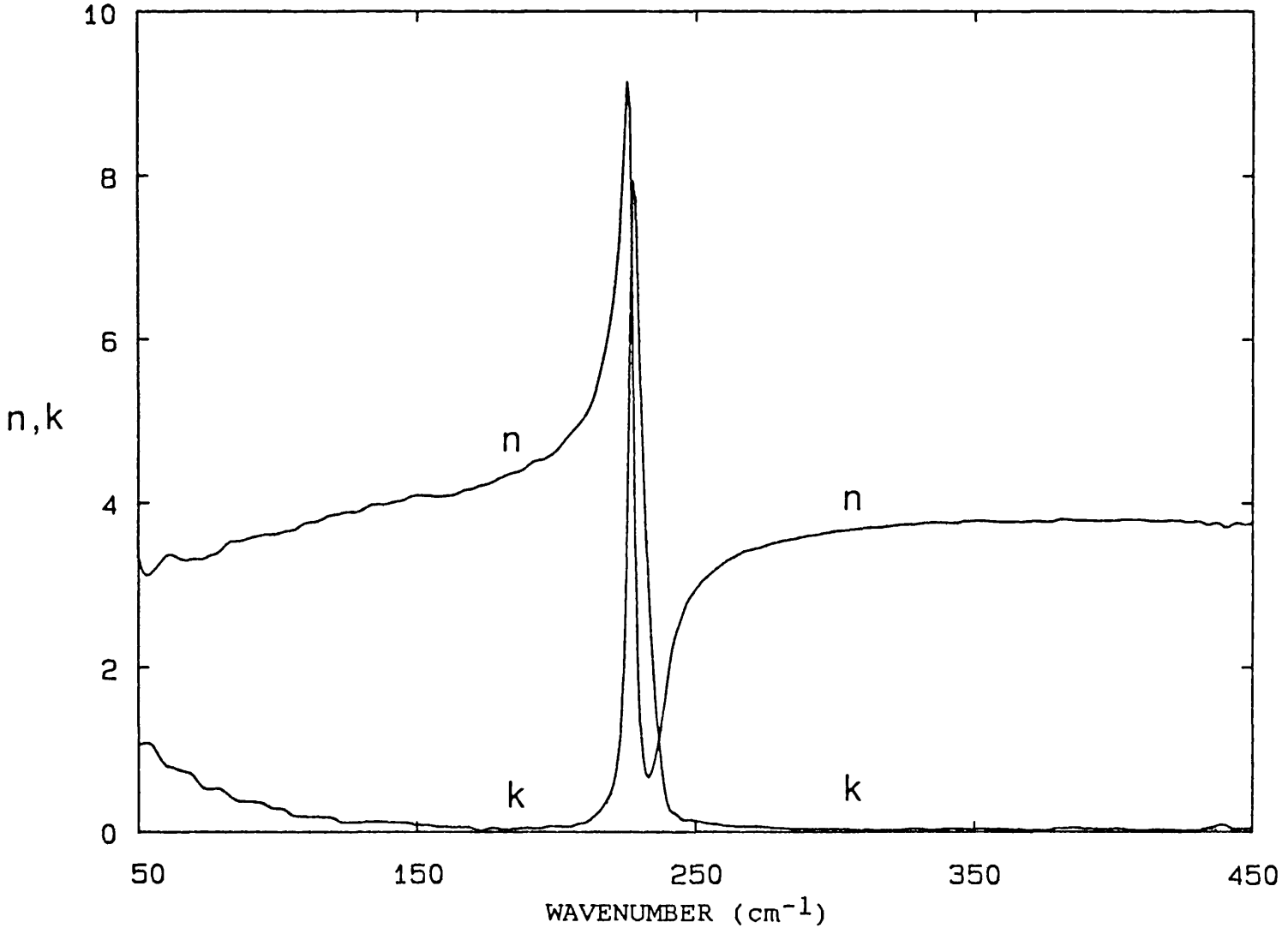

Figure 5.23 Refractive index n and absorption index k for GaSb at 300K

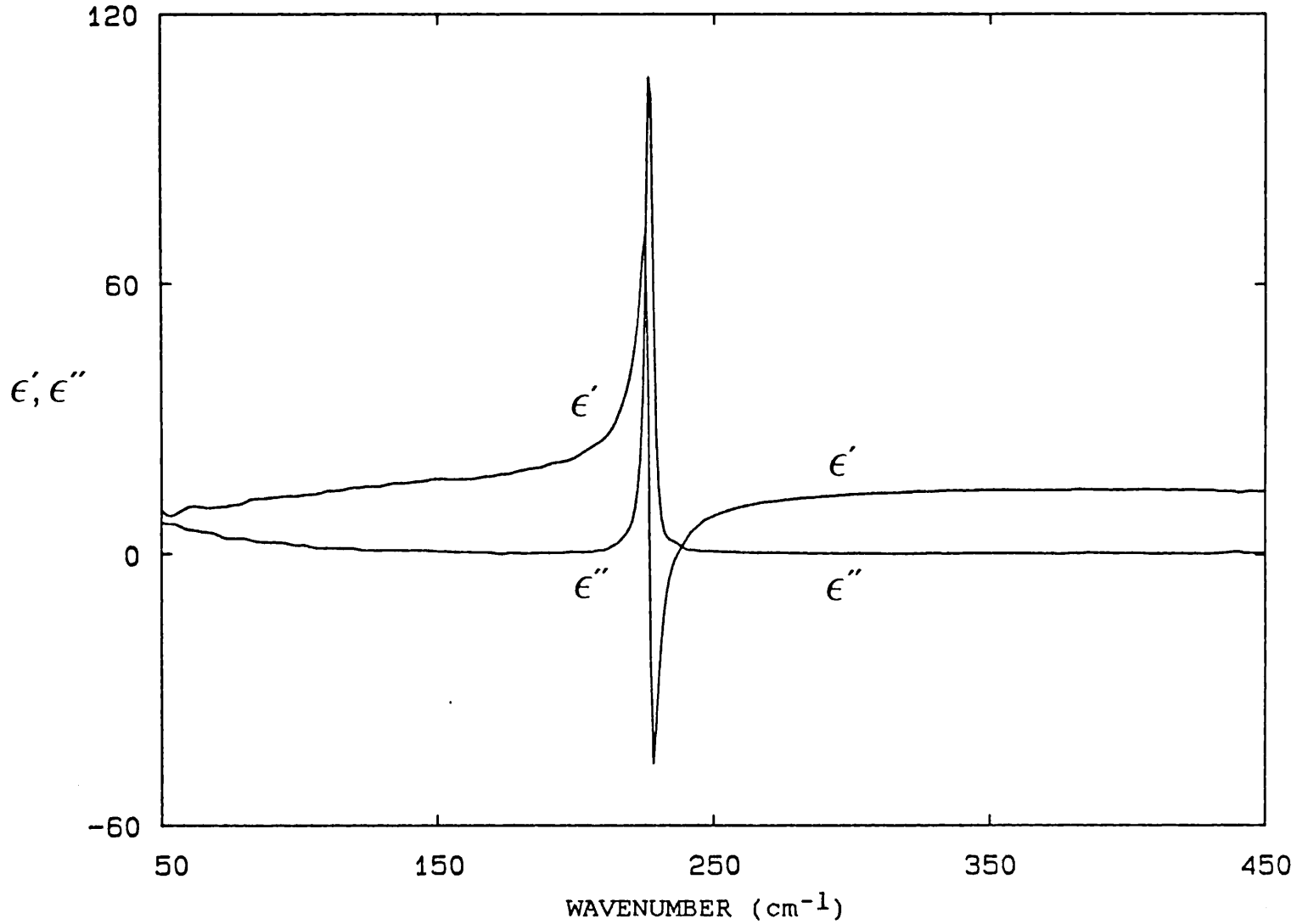

Figure 5.24 Real ϵ' and imaginary ϵ" parts of the dielectric response for GaSb at 300K

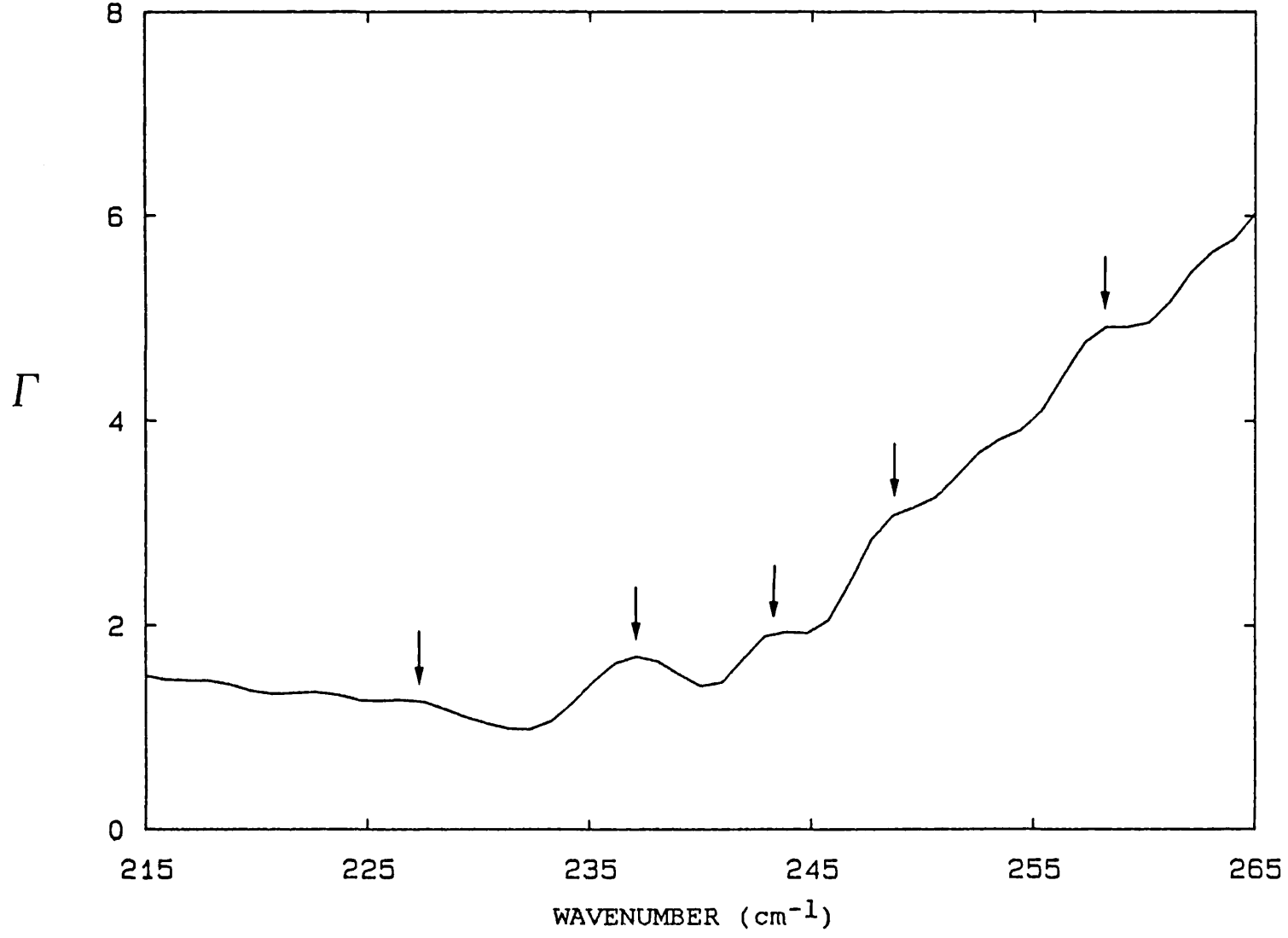

Figure 5.25 Plot of the anharmonic self energy function Γ for GaSb at 300K

5.7 Optical constant data of GaP

The amplitude r and phase ϕ of the complex reflectivity of GaP are shown in figure (5.26), and the calculated values of n and k are shown in figure (5.27), and ϵ' and ϵ'' in figure (5.28). These have been used to calculate the self energy function Γ as shown in figure (5.29), which shows a number of features. These, along with the zone centre frequencies obtained from the dielectric functions, are given in table (5.7). The values and assignments are compared to neutron data of Borcherds et al (1979) and Yarnell et al (1968), I.R. transmission data by Kleinman and Spitzer (1980) and Raman work by Hobden and Russell (1964). Two neutron sets are listed as the value of LO(Γ) and other C.P.P frequencies are different between the two groups, with no explanation of this discrepency. The TO(Γ) and LO(Γ) values agree very well with reported results, with the exception of the neutron data of Borcherds et al. No two phonon combinations can be found for the features at 396, 403 and 441 cm^{-1}, although three-phonon combinations can be found, such as

$$TO(L) - LO(L) + TO(X) = 395\ cm^{-1}$$

$$2 \times LA(X) - TA(X) \quad = 402\ cm^{-1}$$

The feature at 441 cm^{-1} has been reported before from I.R. transmission work as an impurity band due to Aluminium, although at 444.7 cm^{-1}. No free carrier effects have been seen in this sample down to 20 cm^{-1}, giving a maximum carrier concentration of 6×10^{14} cm^{-3} using equation (4.34) and an effective mass of 0.13 m_e.

TABLE 5.7

GaP assignments

OBSERVED FREQUENCY	NEUTRON		I.R	RAMAN	RIM (11)	ASSIGNMENTS
	Ref 1	Ref 2	Ref 3	Ref 4	Ref 5	
360	354.3	355.9	–	–	360.3	LA(X) + TA(X)
367	–	367.0	366	367	368.3	TO(Γ)
379	–	–	–	–	380.5	$W_4 + W_5$
396	–	–	–	–	395.4	3 phonons ?
403	–	–	–	–	402.3	3 phonons ?
403	408.3	402.0	402	403	402.8	LO(Γ)
425	–	–	426	428	428.4	2LA(L)
441	–	–	445	–	–	impurity ?
447	436.6	443.0	–	–	436.1	TO(L) + TA(L)

Ref 1 Borcherds P.H et al; 1979

Ref 2 Yarnell J.L et al; 1968.

Ref 3 Kleinman D.A and Spitzer W.G; 1960.

Ref 4 Hobden M.V and Russell J.P; 1964.

Ref 5 Patel C; 1982.

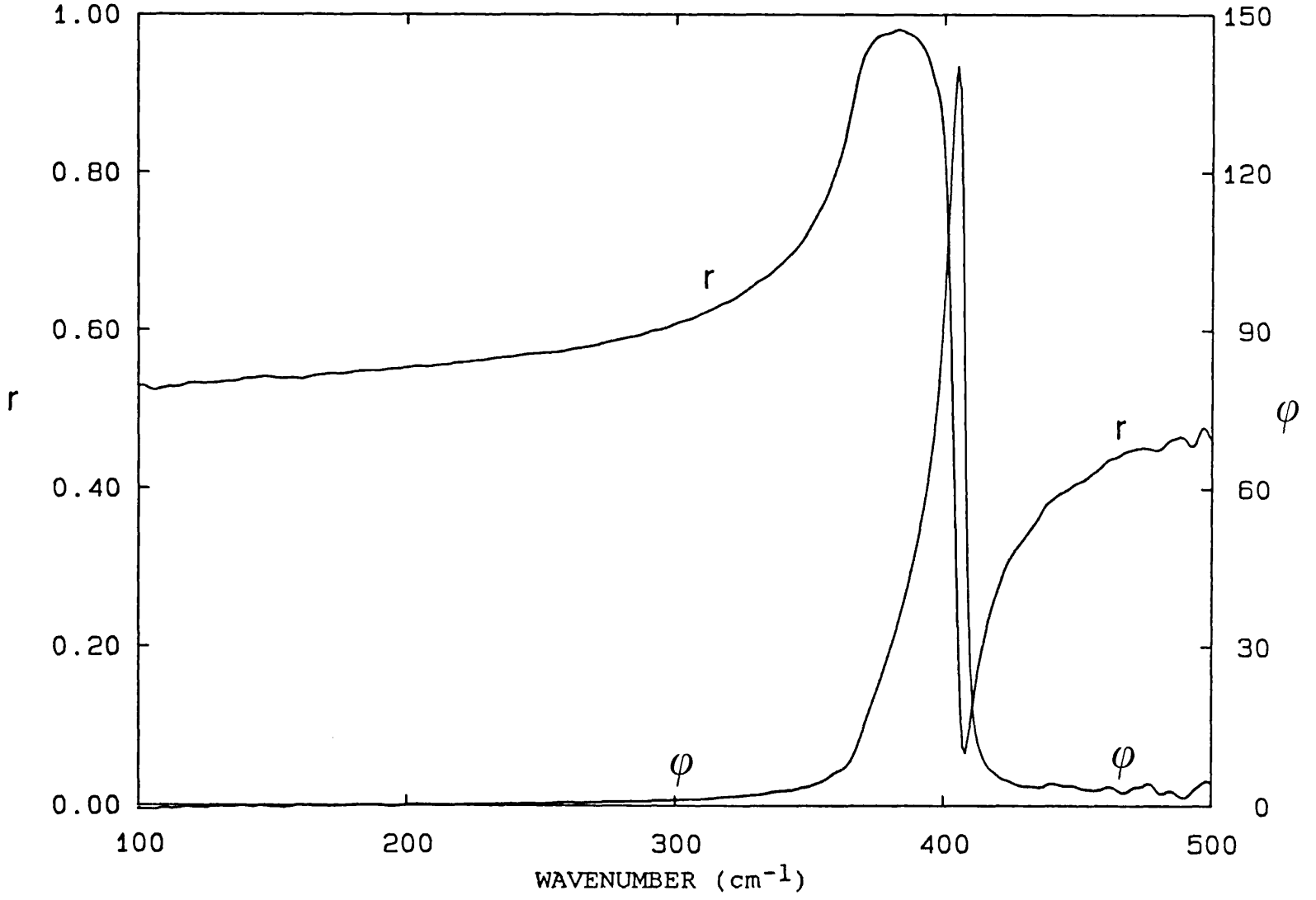

Figure 5.26 Complex reflectivity amplitude r and phase ϕ of GaP at 300K

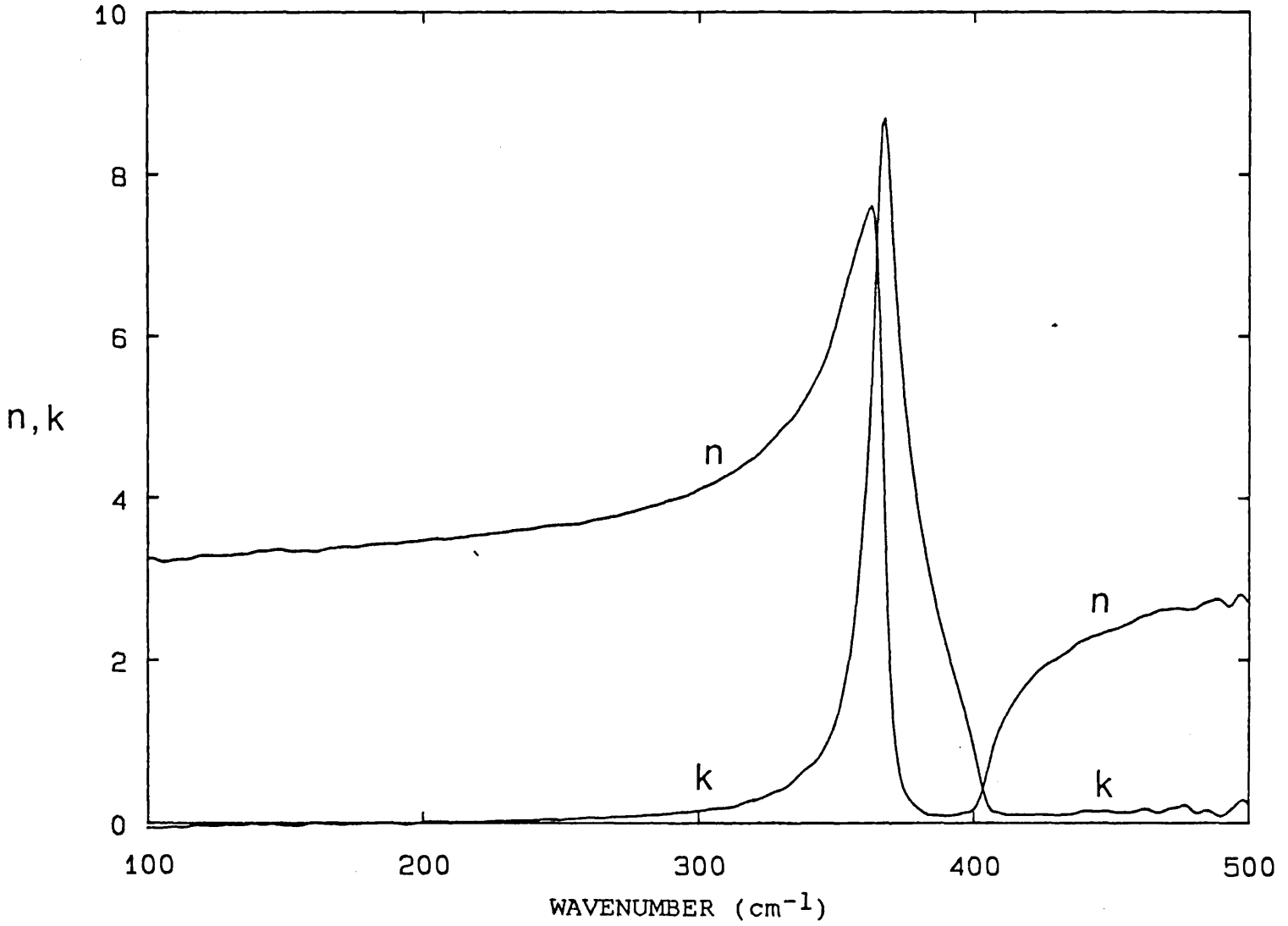

Figure 5.27 Refractive index n and absorption index k for GaP at 300K

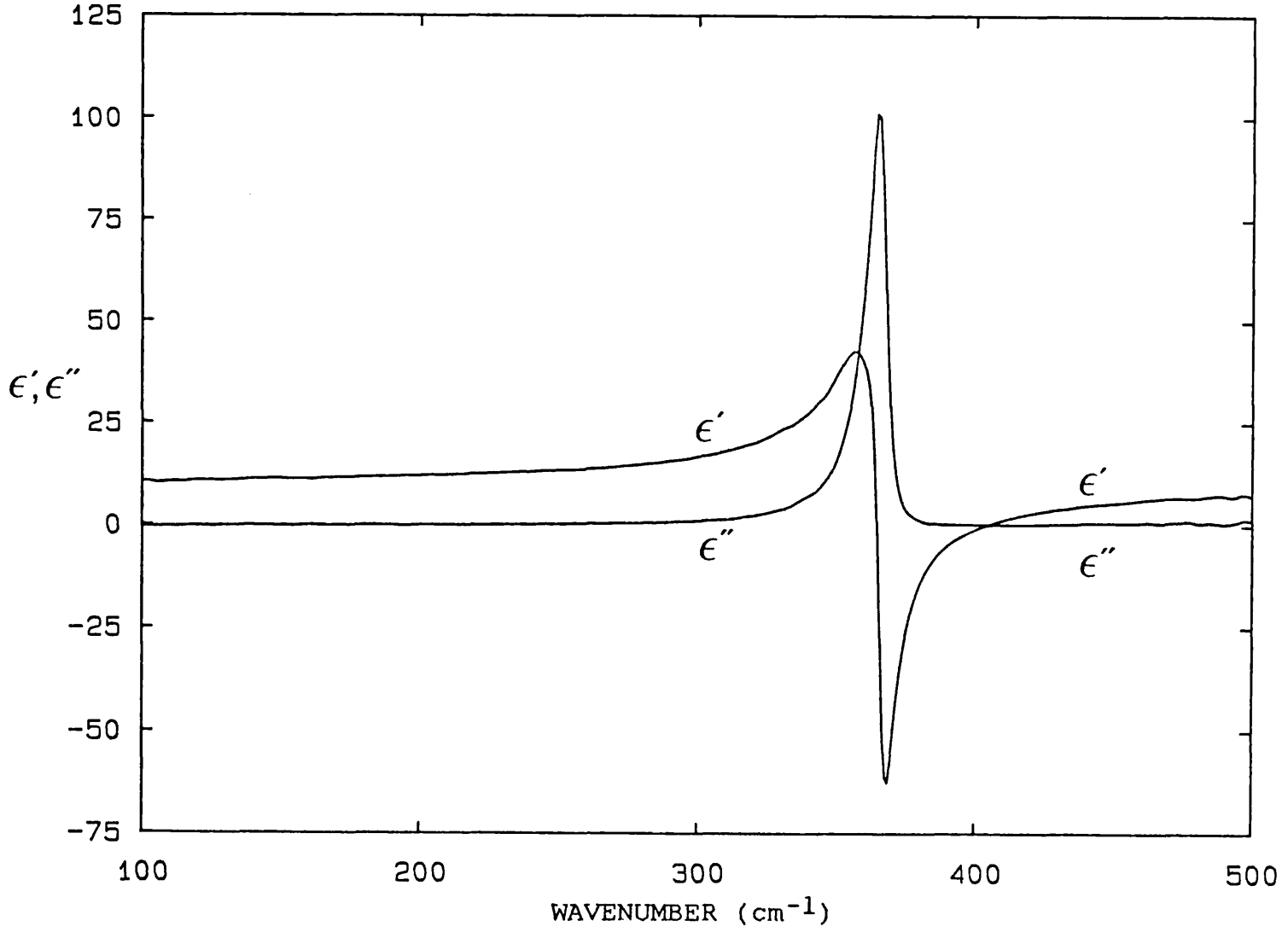

Figure 5.28 Real ϵ' and imaginary ϵ" parts of the dielectric response for GaP at 300K

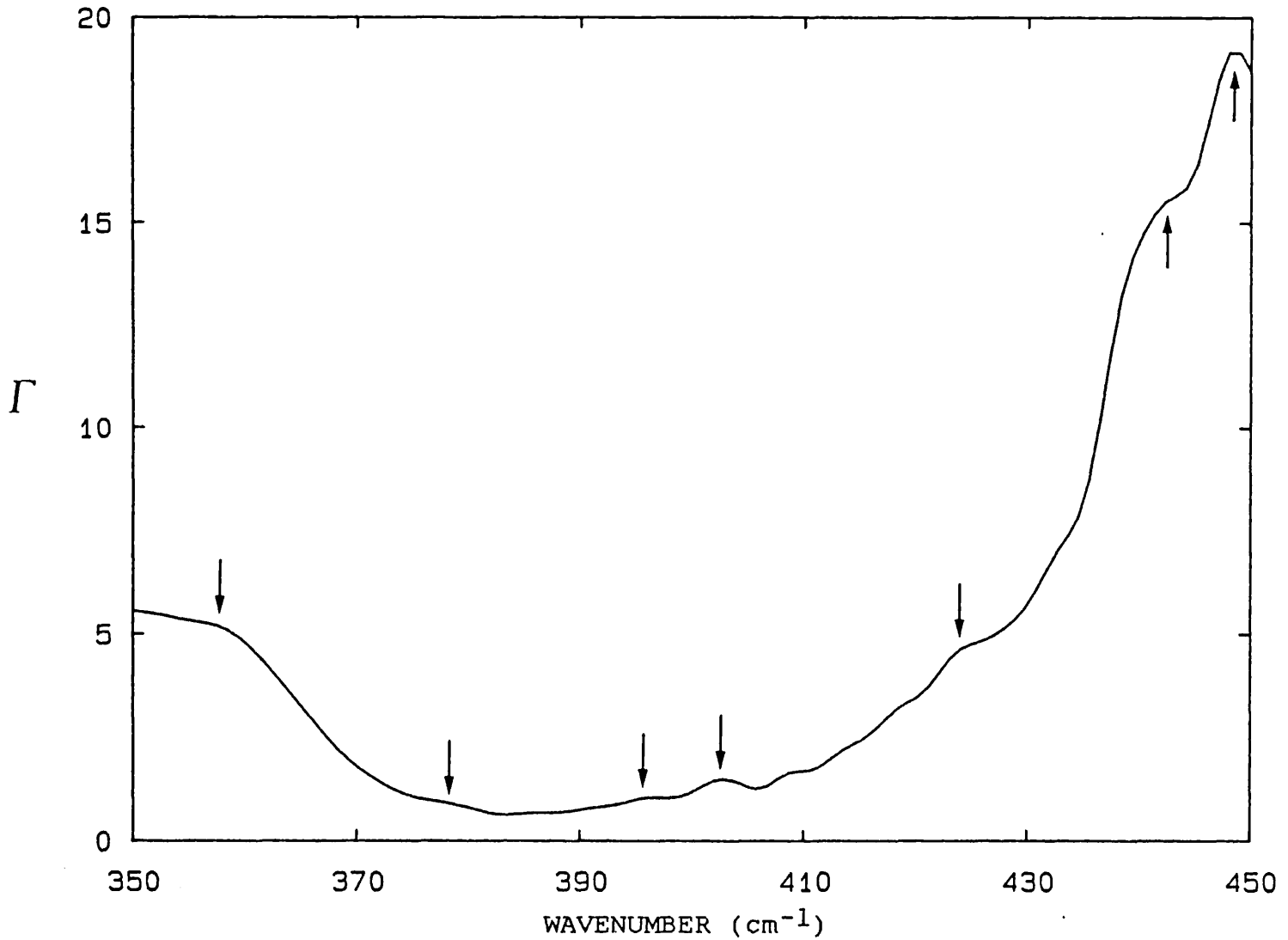

Figure 5.29 Plot of the anharmonic self energy function Γ for InSb at 300K

5.8 Optical constant data of ZnSe

The amplitude r and the phase ϕ of the complex reflectivity of ZnSe have been measured, as shown in figure (5.30). From this have been calculated the refractive index n and the absorption index k, shown in figure (5.31). Then these can be used to calculate the dielectric responses, ϵ' and ϵ'', as shown in figure (5.32). The self energy function Γ can be determined from these functions, and is shown in figure (5.33). A number of pronounced features can be seen, with their positions being tabulated in table (5.8), along with the values of TO(Γ) and LO(Γ) as obtained from the dielectric response. Also in the table are values obtained by the 11 parameter RIM model by Patel (1982), neutron scattering results by Hennion et al (1971) and Raman results by Irwin and LaCombe (1972). The experimental value for TO(Γ) is in very good agreement with the RIM model and the Raman results, although the neutron result is too high. The value for LO(Γ) of 253 cm^{-1} agrees with the neutron result, although the Raman result and I.R absorption work by Aven et al (1961) give values near 250cm^{-1}. The other features can be assigned by two phonon processes, except for the feature at 211 cm^{-1}, which could be due to a three phonon combination of TA(X). Apart from the feature at 225 cm^{-1}, there is no published work on the other bands observed.

No free carrier effects were seen down to 25 cm^{-1}.

TABLE 5.8

ZnSe assignments

OBSERVED FREQUENCY	NEUTRON Ref 1	RAMAN Ref 2	RIM (11) Ref 3	ASSIGNMENTS
180	177	_	180.1	LO(L) - TA(L)
207	213	206	206.2	TO(Γ)
211	210	_	210.3	3TA(X) ?
225	223	228	218.2	LA(L) + TA(L)
253	253	250	249.2	LO(Γ)
253	264	_	257.3	LA(X) + TA(X)
271	283	_	276.3	LO(X) + TA(X)
292	289	_	286.7	TO(X) + TA(X)
	291	_	288.3	LO(L) + TA(L)

Ref 1 Hennion B et al; 1971.

Ref 2 Irwin J.C and LaCombe J; 1972.

Ref 3 Patel C; 1982.

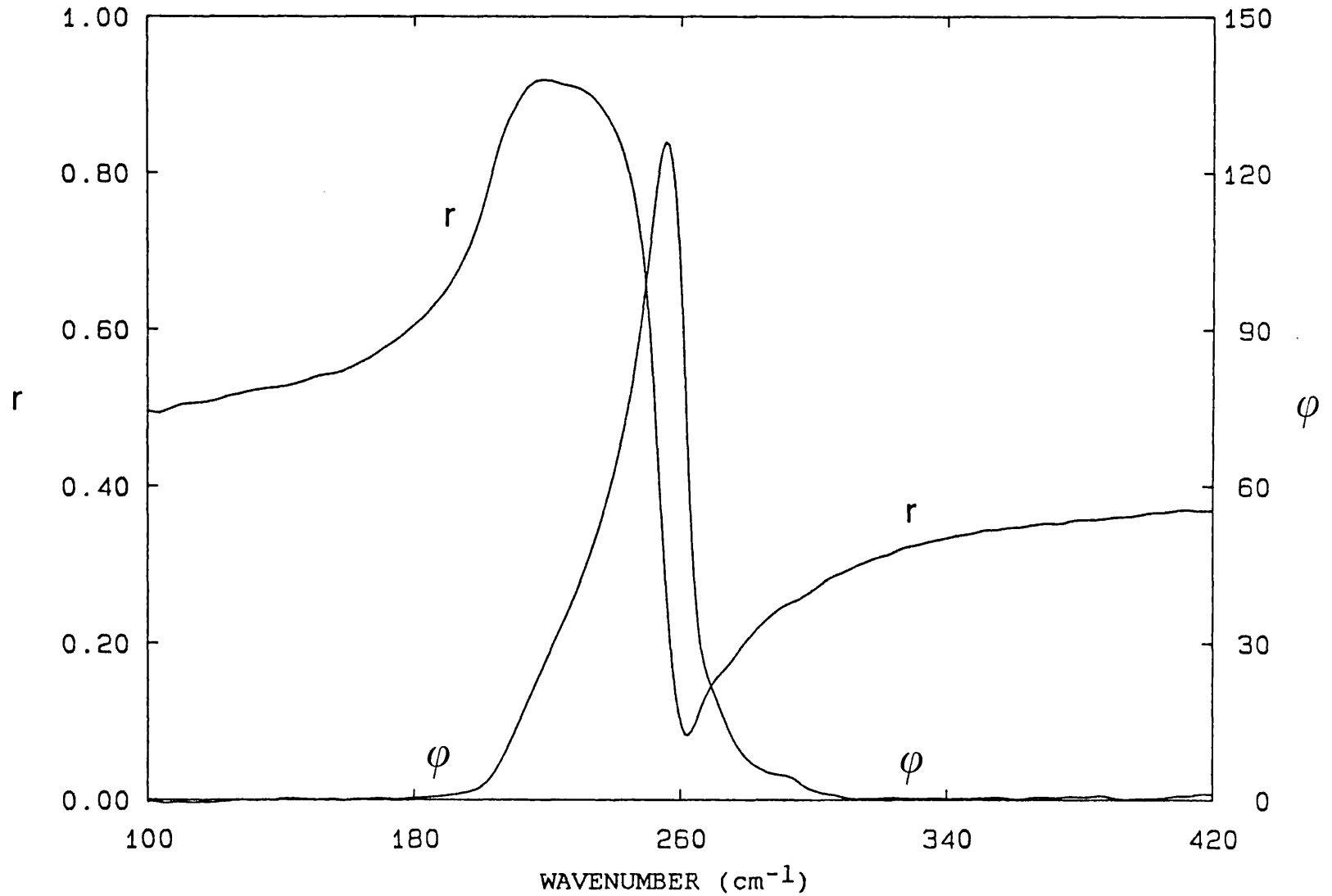

Figure 5.30 Complex reflectivity amplitude r and phase ϕ of ZnSe at 300K

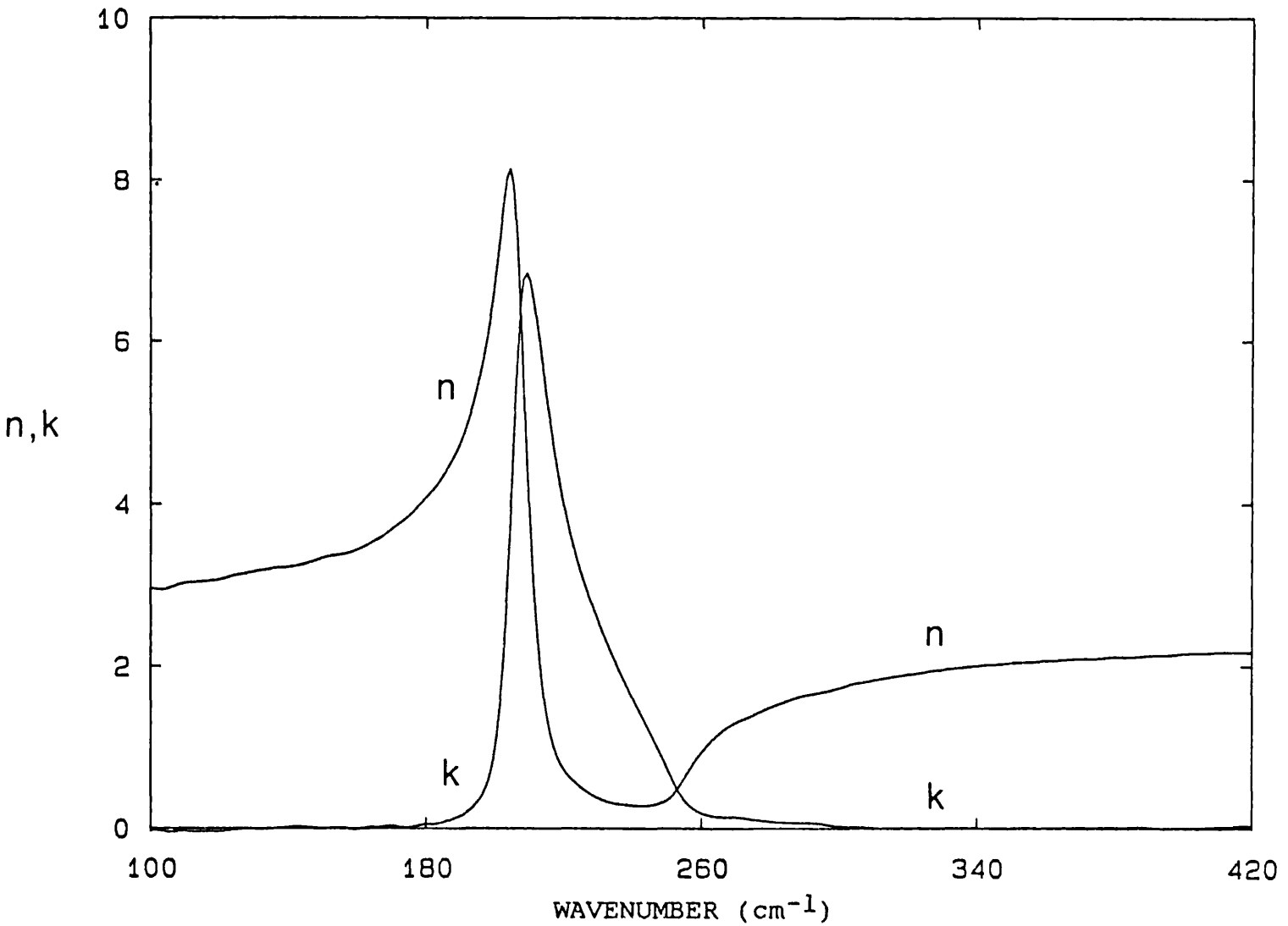

Figure 5.31 Refractive index n and absorption index k for ZnSe at 300K

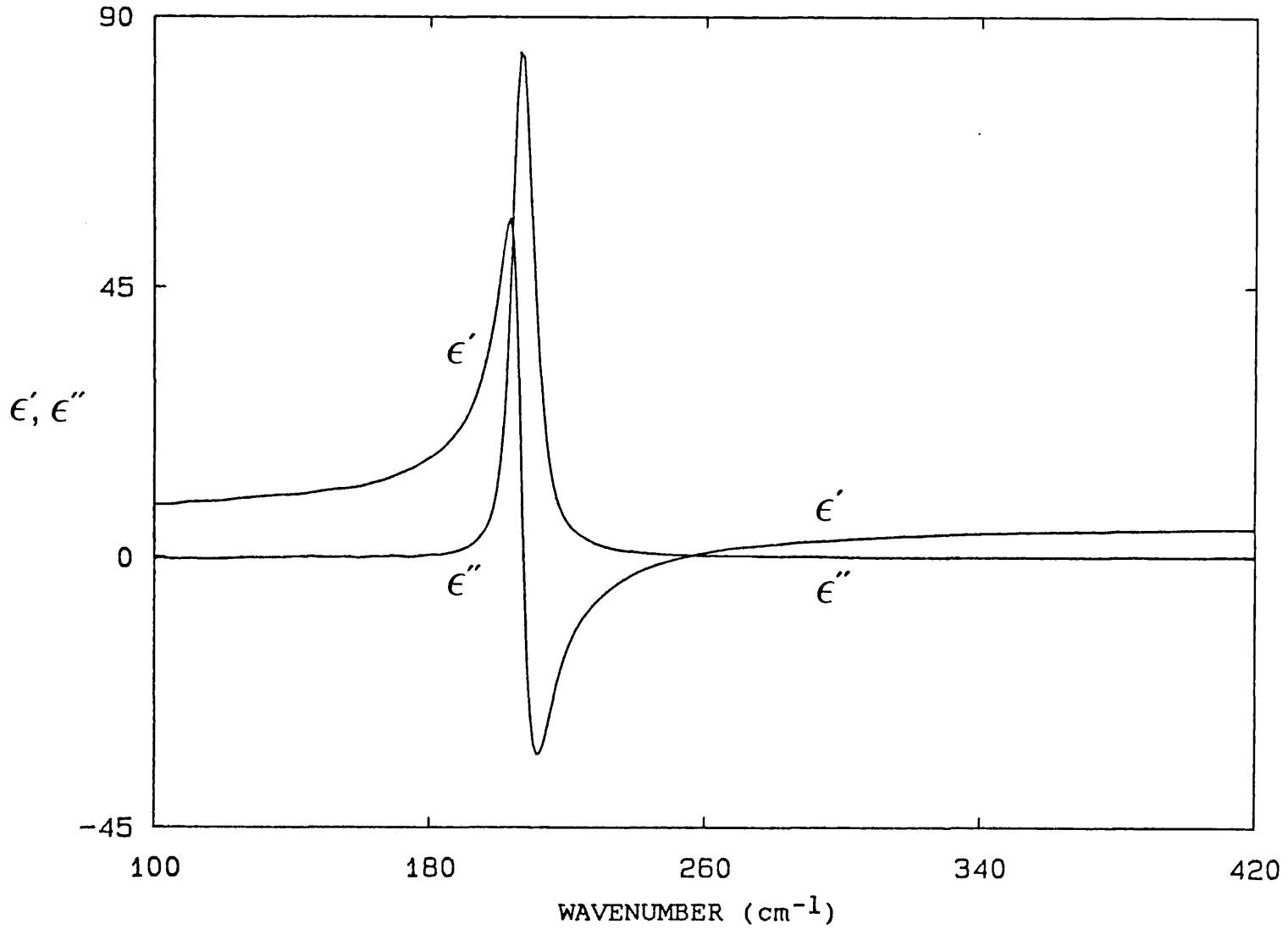

Figure 5.32 Real ϵ' and imaginary ϵ" parts of the dielectric response for ZnSe at 300K

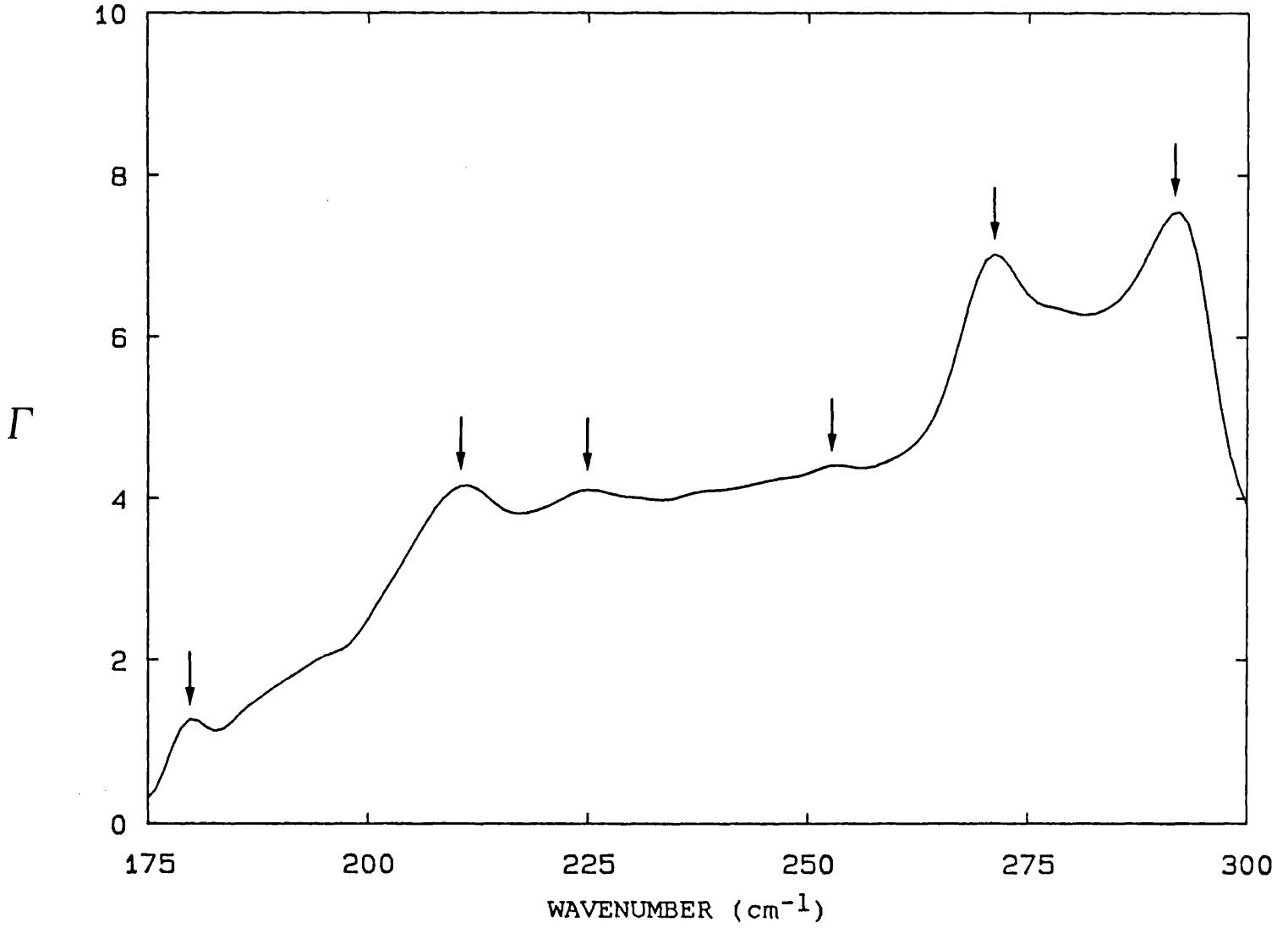

Figure 5.33 Plot of the anharmonic self energy function Γ for ZnSe at 300K

5.9 Optical constant data of CdTe

Figure (5.34) shows the amplitude r and the phase ϕ of the complex reflectivity for CdTe. These have been used to determine the refractive index n and absorption index k, as shown in figure (5.35), as well as the dielectric response functions ϵ' and ϵ'', as shown in figure (5.36). The self energy function Γ can then be determined, and is shown in figure (5.37). From the dielectric response, the values for the zone centre frequencies TO(Γ) and LO(Γ) can be determined, and these along with the features observed in the self energy function are shown in table (5.9). This work is compared to the RIM model of Patel (1982), neutron scattering results of Rowe et al (1974), I.R absorption work by Slack et al (1966) and Raman scattering by Mooradian and Wright (1968). As can be seen from the table, the value for TO(Γ) is in good agreement with previously reported values, although the value of LO(Γ) does not agree. The feature at 186 cm^{-1} has been observed before in Raman spectroscopy, but no clear assignments can be made for the other two features at 175 and 207 cm^{-1}. There are no two phonon combinations around 210 cm^{-1}, so three phonon processes have been used.

No effects of free carriers were seen down to 25 cm^{-1}.

TABLE 5.9

CdTe assignments

OBSERVED FREQUENCY	NEUTRON	I.R	RAMAN	RIM (11)	ASSIGNMENT
		300 K	300 K		
	Ref 1	Ref 2	Ref 3	Ref 4	
141	140.1	141	140	140.1	TO(Γ)
167.5	169.5	178	171	169.4	LO(Γ)
175	173.3	–	–	173.8	TO(L) + TA(L)
175	173.3	–	–	177.8	LO(L) + TA(L)
186	183.1	–	186	187.6	TO(X) + TA(X)
207	–	–	203	206.7	2LA(X) - TA(X)
207	202.6	–	203	207.3	2TA(L) + LO(L)

Ref 1 Rowe J.M et al; 1974.

Ref 2 Slack G.A et al; 1966.

Ref 3 Mooradian A and Wright G.B; 1968.

Ref 4 Patel C; 1982.

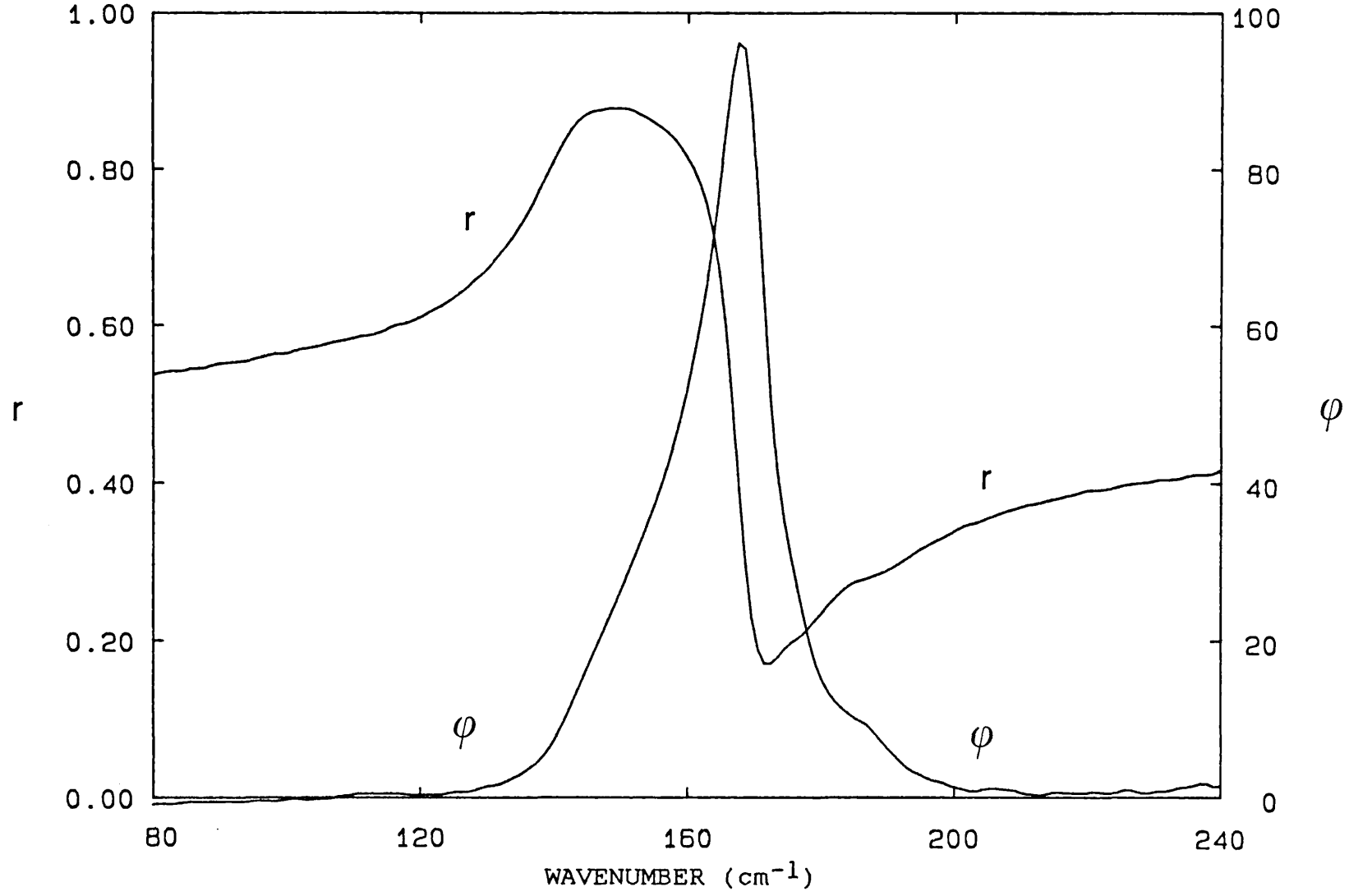

Figure 5.34 Complex reflectivity amplitude r and phase ϕ of CdTe at 300K

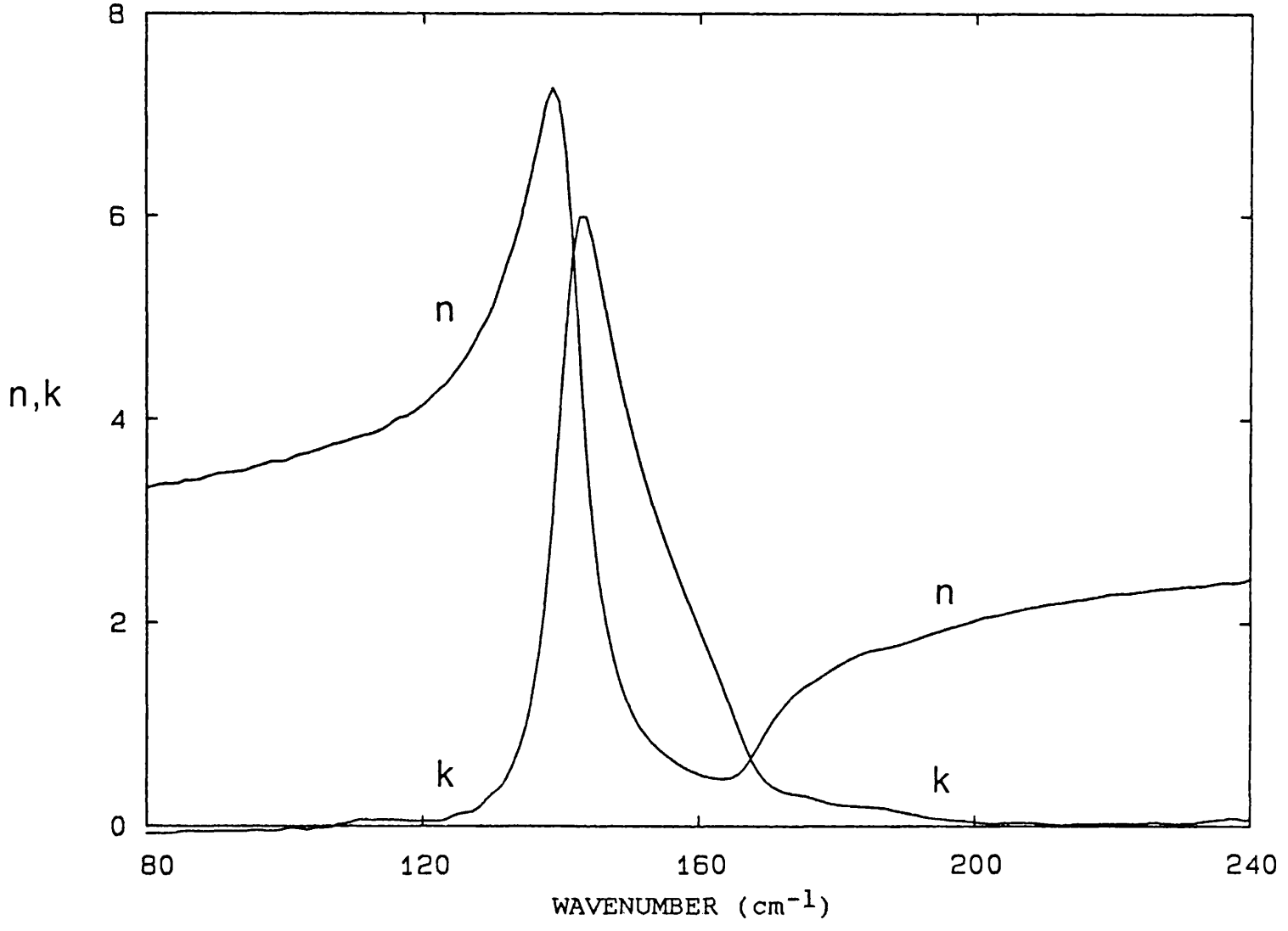

Figure 5.35 Refractive index n and absorption index k for CdTe at 300K

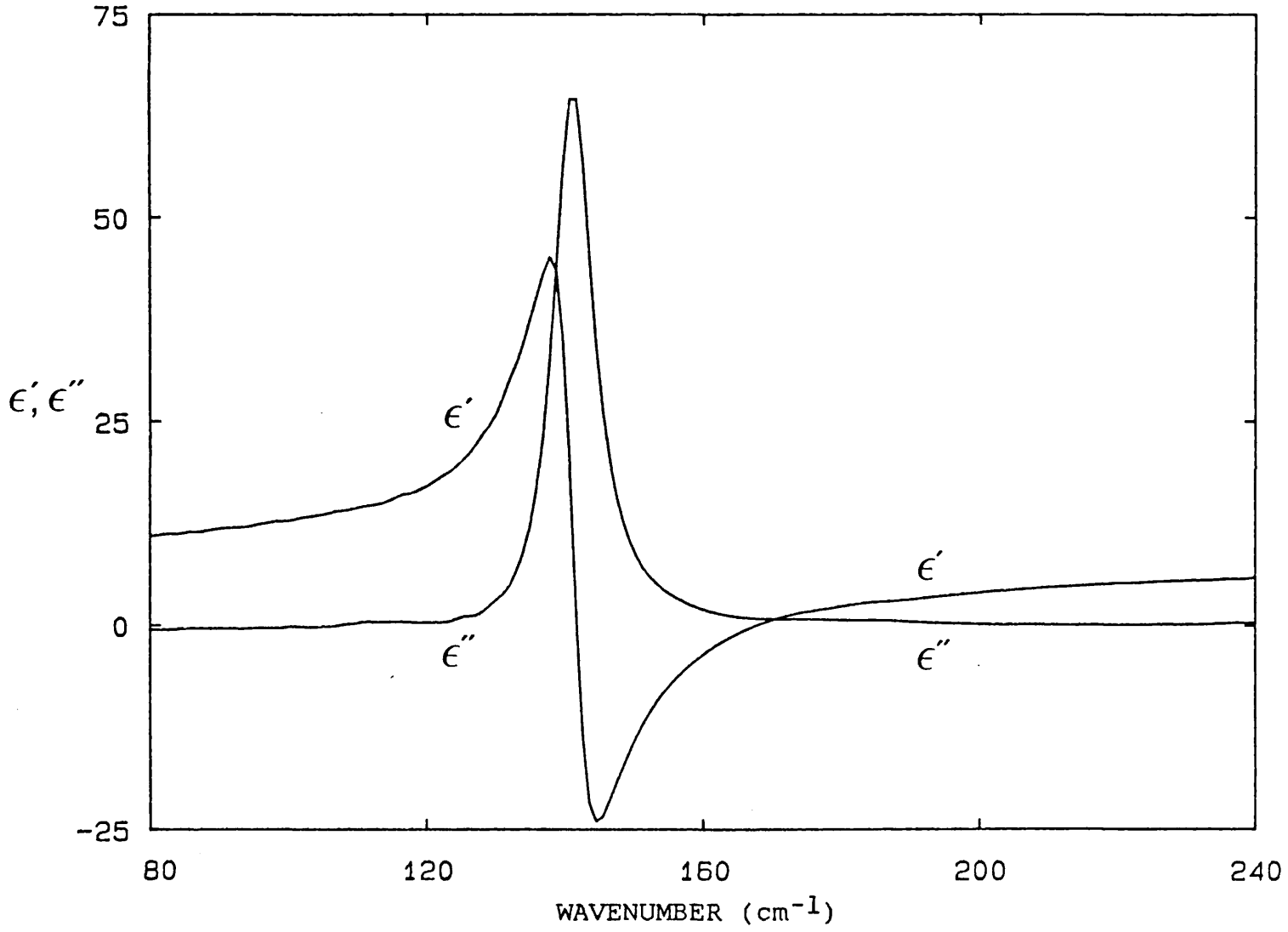

Figure 5.36 Real ϵ' and imaginary ϵ" parts of the dielectric response for CdTe at 300K

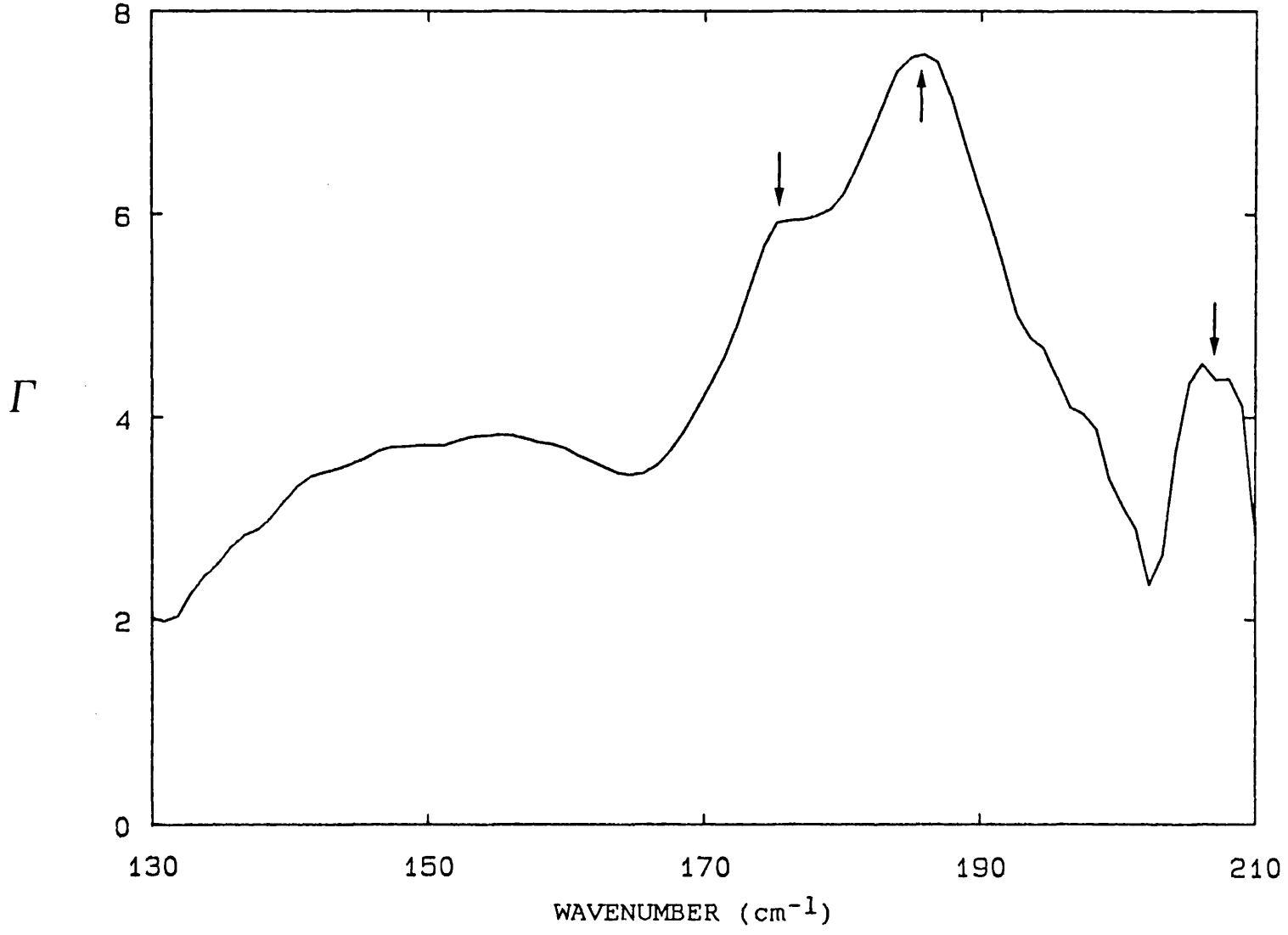

Figure 5.37 Plot of the anharmonic self energy function Γ for CdTe at 300K

5.10 Optical constant data of CaF_2

The reststrahl region for the alkaline earth flourides is very broad, covering about 200 cm^{-1} between the TO(Γ) and LO(Γ). The amplitude r and the phase ϕ of the complex reflectivity for CaF_2 is shown in figure (5.38). From this has been calculated the refractive index n and the absorption index k, as shown in figure (5.39). Also the dielectric response functions ϵ' and ϵ'' have been calculated, and are shown in figure (5.40). These functions have been used to calculate the anharmonic self energy function Γ, figure (5.41), which shows a number of features. From the dielectric functions, the zone centre frequencies TO(Γ) and LO(Γ) can be obtained, which are 262 cm^{-1} and 488 cm^{-1}. This compares quite well with earlier work by Lowndes (1971), in which values of 263 cm^{-1} for TO(Γ) and 482 cm^{-1} for LO(Γ) were reported.

The features observed in the self energy function have not been reported previously.

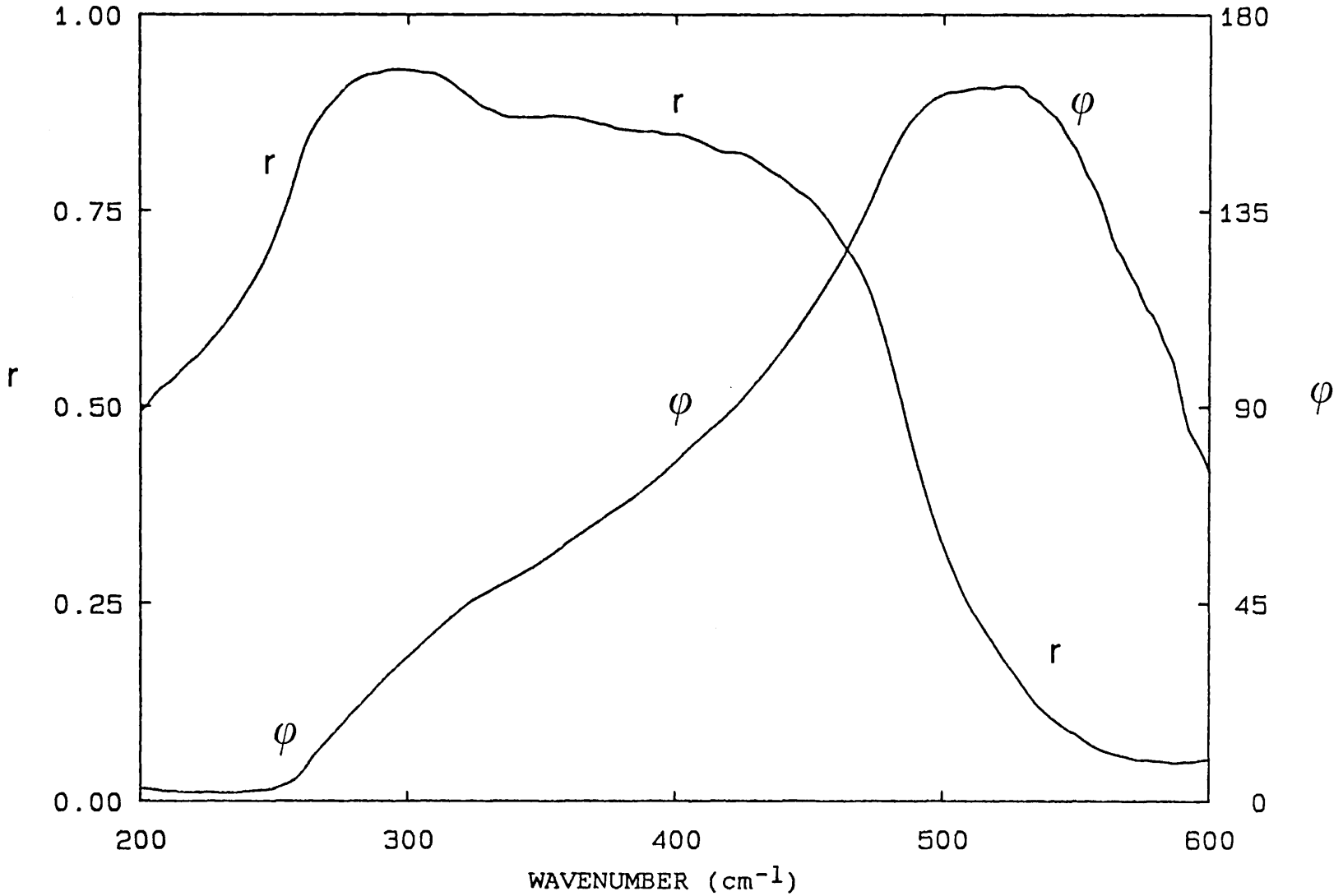

Figure 5.38 Complex reflectivity amplitude r and phase ϕ of CaF_2 at 300K

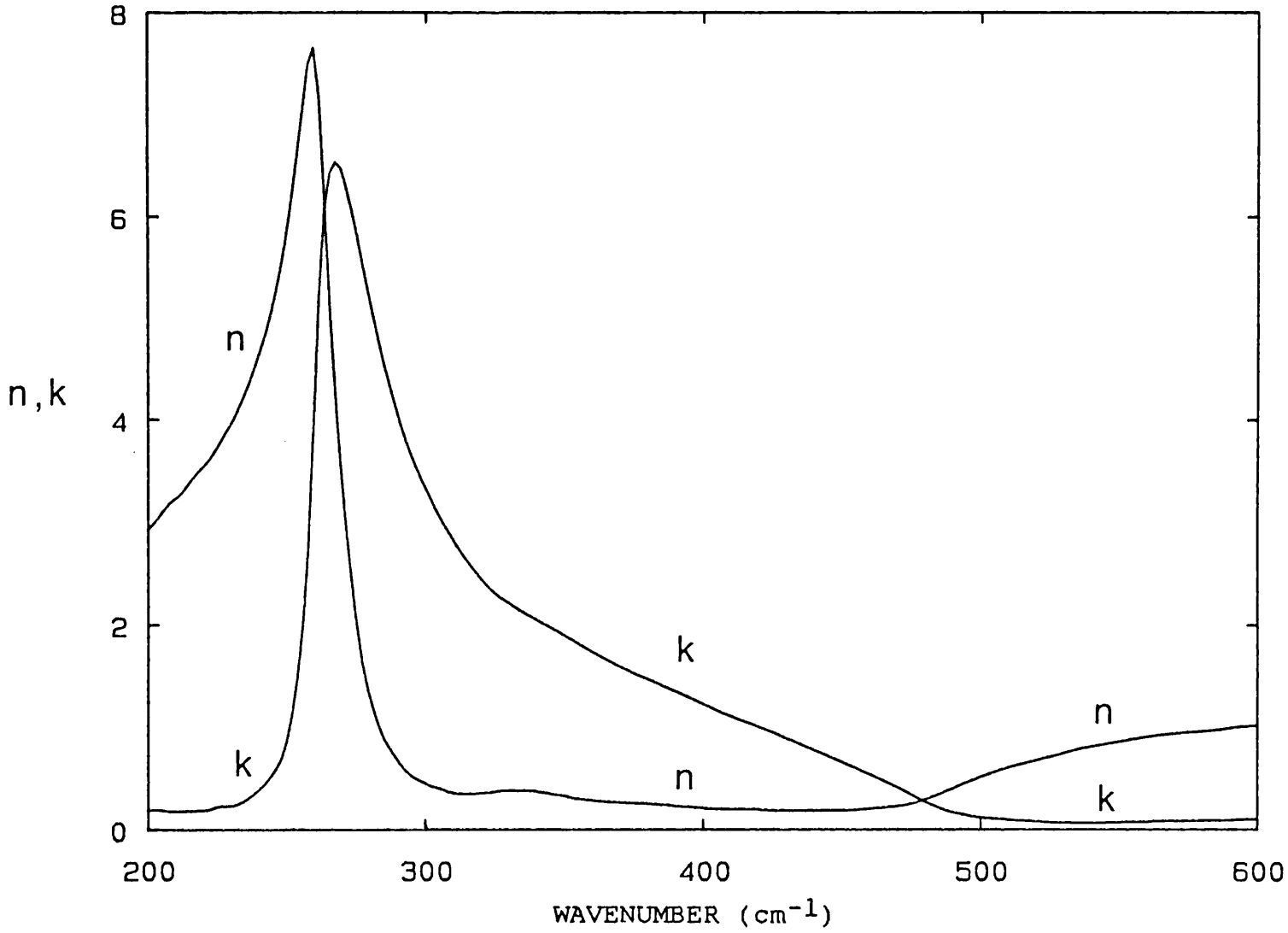

Figure 5.39 Refractive index n and absorption index k for CaF_2 at 300K

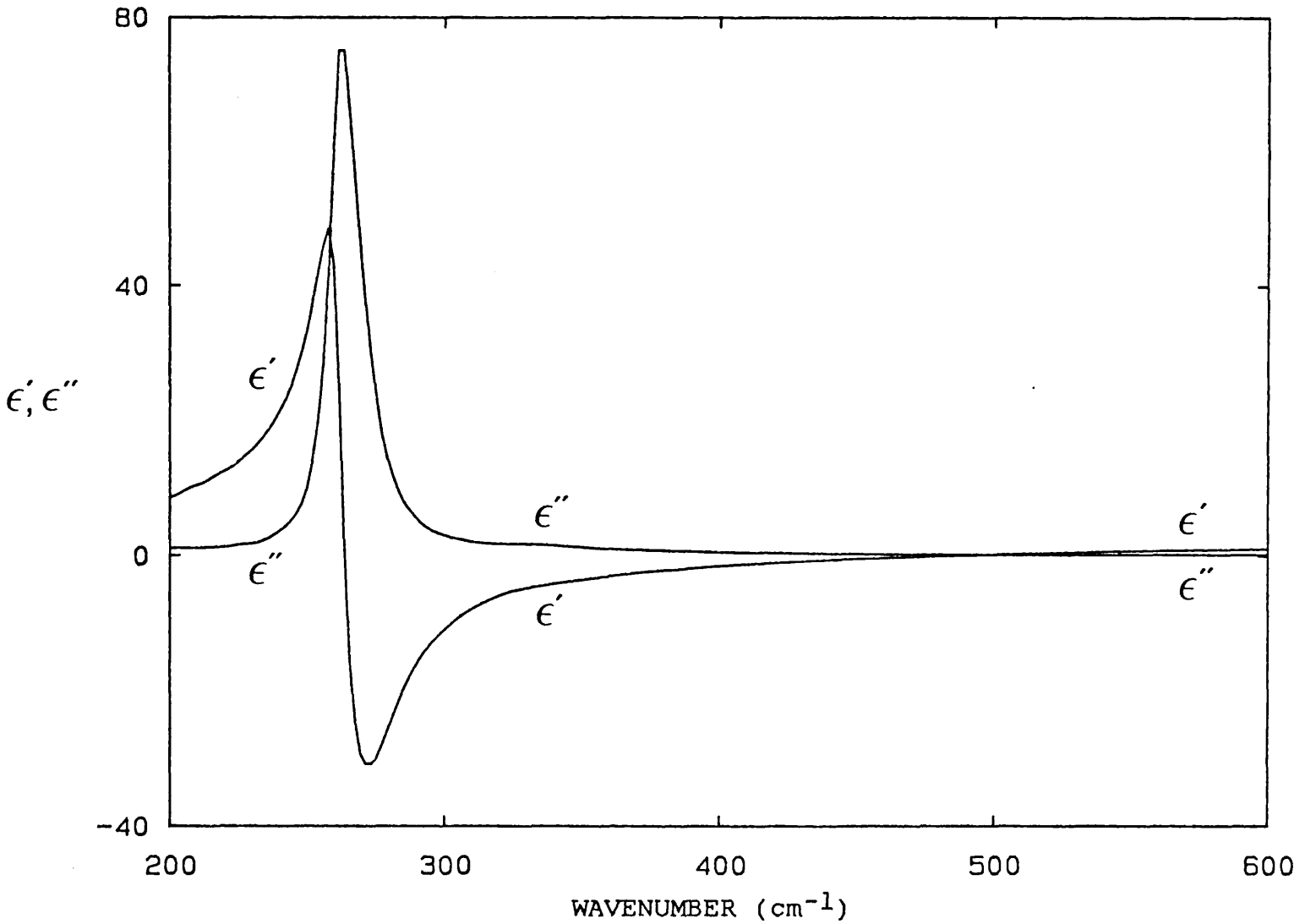

Figure 5.40 Real ϵ' and imaginary ϵ" parts of the dielectric response for CaF_2 at 300K

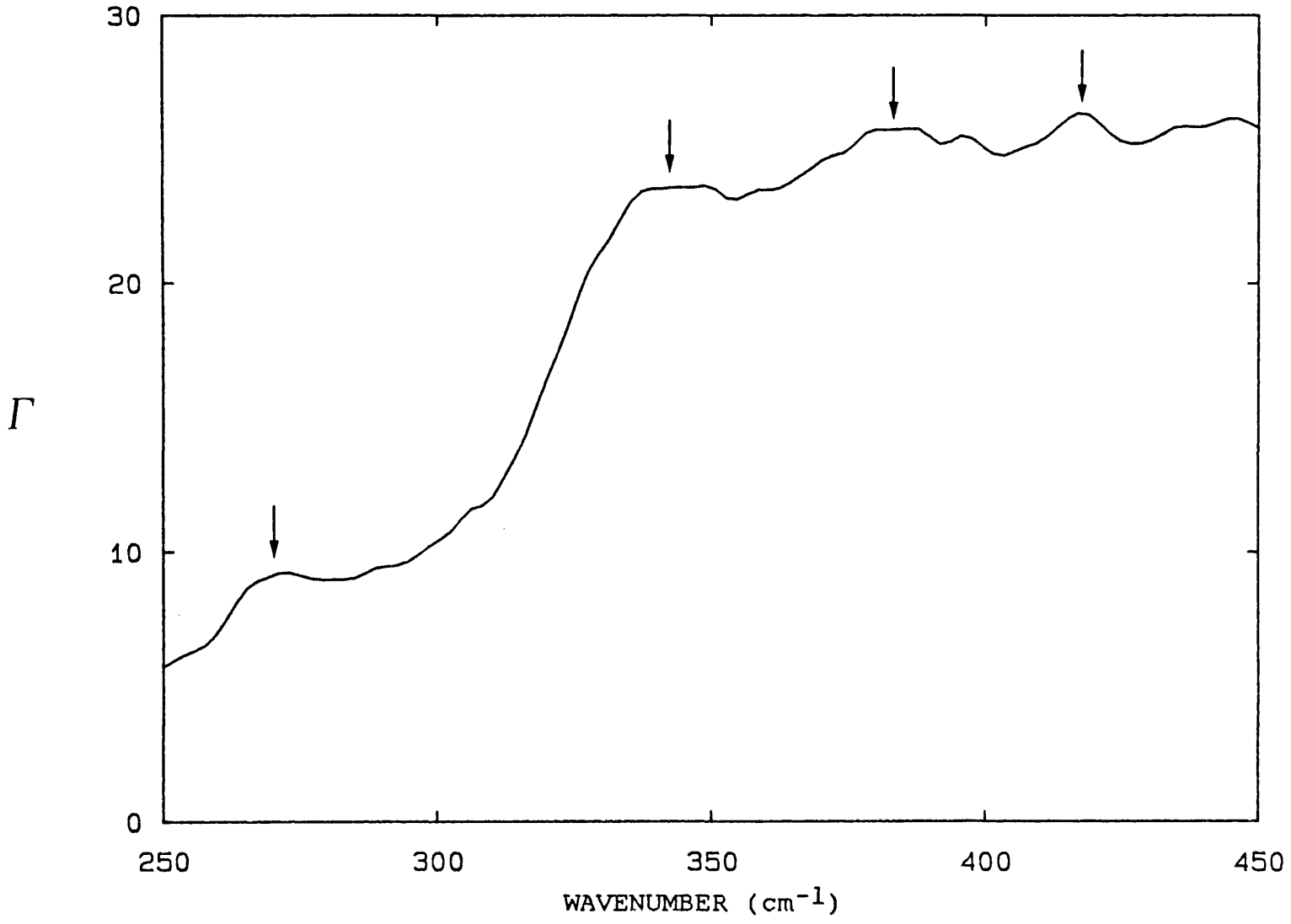

Figure 5.41 Plot of the anharmonic self energy function Γ for CaF_2 at 300K

5.11 Optical constant data of BaF_2

The amplitude r and phase ϕ of the complex reflectivity were obtained for BaF_2, as shown in figure (5.42). From these results were calculated the optical indices, n and k, shown in figure (5.43), and the dielectric functions, ϵ' and ϵ'', as shown in figure (5.44). From this the self energy function Γ was calculated, as shown in figure (5.45). Also, as seen in the CaF_2 data, a number of features were observed in the self energy function, although no previous workers have reported them. The two zone centre frequencies, TO(Γ) and LO(Γ), obtained from the dielectric response, have values of 189 cm^{-1} and 338 cm^{-1}. This compares reasonably with the work of Lowndes (1971), which gives values of 187.5 cm^{-1} and 344 cm^{-1}.

Similiar features to those of CaF_2 are seen in the self energy function, but have not been assigned.

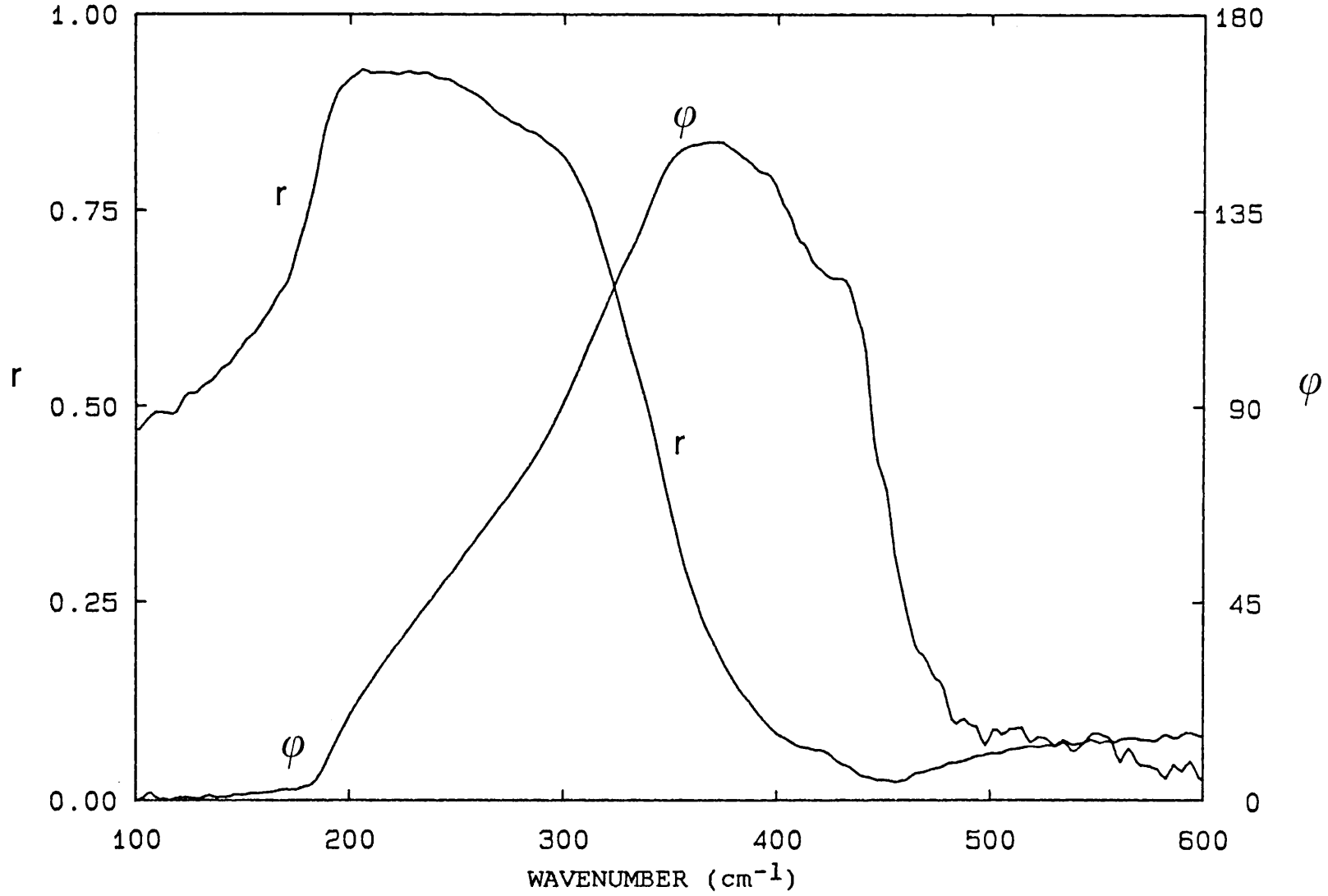

Figure 5.42 Complex reflectivity amplitude r and phase ϕ of BaF_2 at 300K

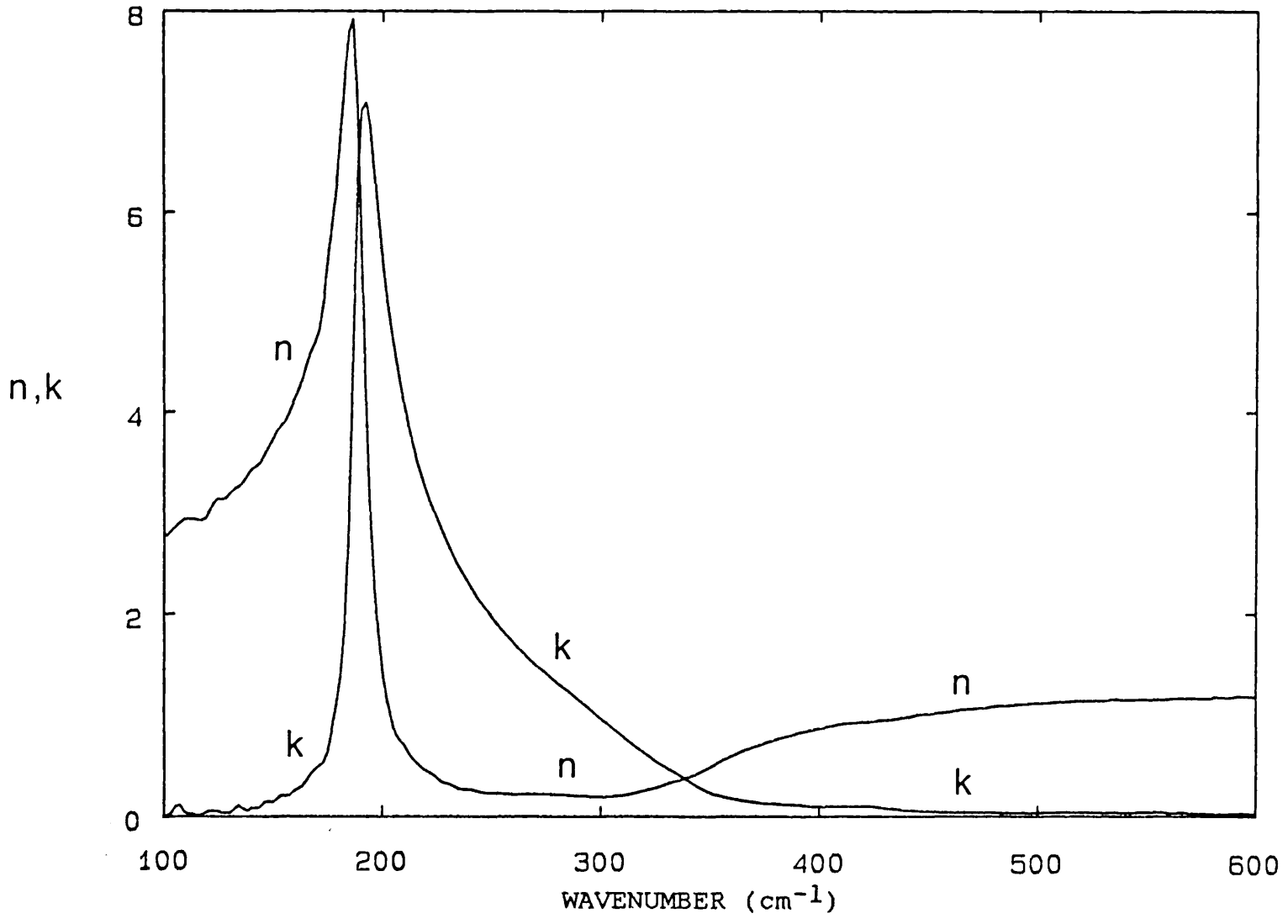

Figure 5.43 Refractive index n and absorption index k for BaF_2 at 300K

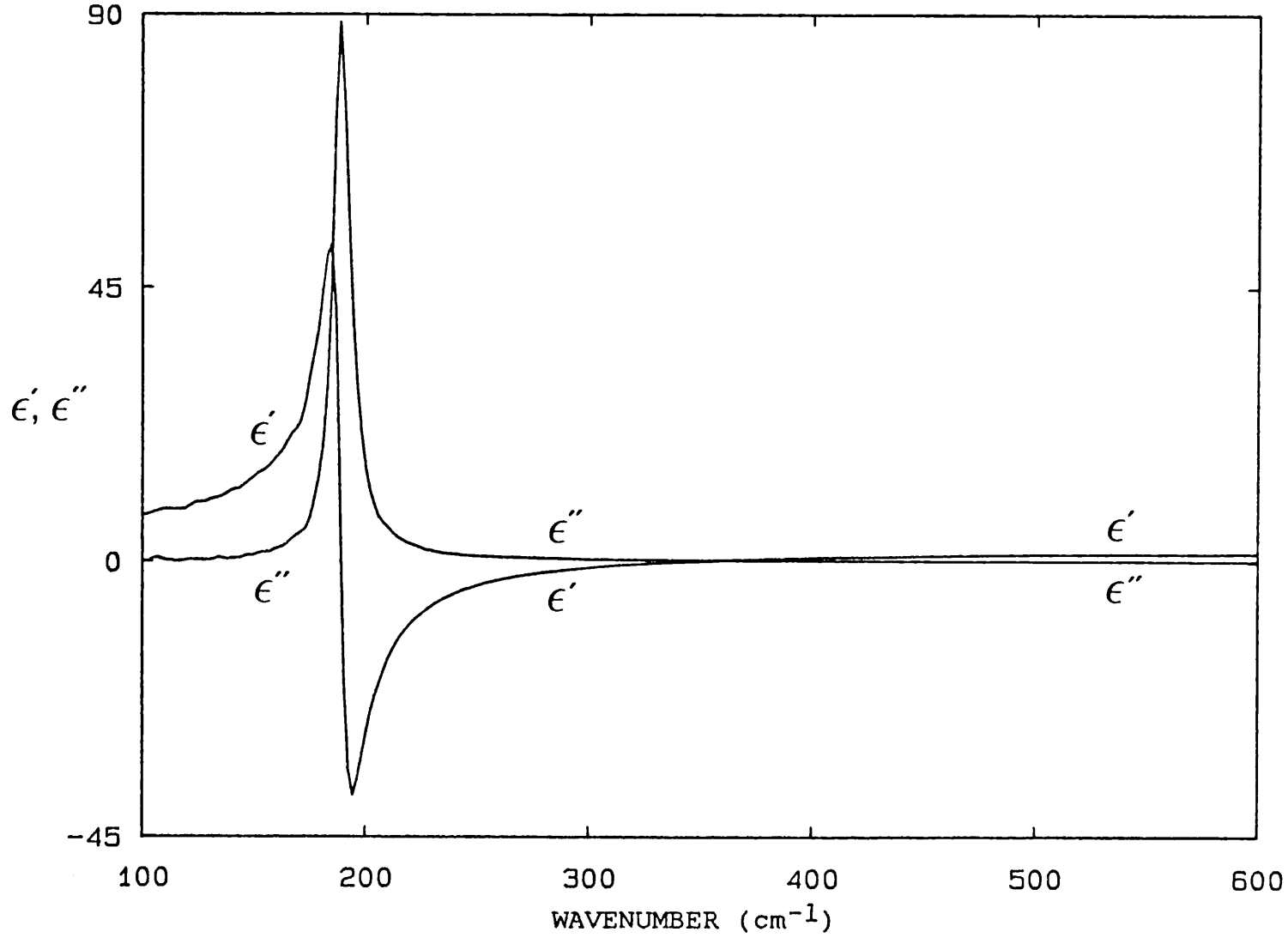

Figure 5.44 Real ϵ' and imaginary ϵ" parts of the dielectric response for BaF_2 at 300K

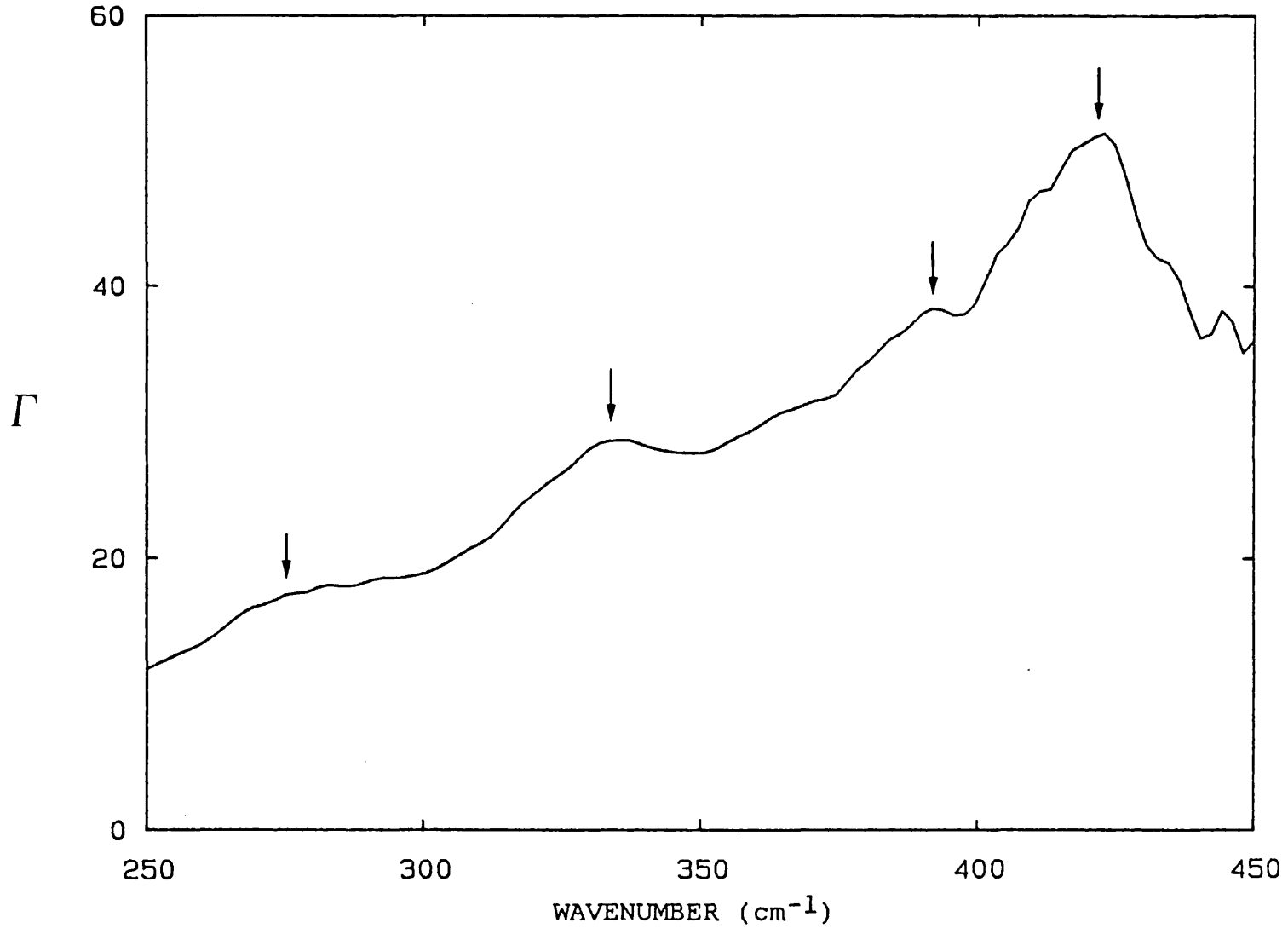

Figure 5.45 Plot of the anharmonic self energy function Γ for BaF_2 at 300K

5.12 References

Alfrey G.F and Borcherds P.H; J.Phys.C, 5, 275, (1972).

Aven M, Marple D.J.F and Segall B; J.appl.Phys.suppl to Vol.32, 10, 2261, (1961).

Birman J.L; Phys.Rev, 131, 1489, (1963)

Borcherds P.H, Alfrey G.F, Saunderson D.H and Woods A.D.B; J.Phys.C, 8, 2022, (1975).

Borcherds P.H, Kunc K, Alfreys G.F and Hall R.L; J.Phys.C.Solid State Phys, 12, 4699, (1979).

Carles R, Saint-Cricq N, Renucci J.B, Renucci M.A and Zwick A; Phys.Rev.B, 22, 4804, (1980).

Dolling G and Waugh J.T.L; "Lattice Dynamics", Editor Wallis R.F, Pergamon Press, London (1965).

Farr M.K, Traylor J.G and Sinha S.K; Phys.Rev.B, 11, 1587, (1975).

Hennion B, Moussa F, Pepy G and Kunc K; Phys Letts.A, 36, 376, (1971).

Hobden M.V and Russell J.P; Phys.Letts, 13, 39, (1964).

Hrostowski H.J and Fuller C.S; J.Phys.Chem.Solids, 4, 155, (1958).

Irwin J.C and La Combe J; Canad.J.Phys, 50, 2596, (1972).

Kiefer W, Richter W and Cardona M; Phys.Rev.B, 12, 2346, (1975).

Kleinman D.A and Spitzer W.G; Phys.Rev, 118, 110, (1960).

Koteles E.S and Datars W.R; Canad.J.Phys, 54, 1676, (1976).

Kunc K, Balkanski M and Nusimovici M.A; Phys.Stat.Solidi (b), 71, 341, (1975); Phys.Stat.Solidi (b), 72, 229, (1975); Phys.Stat.Solidi (b), 72, 249, (1975)

Lowndes R.P; J.Phys.C.Solid State, 4, 3083, (1971).

Mitra S.S; Phys.Rev, 132, 986, (1963).

Mooradian A and Wright G.B; Proc.Int.Conf. on Phys of Semicond, (1968).

Orlova N.S; Phys.Stat.Sol(b), 93, 503, (1979).

Patel C; Ph.D Thesis of (1982), University of London.

Poulet H; Ann.Phys. (Paris), 10, 908, (1955).

Price D.L, Rowe J.M and Nicklow R.M; Phys.Rev.B, 3, 1268, (1977).

Rowe J.M, Nicklow R.M, Price D.L and Zanio K; Phys.Rev, 10, 671, (1974).

Sekine T, Uchinokura K and Matsuura E; J.Phys.Chem.Solids, 38, 1091, (1977).

Sekine T, Uchinokura K and Matsuura E; Solid State Comm, 18, 1337, (1976).

Slack G.A, Ham F.S and Chernok R.M; Phys.Rev, 152, 376, (1966).

Vandevyver M and Plumelle P; J.Phys.Chem.Solids, 38, 765, (1977).

Yarnell J.L, Warren J.L, Wenzel R.G and Dean P.J; Neutron inelastic scattering, Vol.I, 301, (1968).

CHAPTER 6

Measurements on layered semiconductors

Recently some low dimensional semiconductors (LDS) have been obtained from Philips Research Ltd, grown by molecular beam epitaxy (MBE). Both multiple quantum well (MQW) samples and superlattices (SL) have been studied. Some results for the measured amplitude and phase are given in this chapter, along with theoretical results for these many layered structures.

Figure (6.1) shows the dimensions for the MQW sample studied. The structure consists of 60 periods, each period composed of 55 Å of GaAs and 170 Å of $Al_{0.35}Ga_{0.65}As$, with 0.1 μm of $Al_{0.35}Ga_{0.65}As$ cladding on each side and a top layer of 200 Å of GaAs. This is grown on a GaAs substrate of about 400 μm thickness. As can be seen, the total thickness of the multi-layered structure is only about 1.4 μm, compared to over 400 μm for the bulk medium. If information is to be obtained on this structure without being dominated by the response of the substrate, then the first few microns only have to be sampled. Since the Reststral regions for GaAs and AlGaAs are between 200 and 400 cm^{-1}, then the wavelength of study would be between 25 and 50 μm. At first sight it would appear that the layered structure cannot be probed conveniently by far infrared spectroscopy, since the wavelength of the radiation is nearly 20 times the thickness of the material to be

studied. However, the radiation is highly attenuated at the surface within the Reststrahl region. This can be shown by plotting the absorption coefficient α, which is related to the absorption index k by

$$\alpha = 4 \pi \bar{\nu} k \qquad (6.1)$$

where $\bar{\nu}$ is in wavenumbers. This has been calculated for GaAs and is shown in figure (6.2). Also by using Lambert's law, i.e

$$I = I_o e^{-\alpha d} \qquad (6.2)$$

where I_o is the incident intensity and I is the resulting intensity transmitted through a thickness d, it can be seen that the penetration depth $\propto {}^{1}/_{\alpha}$. This is also given in figure (6.2), and as can be seen, the radiation within the Reststrahl region only penetrates a couple of microns.

A MQW sample was studied by reflection DFTS, with the structure given in figure (6.1). The results of the amplitude reflectivity r and the phase ϕ are shown in figure (6.3). As can be seen there are two major reflectivity peaks, which correspond roughly to the response of the GaAs sub-lattice and the AlAs sub-lattice. The general shape of the reflectivity can be compared to work by Kim and Spitzer (1979) for $Al_xGa_{1-x}As$ bulk crystals. The phase result has a discontinuity due to branching errors in assigning the absolute phase. This has been corrected by plotting the phase over more than a 2π region, and is shown in figure (6.4). Recently, Tilley and Raj (1985) working at the University of Essex have

constructed a model for multiple layered samples using macroscopic dielectric theory. This does not take into account any folding of the Brillouin zone, so cannot be used to describe superlattice samples. Their results using the structure in figure (6.1) but with a semi-infinite substrate layer are shown in figure (6.5). By comparing figures (6.4) and (6.5), excellent agreement can be seen between experimental data and theory.

Also data has been obtained for a superlattice sample composed of 150 alternating layers of GaAs and AlAs, each 2 monolayers thick. Either side of the superlattice was a cladding layer 0.1μm thick, composed of $Al_{0.7}Ga_{0.3}As$, with the complete composite grown on a GaAs substrate. The complex amplitude and phase is shown in figure (6.6). The low frequency high reflectivity region is due to free carrier effects, since the substrate is doped. The reflectivity minimum at 210 cm^{-1} can be used to calculate the carrier concentration by using equations (4.33) and (4.34). This gives a carrier concentration of 3.5 x 10^{16} cm^{-3} using an effective mass of 0.07 m_e. The feature at 275 cm^{-1} is due to the Reststrahl region of GaAs, while the feature at 350 cm^{-1} is due to the Reststrahl region of AlAs. As can be seen, the phase has a very complex structure, which so far, has not been modelled.

6.1 References

Kim O.K and Spitzer W.G; J.Appl.Phys, 50, 6, (1979)

Raj N and Tilley D.R; Sol.State.Comm, 55, 373, (1985)

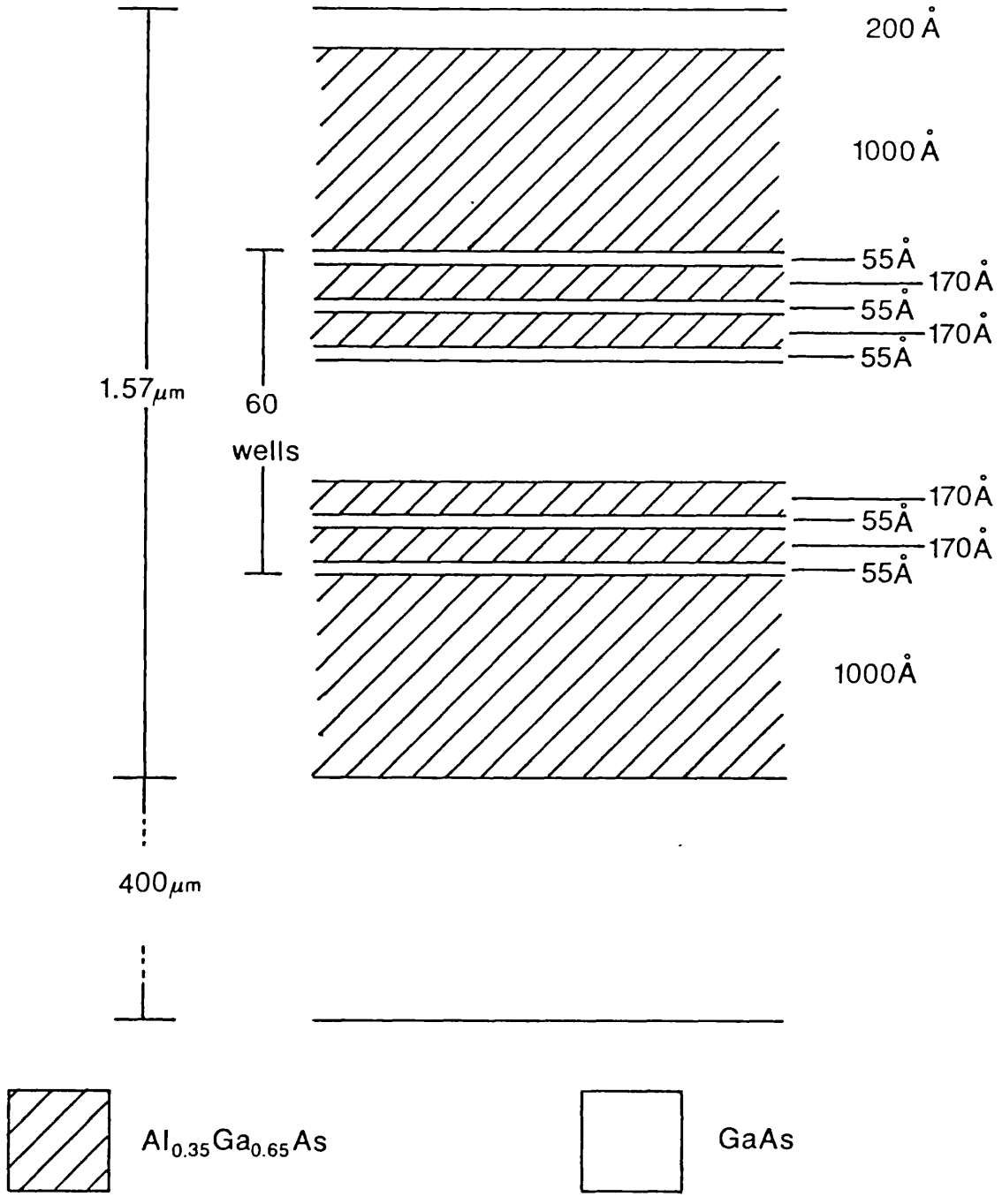

Figure 6.1 Schematic diagram of the MQW sample consisting of 60 layers of AlGaAs and GaAs, with AlGaAs cladding and a GaAs protection layer. This is deposited on a GaAs substrate.

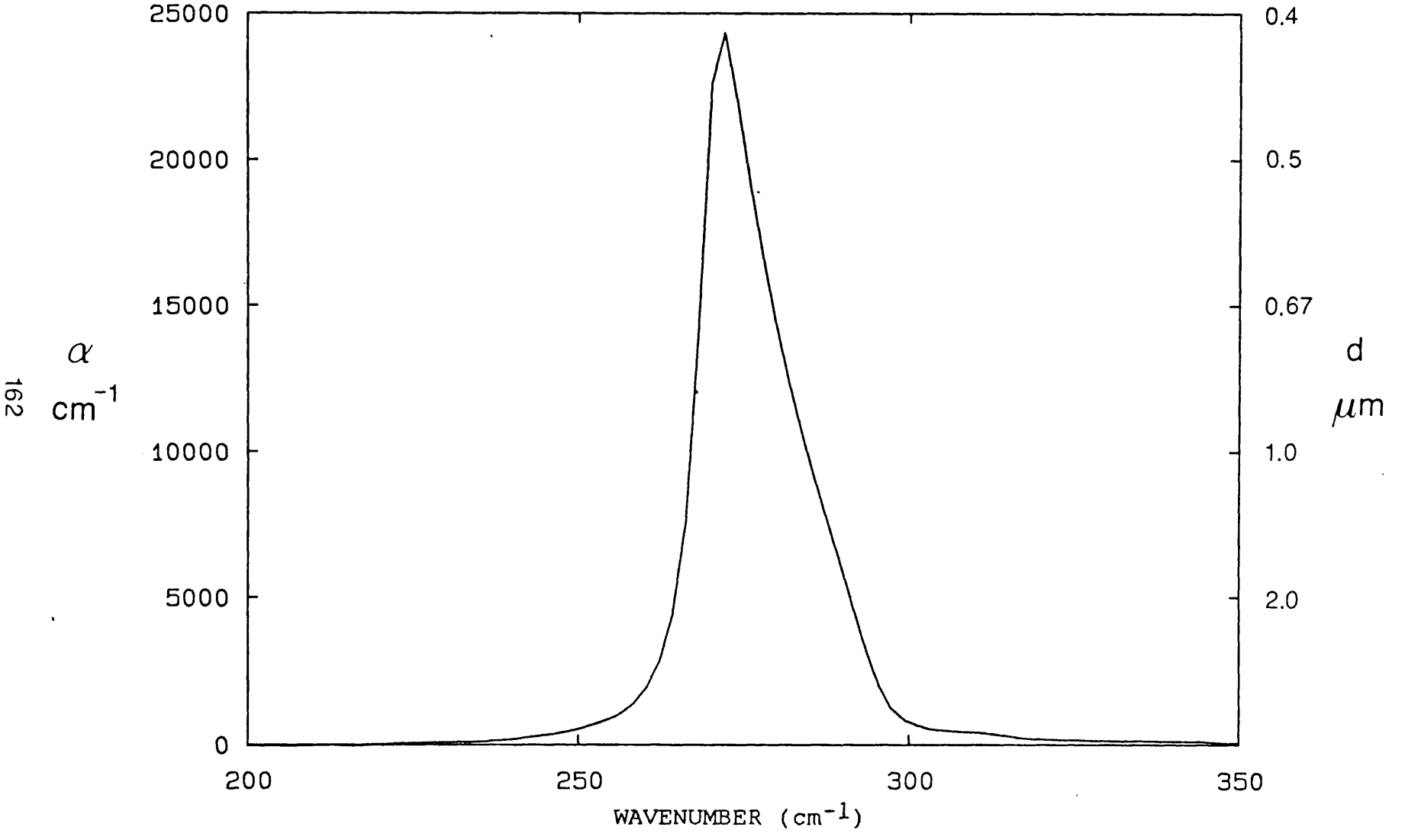

Figure 6.2 Plot of the absorption coefficient α and penetration depth d for GaAs at 300K

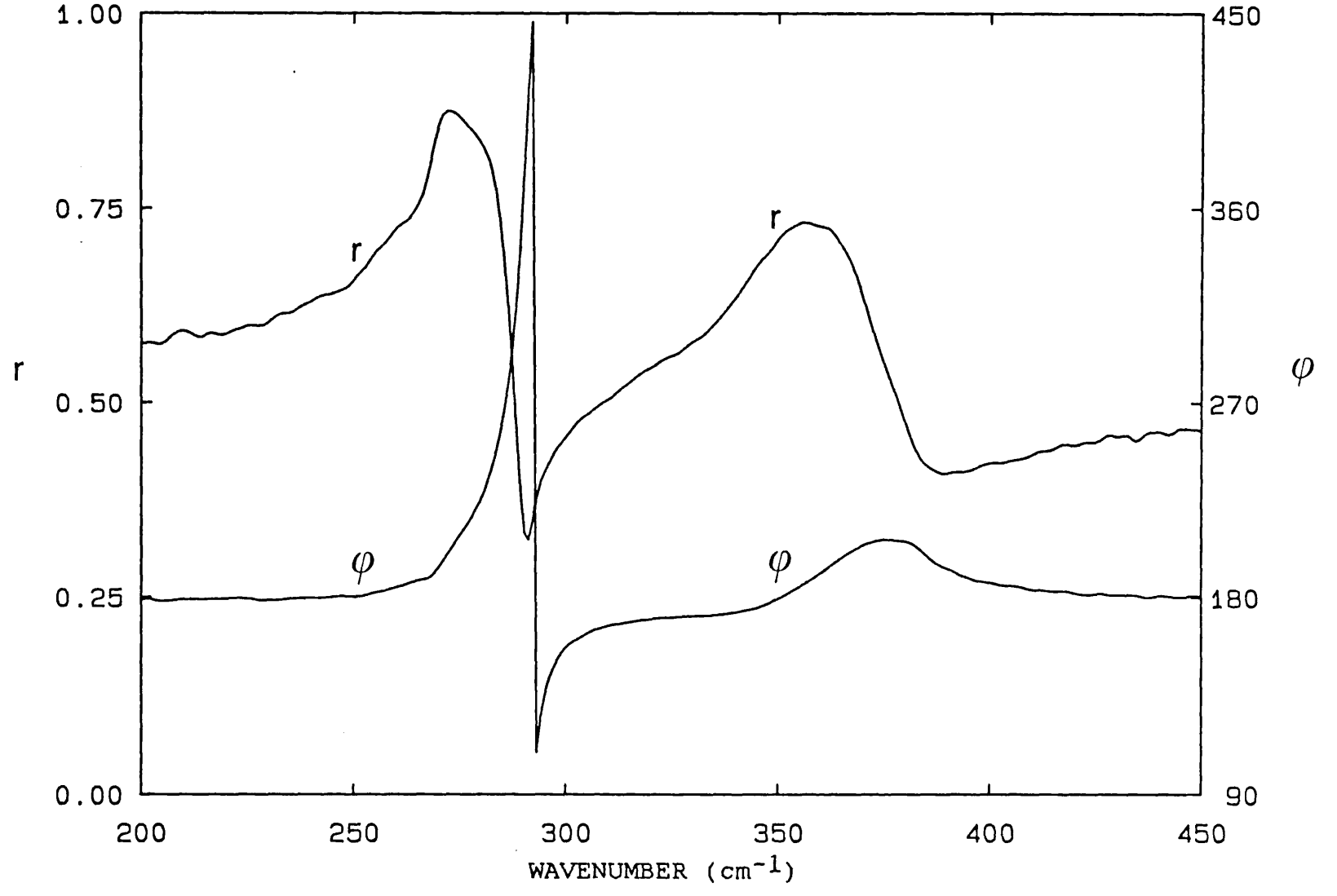

Figure 6.3 Complex reflectivity r and phase ϕ for MQW sample (figure 6.1) at 300K

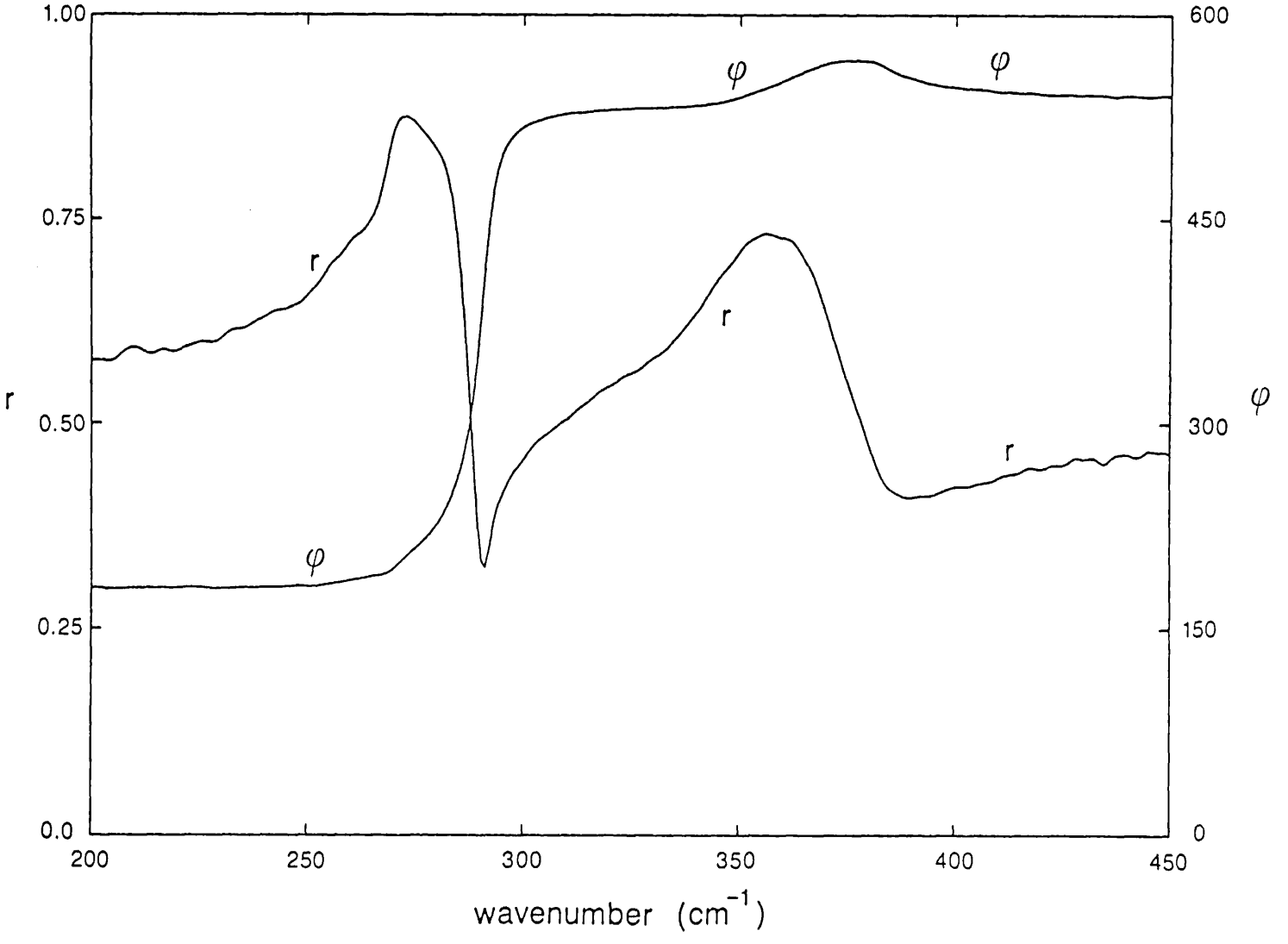

Figure 6.4 Complex reflectivity r and corrected phase ϕ for MQW sample (figure 6.1) at 300K

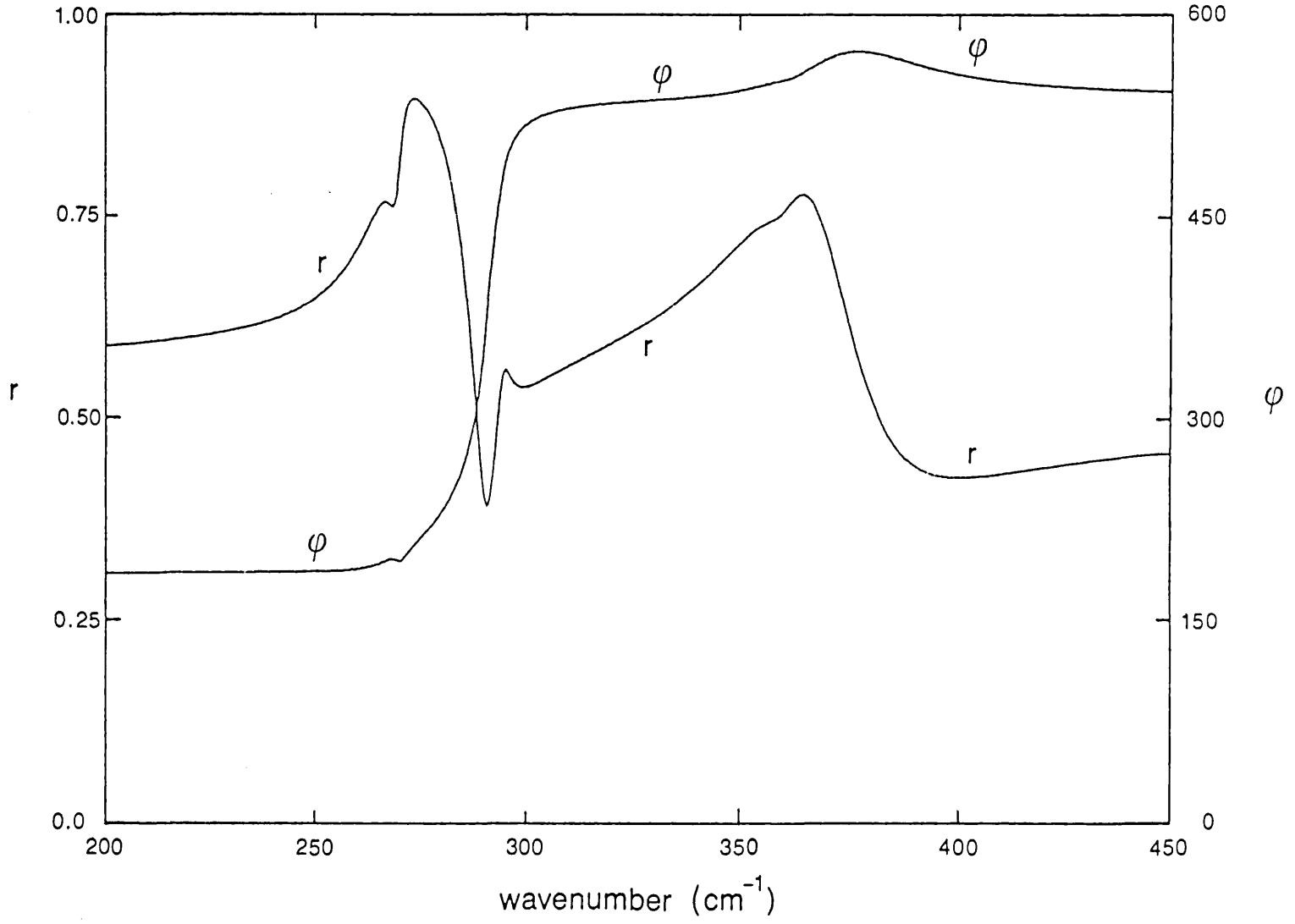

Figure 6.5 Theoretically calculated reflectivity r and ϕ for MQW sample (figure 6.1)

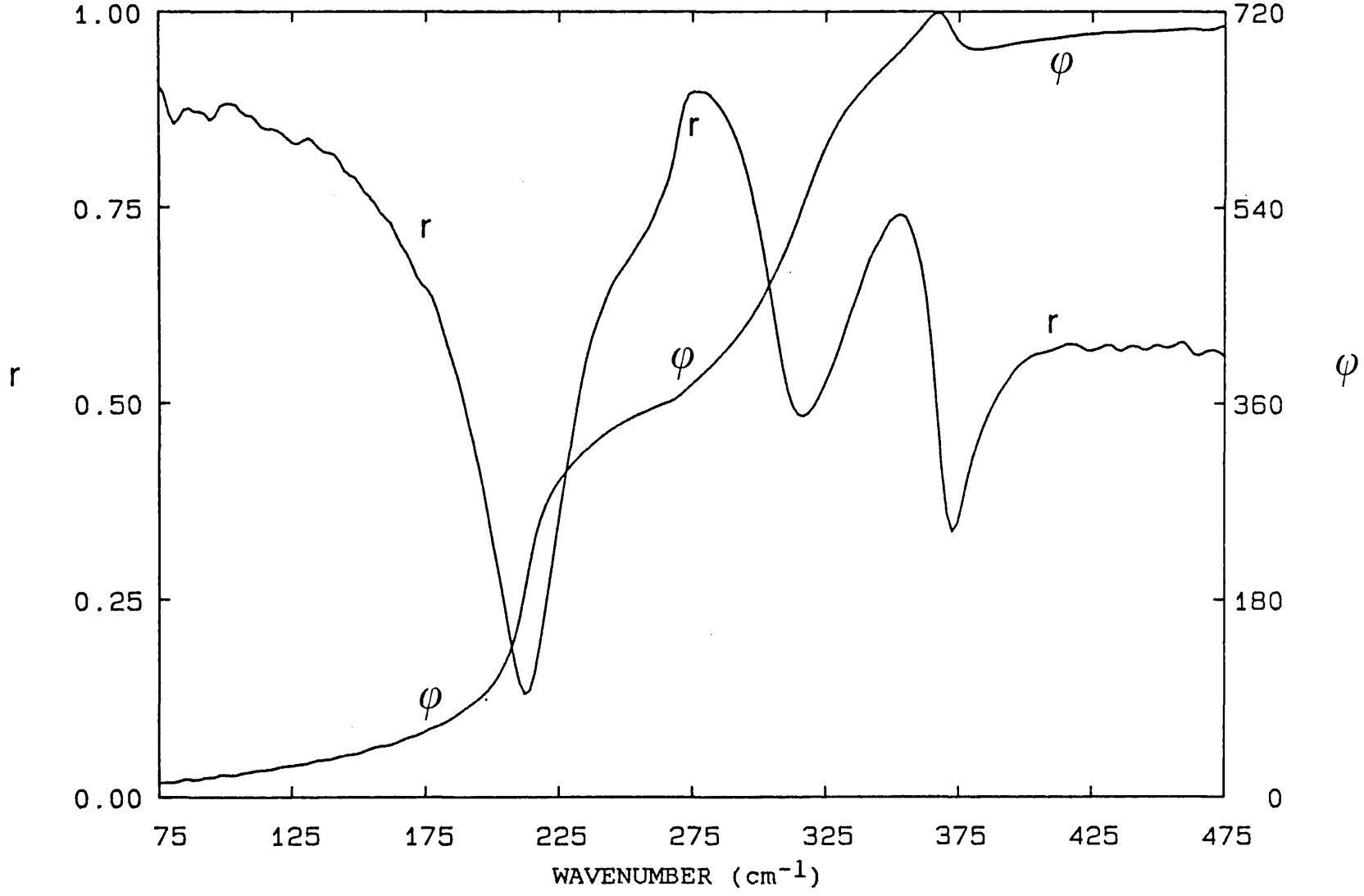

Figure 6.6 Complex reflectivity r and phase ϕ for superlattice sample at 300K

CHAPTER 7

CONCLUSIONS

An NPL/Grubb Parsons cube interferometer has been greatly improved by replacing the step drive moving mirror mechanism with a linear bearing and a hydraulic piston with a speed stability of about 1%. The position of the moving mirror is determined by laser fringe detection with an accuracy of about ± 6nm. The hydraulic piston direction and switching operations are controlled by the computer via an IEEE interface. The computer can also determine the method of laser fringe sampling, either to sample at every laser fringe or to count fringes to give the required sampling interval. By the use of the computer/interface, the ease of operation of the interferometer has been greatly improved, as well as allowing co-adding of interferograms to improve the signal to noise ratio.

A new output optics chamber has been constructed, which allows the focal length to be changed easily so that different detectors can be conveniently coupled to the instrument. Also the positioning controls of the output beam and the laser detector are outside the vacuum wall to facilitate alignment. The vacuum pumping system has been rationalised to decrease pumping down times and vibrational effects, giving a vacuum of about 10^{-5} Torr within the interferometer.

The optical response of 10 materials have been measured

in the far infrared by the use of dispersive Fourier transform spectroscopy. For most of these materials, these are the first measurements of the amplitude reflectivity r and phase ϕ around the Reststrahl region. From r and ϕ, the refractive index n and the absorption index k have been determined from the Fresnel relations at normal incidence, as well as the real part ϵ' and imaginary part ϵ'' of the dielectric response.

The frequency dependence of the anharmonic self energy function Γ of the zone centre transverse optic phonon mode has been calculated from the dielectric functions in each case, and many small features are observed for the first time. These features are interpreted as phonon combination bands from the decay of the zone centre TO mode.

Values for phonon frequencies are available from inelastic neutron scattering data, Raman and infrared measurements and from mathematical models of the lattice dynamics. Neutron scattering is the only direct method for determining phonon dispersion curves, but due to the experimental procedure the results obtained have large uncertainties. Raman scatttering and infrared absorption measurements only give the zone centre optical modes, so that the best description is probably given by an appropriate lattice model fitted to suitable experimental data.

In the present work phonon frequencies from an 11 parameter rigid ion model developed by Patel have been used to calculate the frequencies of expected features in Γ, and in most cases good agreement has been obtained with the

observed features. These results not only give a direct measurement of the optical characteristics within regions of high reflectivity, but support the validity of the rigid ion model.

Reflectivity measurements have also been performed on some low dimensional semiconductors, which are the first ever reported in the far infrared. These have been compared to a theoretical model of the multiple layered sample by Raj and Tilley, with very good agreement.

APPENDIX A

The Jacquinot and Fellgett advantages

As mentioned in the introduction, interferometers have a number of advantages over conventional grating or prism spectrometers. Two of the major advantages are discussed below.

Jacquinot advantage

The etendue is the constant which determines the amount of light that can be transmitted by a particular optical system. It is defined as

$$E = A\Omega \tag{A.1}$$

where A is the area of the collimator and Ω is the solid angle subtended by the source. Jacquinot (1960) showed that for an interferometer $A\Omega$ is a constant from the source to the detector. He also showed that the etendue of a Michelson interferometer is much higher than that of a grating spectrometer. Results from Bell (1972) give the etendue for a Michelson interferometer as

$$E_m = A_m \Omega_m = 2\pi \frac{A_m}{R_m} \tag{A.2}$$

where A_m is the area of the collimator and R_m is the resolving power of the interferometer.

In the case of the grating spectrometer, the power through the instrument is limited by the area of the entrance slit. Bell (1972) shows that the etendue of the grating spectrometer is approximated to

$$E_g \propto \frac{L}{f} * \frac{A_g}{R_g} \qquad (A.3)$$

where L is the length of the slit, f is the focal length of the collimator, A_g is the area of the collimator and R_g is the resolving power of the spectrometer.

If we assume that $A_g \propto A_m$ and that the focal length of the collimators and resolving powers of the interferometer and grating spectrometers are the same (i.e $R_m \propto R_g$) then the ratio of the two etendue is

$$\frac{E_m}{E_g} \propto 2\pi \frac{f}{L} \qquad (A.4)$$

The best value of f/L for a grating spectrometer is never less than 30, so the etendue of a Michelson is nearly 200 times better. As long as the instrument is designed so that the whole solid angle intercepts the detector, the Jacquinot advantage will be realised.

Fellgett advantage

The Fellgett or multiplex advantage can be expressed in the following way. If we observe a spectrum containing n

spectral elements, each element with a width of the spectral resolution, then with a grating or prism spectrometer each element is observed for a time T/n as the exit slit scans. The signal to noise ratio of the observed spectrum is proportional to the square root of the observation time, i.e

$$(S/N)_g \propto \sqrt{(T/n)} \tag{A.5}$$

In the case of a Michelson interferometer, each element is observed all the time during a scan. Thus, the signal to noise ratio will be proportional to the square root of the observation time, i.e

$$(S/N)_i \propto \sqrt{T} \tag{A.6}$$

Therefore, the ratio between the interferometer and the grating signal to noise ratio will be

$$\frac{(S/N)_i}{(S/N)_g} = \sqrt{n} \tag{A.7}$$

Since n is typically of the order of 100 or more, the signal to noise ratio of an interferometer will be much higher than that of a grating device. This is the Fellgett or multiplex advantage.

APPENDIX 2

IEEE Commands

Below is a description of the various IEEE 488 commands used to collect and control data.

IFC488 No parameters.

This command pulses the IFC line for approximately 20 ms to clear the bus and return all devices to their initial state.

COM488 code = integer variable.

This sets the ATN line true and sends the variable. There are more than 20 command codes which can be called, although only the two below have ever been used.

COMMAND	FUNCTION	CODE VALUE
GET	Group Execute Trigger Initiates a simultaneous pre-defined action by responding devices	8
DCL	Device Clear Returns all devices that can respond to a pre-determined state.	20

NUI488 tout,st,fl,nb,dummy[array],sa,pa = integer;

Transfer data from the TALKER on the IEEE-488 bus

and store in an integer array or variable

NUO488 tout,st,fl,nb,dummy[array],sa,pa = integer;

Send data from integer array or variable to the LISTENER on the IEEE-488 bus. The various parameters which have been used are described below

pa Integer containing the primary address of the Microlink, which is usually 7.

sa Integer containing the secondary address of a module within the Microlink. For the ADC unit AN-1D the value is 1.

dummy The first element of an integer array. This is where the data is stored.

nb Integer containing the number of bytes to be transferred as data.

fl Integer whose bit pattern determines how the data will be transferred. Values used are

fl = 16 Ignore timeout signals

fl = 129 Send GET command prior to input

st Integer whose bit pattern can be examined to check for correct data transfer. This function is not normally required, so is set to 0.

tout Integer used as a software timer, which stops the computer from "hanging-up" if the wrong address is sent or the device is disconnected. A value of about 500 is equivalent to 1 second.

The program used to collect the interferograms and control

the hydraulic system is given below. Electronic sampling is obtained by using the laser fringe counting circuit set to the required step interval, and the number of fringes per point NOOF set to 1. Otherwise, every laser fringe will be sampled with the control of the step size dependent on the value of NOOF.

```
PROGRAM mscan(input,output);
TYPE intarray = array [1..16000] of integer;
VAR    bal     : intarray;
       ba      : array [1..4000] of integer;
       breal   : array [1..4000] of real;
       clock   : array [1..2] of integer;
       y       : string(1);
       fnamel  : string(15);
       f       :  file of integer;
       a,i,j,k,n,t,tout,st,nb,fl,fll,sa,pa,ip : integer;
       code,stara,enda,nsave,nscan,noof,nend : integer;
       max,min,imin : integer;

PROCEDURE IFC488; extern;
PROCEDURE COM488(var p : integer); extern;
PROCEDURE NUO488(var r1,r2,r3,r4,r5,r6,r7:integer); extern;
PROCEDURE NUI488(var p1,p2,p3,p4,p5,p6,p7:integer); extern;

PROCEDURE store;
BEGIN
    close(f);
    write('Type in the file name : ');readln(fnamel);
    assign(f,fnamel);
    rewrite(f);
    for i:=1 to nsave do
    ba[i]:=trunc(0.5+(breal[i]/nscan));
    for i:=1 to nsave do write(f,ba[i]);
    close(f);
```

```
END;
(* MAIN PROGRAM *)
BEGIN
    IFC488;     (*   clear bus lines   *)
    writeln('This is the Sirius data recording program ');
    writeln('Software or electronic sampling ');
    writeln('NB : sets mid point on Minimum value ');
       (*   Peak or minimum of zero path used as centre  *)
    write('Set ZP to Minimum (1) Maximum (2) :');readln(t);
        (*   total number of points to be read NEND    *)
    write('Input No of data points          :');readln(nend);
       (*   number of fringes skipped per point NOOF   *)
    write('Input No of fringes per point :');readln(noof);
       (*   number of points to average and saved NSAVE  *)
    write('Input No of points to save   :');readln(nsave);
       (*   number of scans to co-average NSCAN   *)
    write('Input No of scans            : ');readln(nscan);
       (*   set up HSC   *)
    nb:=2; sa:=0; clock[1]:=8; clock[2]:=0;
    tout:=512; st:=0; pa:=7;
    NUO488(tout,st,fl,nb,clock[1],sa,pa);
       (*   set up ADC   *)
    sa:=1; fl:=129; fll:=16; nb:=1; ip:=2;
    NUO488(tout,st,fll,nb,ip,sa,pa);
       (*   start drive up   *)
    code:=8; COM488(code);
       (*   begin multiple scans k   *)
    for k:=1 to nscan do
    BEGIN
       (*   take data, put in bal[]   *)
      NUI488(tout,st,fl,nend,bal[1],sa,pa);
       (*   stop drive, change direction   *)
      code:=8; COM488(code);
      max:=bal[1]; min:=bal[1];
       (*   Minimum as zero path, find ADC range  *)
      if t=1 then
      BEGIN
      for j:=1 to nend do
        BEGIN
```

```
        if max<bal[j] then max:=bal[j];
        if min>bal[j] then BEGIN min:=bal[j];imin:=j;END;
      END;
    END;
    ELSE          (*   Maximum as zero path   *)
    BEGIN
    for j:=1 to nend do
      BEGIN
        if max<bal[j] then BEGIN max:=bal[j];imin:=j;END;
        if min>bal[j] then min:=bal[j];
      END;
    END;
    stara:=imin - ((nsave div 2) * noof);
    enda:= imin + ((nsave div 2) * noof);
     (*   co-average data, store in breal array    *)
    for j:=1 to nsave do
    BEGIN
        if nscan = 1 then breal[j]:=0;
       breal[j]:=bal[stara-noof+j*noof] + breal[j];
    END;
    writeln('Reverse scan ',k,' completed ');
    writeln('ADC range is ',max-min,' ZP at ',imin);
     (*   start drive in forward direction    *)
    code:=8; COM488(code);
    NUI488(tout,st,f1,nend,bal[1],sa,pa);
     (*   stop drive, change direction    *)
    code:=8; COM488(code);
    writeln('Forward scan ',k,' completed');
     (*   start drive, reverse direction    *)
    code:=8; COM488(code);
  END;
     (*   store data ?    *)
  write('Do you want to store the data : ');readln(y);
  if (y='y') or (y='Y') then store;
END.
```

Publications based on the work described in this thesis

A.K.Wan Abdullah, K.A.Maslin and T.J.Parker.
Observation of two-phonon difference bands in the FIR transmission spectrum of Si.
Infrared Physics, 24, 185-188 (1984)

K.A.Maslin, G.A.Gledhill and T.J.Parker.
Comparison of the techniques of Dispersive and Power Fourier Transform Spectroscopy for the investigating the FIR properties of imperfect crystals.
Infrared Physics, 25, 439-441 (1985)

C.Patel, K.A.Maslin and T.J.Parker.
Study of lattice anharmonicity in ZnSe by Dispersive Fourier Transform Spectroscopy.
to be published in the Proceedings of the Second International Conference on Phonon Physics, August 26-30, 1985, Budapest.

T.J.Parker, K.A.Maslin, D.R.Tilley, N.Raj and P.J.Dobson.
The far infrared lattice response of GaAs-AlGaAs superlattices.
To be submitted to Physical Review Letters.